



---

**Forschungszentrum Karlsruhe**  
Technik und Umwelt

---

**Wissenschaftliche Berichte**  
FZKA 7431

# **Dielectrophoresis of Single-Walled Carbon Nanotubes**

**S. Blatt**

Institut für Nanotechnologie

**August 2008**

---

**Forschungszentrum Karlsruhe**  
in der Helmholtz-Gemeinschaft  
Wissenschaftliche Berichte  
FZKA 7431

**Dielectrophoresis  
of Single-Walled Carbon Nanotubes**

Sabine Blatt

Institut für Nanotechnologie

Von der Fakultät für Physik der  
Universität Karlsruhe (TH)  
genehmigte Dissertation

Forschungszentrum Karlsruhe GmbH, Karlsruhe  
2008

Für diesen Bericht behalten wir uns alle Rechte vor

Forschungszentrum Karlsruhe GmbH  
Postfach 3640, 76021 Karlsruhe

Mitglied der Hermann von Helmholtz-Gemeinschaft  
Deutscher Forschungszentren (HGF)

ISSN 0947-8620

urn:nbn:de:0005-074310

# Dielectrophoresis of Single-Walled Carbon Nanotubes

---

## Dielektrophorese von einwandigen Kohlenstoff-Nanoröhren

Zur Erlangung des akademischen Grades eines  
DOKTORS DER NATURWISSENSCHAFTEN

von der Fakultät für Physik der  
Universität (TH) Karlsruhe

genehmigte

DISSERTATION

von

Dipl.-Phys. Sabine Blatt  
aus Koblenz

Tag der mündlichen Prüfung:  
Referent:  
Korreferent:

11.07.2008  
Prof. Dr. Hilbert von Löhneysen  
Prof. Dr. Manfred M. Kappes



## Abstract

This work was focused on the behavior of single-walled carbon nanotubes under the influence of dielectrophoretic forces. In particular, it aimed at an understanding of the basic processes in dielectrophoretic separation and assembly experiments. By dielectrophoretic deposition onto interdigitated electrode arrays continuous films of carbon nanotubes were produced, in which metallic and semiconducting nanotubes possess a significantly different degree of alignment with respect to the electric field. These findings were explained with an advanced theoretical model for nanotube dielectrophoresis, which takes into account the structural and dielectric anisotropy of single-walled carbon nanotubes. An experiment was designed to measure the degree of alignment of dispersed single-walled carbon nanotubes under variation of the applied electric field, from which—according to the theoretical predictions—the dielectric properties of the nanotubes can be derived. First results revealed a weak dependence of the alignment on the electric field. The possibility of separating metallic and semiconducting single-walled carbon nanotubes by electrodeless dielectrophoresis through nanopores was studied under various experimental conditions. The results suggest that after an optimization of the process parameters, electrodeless dielectrophoresis might be suited for an upscaling of the separation of single-walled carbon nanotubes. Additionally, finite element simulations were carried out to visualize the electric potential and dielectrophoretic force fields in various electrode setups. The results allowed for an interpretation of experimental observations regarding the influence of the sample substrate on the dielectrophoretic deposition of single-walled carbon nanotubes, the self-limiting single-nanotube assembly and the characterization of carbon nanotubes by voltage-contrast scanning tunneling microscopy.

## Kurzzusammenfassung

### Dielektrophorese von einwandigen Kohlenstoff-Nanoröhren

Die vorliegende Arbeit befasst sich mit dem Verhalten einwandiger Kohlenstoff-Nanoröhren unter dem Einfluss dielektrophoretischer Kraftfelder. Ziel der Arbeit ist es, ein grundlegendes Verständnis der fundamentalen Prozesse bei der dielektrophoretischen Trennung und Platzierung von Kohlenstoff-Nanoröhren zu erhalten. Durch dielektrophoretische Deposition auf interdigitalen Elektroden wurden kompakte Filme aus Kohlenstoff-Nanoröhren hergestellt, in denen die metallischen und halbleitenden Nanoröhren eine signifikant unterschiedliche Ausrichtung in Bezug auf das elektrische Feld aufweisen. Dieser Effekt lässt sich

mit einem erweiterten theoretischen Modell für die Dielektrophorese von Kohlenstoff-Nanoröhren erklären, das die geometrische und dielektrische Anisotropie der Nanoröhren explizit berücksichtigt. Entsprechend der theoretischen Vorhersagen erlaubt eine Untersuchung der Ausrichtung suspendierter Nanoröhren unter Variation der Feldparameter die Bestimmung ihrer dielektrischen Eigenschaften. Hierzu wurde ein Experiment konzipiert, dessen erste Ergebnisse eine schwache Abhängigkeit der Ausrichtung vom elektrischen Feld zeigen. Um die Machbarkeit einer Trennung von metallischen und halbleitenden Kohlenstoff-Nanoröhren durch elektrodenlose Dielektrophorese zu untersuchen, wurde der Transport von Nanoröhren durch Nanoporen unter unterschiedlichen experimentellen Bedingungen studiert. Die Ergebnisse weisen darauf hin, dass die elektrodenlose Dielektrophorese nach einer Optimierung der Prozessparameter möglicherweise ein Hochskalieren der dielektrophoretischen Separation erlaubt. Zusätzlich zu der experimentellen Arbeit wurden Finite Elemente Simulationen durchgeführt, um die Verteilung des elektrischen Potentials und der dielektrophoretischen Kraftfelder in unterschiedlichen Elektrodenanordnungen zu bestimmen. Die Ergebnisse dieser Rechnungen erlauben die Interpretation experimenteller Befunde in Bezug auf den Einfluss des Substrats auf die dielektrophoretische Deposition von Kohlenstoff-Nanoröhren, die Selbstbegrenzung bei der dielektrophoretischen Platzierung und die Charakterisierung der elektronischen Eigenschaften von Nanoröhren durch Spannungs-Kontrast Elektronenmikroskopie.

# Deutsche Zusammenfassung

Seit dem Beginn der 80er Jahre haben die Forschungsaktivitäten im Bereich der Nanotechnologie einen deutlichen Zuwachs erlebt. Unter den neuartigen Materialien, deren Eigenschaften untersucht werden, werden einwandige Kohlenstoff-Nanoröhren besonders intensiv erforscht. Einwandige Kohlenstoff-Nanoröhren sind zylindrische Objekte aus Kohlenstoff, die man sich anschaulich als eine zu einem nahtlosen Zylinder aufgerollte Graphen-Ebene vorstellen kann. Eine Kohlenstoff-Nanoröhre stellt ein einzigartiges, quasi-eindimensionales molekulares System dar; unter anderem zeichnet sie sich dadurch aus, dass die Richtung, in der die Graphen-Ebene aufgerollt wird, die elektronischen Eigenschaften der Nanoröhre bestimmt und sowohl metallische als auch halbleitende einwandige Kohlenstoff-Nanoröhren existieren.

Für die Grundlagenforschung haben Kohlenstoff-Nanoröhren eine große Bedeutung, da sie die experimentelle Verifikation theoretischer Vorhersagen ermöglichen, z. B. in Bezug auf thermische und elektronische Transportprozesse in eindimensionalen Leitern. Darüber hinaus gibt es vielversprechende Ansätze, Nanoröhren als Bauteile für zukünftige Anwendungen zu verwenden. Bevor jedoch Kohlenstoff-Nanoröhren effizient in elektronische Schaltkreise integriert werden können, muss zunächst eine Reihe von Problemen gelöst werden. Eines dieser Hindernisse ist das Fehlen eines selektiven Herstellungsprozesses – keiner der derzeitigen Wachstumsprozesse erlaubt die kontrollierte Herstellung von Kohlenstoff-Nanoröhren mit definierten elektronischen Eigenschaften. Während somit immer eine Mischung aus metallischen und halbleitenden Nanoröhren produziert wird, setzen einige Anwendungen die Verwendung von ausschließlich einem elektronischen Typus voraus; deshalb ist ein effizienter Trennprozess notwendig. Ein weiteres Hemmnis ist die präzise und reproduzierbare Platzierung der Nanoröhren innerhalb eines Schaltkreises.

In beiden Bereichen konnten durch die Anwendung von Wechselfeld-Dielektrophorese (DEP) in den vergangenen Jahren deutliche Fortschritte erzielt werden. Dielektrophorese beschreibt die Bewegung eines in Flüssigkeit dispergierten polarisierbaren Objekts unter dem Einfluss eines inhomogenen externen elektrischen Felds. Die dielektrophoretische Kraft ist unabhängig von der Ladung des Teilchens und wird stattdessen durch seine Größe und Form und das Verhältnis der dielektrischen Eigenschaften des Teilchens und der umgebenden

Flüssigkeit bestimmt. Man unterscheidet zwischen positiver und negativer DEP, je nachdem ob das Objekt aufgrund einer größeren Polarisierbarkeit im Vergleich zur Flüssigkeit eine attraktive Kraft in Richtung der Feldinhomogenitäten erfährt, oder es im Falle einer geringeren Polarisierbarkeit von den Feldinhomogenitäten abgestoßen wird. Die Polarisierbarkeit ist eine komplexe Größe, in die sowohl die dielektrische Konstanten  $\varepsilon$  und Leitfähigkeiten  $\sigma$  des Teilchens und der Flüssigkeit eingehen als auch die Frequenz des elektrischen Wechselfeldes  $\omega = 2\pi f$  und die Geometrie des Teilchens. Die Richtung der dielektrophoretischen Kraft kann sich deshalb auch mit der Feldfrequenz ändern, so dass ein Teilchen bei niedrigen Frequenzen eine positive und bei hohen Frequenzen eine negative DEP erfährt und umgekehrt.

Mit Hilfe von Dielektrophorese können Kohlenstoff-Nanoröhren gezielt in einer Lücke zwischen zwei Elektroden platziert werden. Unter bestimmten Bedingungen kommt es dabei zu einer Selbstbegrenzung der Deposition, so dass zu einem großen Anteil jeweils eine Nanoröhre pro Kontakt deponiert wird. Neben der gezielten Platzierung und Kontaktierung erlaubt Dielektrophorese auch die Trennung von metallischen und halbleitenden Kohlenstoff-Nanoröhren aufgrund ihrer dielektrischen Eigenschaften. Wird Dielektrophorese auf eine Suspension angewandt, in der Nanoröhren mit Hilfe eines Tensids vereinzelt wurden, so erfahren metallische Kohlenstoff-Nanoröhren eine positive DEP im gesamten Frequenzbereich, halbleitende Nanoröhren jedoch erfahren für Frequenzen oberhalb einer Grenzfrequenz im RF-Bereich eine negative DEP. Dadurch können überwiegend metallische Nanoröhren auf interdigitalen Mikroelektroden abgeschieden werden, während die halbleitenden Kohlenstoff-Nanoröhren in der Suspension verbleiben. Für zukünftige Anwendungen muss dieser Prozess hochskaliert werden, so dass er auf größere Mengen von Nanoröhren-Suspensionen angewandt werden kann. Da große Feldstärken und große Feldinhomogenitäten wesentliche Voraussetzungen für eine effiziente Separation mit Dielektrophorese sind, ist das Hochskalieren keineswegs trivial und erfordert grundlegende experimentelle Studien.

Im ersten Teil dieser Arbeit wurde die dielektrophoretische Deposition von einwandige Kohlenstoff-Nanoröhren auf interdigitalen Mikroelektroden untersucht. Die Verwendung von Aluminium als Elektrodenmaterial erhöht aufgrund der natürlichen Oxidschicht die Ausbeute an deponierten Kohlenstoff-Nanoröhren deutlich und erlaubt die Herstellung von kompakten Filmen aus Nanoröhren mit einer Dicke von bis zu 100 nm. Die Anwendung von sehr großen elektrischen Felder während der Deposition – die zu der gerade genannten Zunahme der deponierten Nanoröhren beiträgt – führt zur Abscheidung von halbleitenden Kohlenstoff-Nanoröhren auch oberhalb der zuvor bestimmten Grenzfrequenz. Außerdem besitzen die metallischen und halbleitenden Nanoröhren auf der Probe eine signifikant unterschiedliche Ausrichtung, die durch polarisationsabhängige Absorptionsspektroskopie analysiert wurde: metallische Kohlenstoff-Nanoröhren sind parallel zur Richtung des elektrischen Felds während der Deposition ausgerichtet, halbleitende

Nanoröhren hingegen sind willkürlich orientiert. Aus dieser Beobachtung lassen sich zwei wichtige Schlüsse ableiten: die Nanoröhren werden einzeln deponiert, d. h. die Einzelrohr-Suspensionen sind auch in hohen elektrischen Feldern stabil, und obwohl beide elektronischen Arten eine positive DEP erfahren, ist ihre Reaktion auf die dielektrophoretischen Felder doch deutlich unterschiedlich.

Um diese experimentellen Ergebnisse zu erklären, wurde das Modell überarbeitet, das bisher für die Dielektrophorese von Kohlenstoff-Nanoröhren verwendet wurde. Dieses Modell beschreibt die DEP von stabförmigen Objekten unter der Annahme einer bestimmten festen Ausrichtung des Objekts in Relation zum elektrischen Feld. Das in dieser Arbeit eingeführte erweiterte Modell erlaubt eine willkürliche Ausrichtung, die durch das Verhältnis zwischen dem dielektrophoretischen Drehmoment und der thermischen Energie bestimmt wird. Das konventionelle Modell berücksichtigt außerdem nur die dielektrischen Eigenschaften in Richtung der langen Achse des Teilchens. Kohlenstoff-Nanoröhren besitzen aber eine ausgeprägte Anisotropie sowohl in ihrer Geometrie als auch in ihren dielektrischen Eigenschaften; dies wurde explizit in das erweiterte Modell integriert. Der neue Formalismus wurde verwendet, um die Ausrichtung von metallischen und halbleitenden Nanoröhren als Funktion der Stärke und der Frequenz des elektrischen Felds zu berechnen. Bei geringen Feldfrequenzen zeigen beide Arten ein ähnliches Verhalten, bei großen Frequenzen jedoch ergeben sich deutliche Unterschiede: Im Fall der metallischen Kohlenstoff-Nanoröhren sind moderate Feldstärken ausreichend, um eine geordnete Phase mit einem hohen Grad der Ausrichtung zu erzeugen. Bei halbleitenden Nanoröhren ist die ungeordnete Phase bis zu deutlich höheren Feldstärken erhalten und bei einer weiteren Zunahme der Feldstärke wird ein Übergang zwischen zwei verschiedenen geordneten Phasen vorhergesagt. Auf der Grundlage des erweiterten Dielektrophorese-Modells wurden die Ergebnisse der polarisationsabhängigen Absorptionsspektroskopie gefittet, wobei sich eine sehr gute Übereinstimmung zwischen den Messwerten und dem Fit ergab. Der experimentelle Befund, dass halbleitende Kohlenstoff-Nanoröhren bei sehr großen elektrischen Feldern auch oberhalb der Grenzfrequenz deponiert werden, wurde durch eine Finite Elemente Simulation untersucht. Die Ergebnisse der Rechnung verdeutlichen, dass halbleitende Nanoröhren in einem gewissen Frequenzbereich, der durch die dielektrischen Eigenschaften der Nanoröhren festgelegt wird, eine positive Dielektrophorese ausschließlich aufgrund ihrer orthogonalen Polarisierbarkeit erfahren, die in früheren Rechnungen vernachlässigt wurde.

Zur Erklärung von experimentellen Ergebnissen, die am Institut für Nanotechnologie (INT) erzielt wurden, wurden weitere Finite Elemente Simulationen durchgeführt. Ein Experiment beschäftigte sich mit der Deposition von kurzen Kohlenstoff-Nanoröhren zwischen Goldelektroden, die entweder auf isolierendem Quarz-Glas oder auf oxidiertem leitfähigem Silizium-Substrat strukturiert wurden. Eine Simulation der dielektrophoretischen Kraftfelder für beide Strukturen zeigt, dass die Anwesenheit eines leitfähigen Substrats zu einer Abstoßung der

Kohlenstoff-Nanoröhren im Zentrum der Lücke zwischen dem Elektrodenpaar führt, während im Fall des isolierenden Substrats ausschließlich attraktive Kräfte in der Lücke vorliegen. In Übereinstimmung mit diesen Ergebnissen zeigen die Experimente ein substrat-spezifisches Depositionsmuster der Nanoröhren in der Elektrodenlücke.

Die Selbstbegrenzung, die bei der gezielten Platzierung von Nanoröhren zwischen Elektrodenpaaren auftritt, wurde in früheren Arbeiten durch einen Kurzschluss des Potentials in Anwesenheit der Nanoröhre und eine dadurch bedingte Abnahme der dielektrophoretischen Kraft erklärt. Am INT durchgeführte Impedanzmessungen deuten an, dass diese Erklärung unzureichend ist, und ein alternativer Mechanismus wurde vorgeschlagen, der auf einer Änderung der elektrischen Felder beruht. Die Verteilung des elektrischen Potentials und der dielektrophoretischen Kraftfelder in der Elektrodenlücke, die in Finite Elemente Simulationen berechnet wurden, unterstützen diese Erklärung: In Abwesenheit einer Kohlenstoff-Nanoröhre zwischen den Elektroden liegt eine attraktive dielektrophoretische Kraft in der Elektrodenlücke vor. Die Deposition einer Nanoröhre führt zu starken repulsiven Kräften in diesem Bereich, die die Deposition einer weiteren Nanoröhre verhindern. Die Änderung der dielektrophoretischen Kraftfelder basiert auf der sehr großen Permittivität des Nanoröhren-Tensid-Komplexes im Vergleich zur Permittivität der umgebenden wässrigen Lösung.

Die Betrachtung von Bauteilen mit einzelnen Nanoröhren mit dem Rasterelektronenmikroskop und der Ansatz, Spannungs-Kontrast Rasterelektronenmikroskopie zur Charakterisierung der elektronischen Eigenschaften von Kohlenstoff-Nanoröhren zu verwenden, motivieren eine weitere Finite Elemente Simulation. Experimente am INT zeigten, dass die Kontraständerung von Bauteilen mit einzelnen Nanoröhren bei Variation der Gate-Spannung vom elektronischen Typus der Nanoröhre abhängt. Zur Erklärung wurde zunächst der Kontrastunterschied zwischen einer nicht kontaktierten und einer geerdeten Elektrode untersucht, indem das elektrische Potential und Feld für beide Anordnungen berechnet wurde. Elektrisch nicht kontaktierte ("floatende") Elektroden nehmen ein ähnliches Potential wie das Substrat an und erzeugen deshalb keine Feldverzerrungen. Geerdete Elektroden hingegen verursachen starke Feldverzerrungen in ihrer Umgebung. Deshalb ist der Kontrast einer floatenden Elektrode dem des Substrats sehr ähnlich, während eine geerdete Elektrode je nach der Polarität der Gate-Spannung heller oder dunkler als das Substrat erscheint. Nun wurde die Kontraständerung einer Kohlenstoff-Nanoröhre modelliert, die zwischen einer geerdeten und einer ansonsten elektrisch floatenden Elektrode deponiert ist. Dabei wurde angenommen, dass sich die Permittivität einer halbleitenden Nanoröhre unter dem Einfluss der Gate-Spannung ändert. Für kleine Permittivität ergibt sich ein vernachlässigbarer Einfluss der Nanoröhre auf das Potential der floatenden Elektrode. Mit zunehmender Permittivität verstärkt sich dieser Einfluss, bis schließlich für eine halbleitende Kohlenstoff-Nanoröhre im ON-Zustand oder eine metallische

Nanoröhre die floatende Elektrode vollständig über die Nanoröhre an die geerdete Elektrode gekoppelt ist. Die berechneten Potentialverteilungen zeigen eine gute Übereinstimmung mit den experimentellen Beobachtungen.

Das in dieser Arbeit vorgestellte erweiterte Dielektrophorese-Modell sagt deutliche Unterschiede in der Ausrichtung von metallischen und halbleitenden Kohlenstoff-Nanoröhren in elektrischen Feldern voraus, wobei der Grad der Ausrichtung eindeutig von den dielektrischen Eigenschaften bestimmt wird. Im Umkehrschluss bedeutet das, dass eine Untersuchung der Ausrichtung der Nanoröhren unter Variation der Feldparameter (Frequenz und Feldstärke) die Bestimmung der dielektrischen Eigenschaften erlauben sollte. Dazu wurde ein Experiment konzipiert, in dem die Absorption von suspendierten Nanoröhren als Funktion der Feldparameter gemessen wird. Aufgrund eines starken Depolarisationseffektes senkrecht zur Röhrenachse absorbieren Kohlenstoff-Nanoröhren fast ausschließlich Licht, das entlang ihrer Achse polarisiert ist. Metallische und halbleitende Nanoröhren erzeugen dabei eindeutige und unabhängige Signaturen im Absorptionsspektrum. Deshalb ist es möglich, anhand der Veränderung der Absorptionsspektren mit dem angelegten Feld die Ausrichtung der beiden elektronischen Typen zu bestimmen. Erste Ergebnisse bestätigen eine Änderung der Absorptionsspektren, wenn ein elektrisches Feld angelegt wird. Im Vergleich zu der Absorption ohne angelegtes Feld zeigt die relative Absorbanz – und damit die Ausrichtung der Nanoröhren – qualitativ die erwartete Abhängigkeit vom elektrischen Feld. Der Effekt ist jedoch nur schwach und tritt gleichermaßen für metallische wie für halbleitende Kohlenstoff-Nanoröhren auf. Ein Erklärungsansatz besteht in einer Degradation des elektronischen Systems der metallischen Nanoröhren, die sich daraufhin wie halbleitende Nanoröhren verhalten – Anzeichen für eine solche Degradation wurden schon in früheren Experimenten am INT beobachtet, wo bei dielektrophoretischen Depositionen bei hohen Frequenzen gelegentlich keine Kohlenstoff-Nanoröhren abgeschieden werden konnten. Dabei ist ein Zusammenhang mit dem Alter der verwendeten Nanoröhren-Suspensionen möglich. Für eine abschließende Interpretation und zum Nachweis eines Alterungseffektes muss die Messung der feldabhängigen Absorption wiederholt werden. In diesem Zusammenhang ist auch die Verwendung von nicht-ionischen Lösungsmitteln vielversprechend. Es wird erwartet, dass neben den deutlich unterschiedlichen dielektrischen Eigenschaften eines nicht-ionischen Lösungsmittels im Vergleich zu den bisher verwendeten Tensiden auch die Oberflächenleitfähigkeit von halbleitenden Kohlenstoff-Nanoröhren wesentlich reduziert wird. Dadurch wird sich das Verhalten der Nanoröhren unter Dielektrophorese insgesamt stark ändern, was möglicherweise die Messung der feldabhängigen Ausrichtung erleichtern wird.

Planare Elektrodenstrukturen sind zum Hochskalieren der dielektrophoretischen Separation nicht gut geeignet, da einerseits das dielektrophoretische Kraftfeld exponentiell mit dem Abstand zur Probenoberfläche abfällt und außerdem auf der Oberfläche deponierte metallische Kohlenstoff-Nanoröhren das Feld abschirmen

und somit weiter abschwächen. Ein möglicher Ansatz zum Hochskalieren besteht in der Verwendung der elektrodenlosen Dielektrophorese. Dabei werden zwei Flüssigkeitsvolumina durch eine isolierende Membran getrennt, die ein oder mehrere Löcher aufweist. Wird ein homogenes elektrisches Feld derart an die Flüssigkeit angelegt, dass der Feldvektor senkrecht zur Membran steht, so wird das elektrische Feld durch die Verengung "eingeschnürt" und es entstehen lokale Feldverzerrungen im Bereich der Löcher. Die zugehörigen dielektrophoretischen Kraftfelder sind auf den Nahbereich der Membran beschränkt und eine zusätzliche Antriebskraft ist erforderlich, um in der Flüssigkeit enthaltene Partikel in den Einflussbereich der dielektrophoretischen Kraft zu bringen. Eine feine Justage der Antriebskraft im Verhältnis zur DEP-Kraft sollte es ermöglichen, mit einer solchen Anordnung metallische und halbleitende Kohlenstoff-Nanoröhren zu trennen. Um die Machbarkeit dieses Ansatzes zu testen, wurde eine Messzelle entworfen und der Einfluss von Gleich- oder Wechselspannung und hydrostatischem Druck auf den Transport von Kohlenstoff-Nanoröhren durch die Löcher der Membran untersucht; die Löcher weisen hierbei einen Durchmesser von 10–100 nm auf. Nachdem eine Halbzelle mit Nanoröhren-Suspension ("Nanoröhren-Seite") und die andere mit einer gleichartigen Tensidlösung ("Seifenseite") befüllt wurde, erlaubt eine in Situ-Messung der optischen Absorption die Detektion der Translokation von Kohlenstoff-Nanoröhren durch die Membran. Durch Messung der elektrophoretischen Mobilität wurde gezeigt, dass Kohlenstoff-Nanoröhren in Tensidlösung eine negative Oberflächenladung besitzen. Um eine Antriebskraft von der Nanoröhren zur Seifenseite zu erzeugen, wurde eine positive Gleichspannung an der Seifenseite angelegt. Es stellte sich heraus, dass in den Nanoporen der Membran ein elektroosmotischer Fluss entsteht, der der erwarteten Bewegung der Nanoröhren entgegengerichtet ist und dadurch die Anwendung einer Gleichspannung zum Erzeugen einer Antriebskraft hinfällig macht. Die Applikation von hydrostatischem Druck hingegen bewirkt einen effizienten Transport der Kohlenstoff-Nanoröhren durch die Membran; innerhalb der experimentell zugänglichen Grenzen erwies sich dieser Transport als unabhängig von einer angelegten Wechselspannung und eine Trennung der Nanoröhren fand nicht statt. Experimente, in denen die Antriebskraft ausschließlich auf Diffusion basierte, offenbarten einen bevorzugten Transport von Nanoröhren mit kleinem Durchmesser und metallischen Nanoröhren. Die Durchmesserselektivität stellte sich als intrinsisch für den diffusiven Transport von Kohlenstoff-Nanoröhren durch die Nanoporen heraus. Die Anreicherung an metallischen Nanoröhren wurde auch in Abwesenheit einer Wechselspannung beobachtet und ist deshalb offensichtlich nicht ausschließlich durch Dielektrophorese bedingt; die genaue Bestimmung der Ursachen erfordert weitere Untersuchungen. Diese ersten Ergebnisse zeigen, dass die elektrodenlose Dielektrophorese nach einer Optimierung der Prozessparameter möglicherweise ein Hochskalieren der dielektrophoretischen Separation erlaubt. Auch hier verspricht die Verwendung von nicht-ionischen Lösungsmitteln neue Einblicke.

# Contents

|  |           |
|--|-----------|
| <b>1. Introduction</b>   | <b>3</b>  |
| <b>2. Theoretical framework</b>  | <b>7</b>  |
| 2.1. Single-walled carbon nanotubes (SWNTs)  | 7         |
| 2.1.1. Structure of SWNTs  | 7         |
| 2.1.2. Electronic properties of SWNTs  | 9         |
| 2.1.3. Optical characterization of SWNTs   | 16        |
| 2.1.4. Fabrication and processing of SWNTs   | 19        |
| 2.2. Dielectrophoresis (DEP)   | 23        |
| 2.2.1. Basic theory of dielectrophoresis   | 23        |
| 2.2.2. Dielectrophoresis of SWNTs  | 26        |
| 2.3. Finite element simulations  | 29        |
| 2.3.1. Principles of finite element simulation   | 30        |
| 2.3.2. The FlexPDE package   | 32        |
| 2.3.3. Choice of the partial differential equation and appropriate boundary conditions | 34        |
| <b>3. Absorption spectra of thin films of SWNTs</b>                                    | <b>37</b> |
| 3.1. Experimental  | 37        |
| 3.1.1. Dielectrophoretic deposition of SWNTs onto interdigitated electrodes            | 37        |
| 3.1.2. Morphology of the samples   | 39        |
| 3.1.3. Impedance spectroscopy of the electrode arrays                                  | 40        |
| 3.2. Results and discussion  | 44        |
| 3.2.1. Polarization dependent absorbance spectra of SWNT films                         | 44        |
| 3.2.2. Advanced model for nanotube dielectrophoresis                                   | 47        |
| 3.2.3. Application to the experimental results   | 51        |
| <b>4. Finite element simulations</b>   | <b>55</b> |
| 4.1. Probing dielectrophoretic force fields with metallic carbon nanotubes             | 55        |
| 4.2. Ultra-large-scale directed assembly of SWNT devices                               | 59        |
| 4.3. Influence of structural and dielectric anisotropy on the DEP of SWNTs             | 65        |
| 4.4. Nanotube devices with floating electrodes for voltage-contrast SEM                | 68        |

---

|  |            |
|--|------------|
| <b>5. Field-dependent absorption spectra of dispersed SWNTs</b>            | <b>75</b>  |
| 5.1. Experimental setup . . . . .  | 76         |
| 5.2. Results and discussion . . . . .                                      | 78         |
| <b>6. Transport of SWNTs through nanopores</b>                             | <b>83</b>  |
| 6.1. Experimental . . . . .  | 87         |
| 6.1.1. Experimental setup . . . . .  | 87         |
| 6.1.2. Impedance spectroscopy of the DEP cell . . . . .                    | 89         |
| 6.2. Results and discussion . . . . .                                      | 91         |
| 6.2.1. Experiments with DC voltage . . . . .                               | 91         |
| 6.2.2. Experiments with AC voltage . . . . .                               | 94         |
| <b>7. Summary and outlook</b>  | <b>99</b>  |
| <b>A. Characterization of the nanotube suspensions</b>                     | <b>103</b> |
| <b>B. Additional information on films of SWNTs</b>                         | <b>107</b> |
| <b>C. The effective dipole moment in a global coordinate system</b>        | <b>113</b> |
| <b>D. Additional information on the field-dependent absorption spectra</b> | <b>115</b> |
| <b>E. Electrophoretic mobility of SWNTs</b>                                | <b>121</b> |
| <b>List of Figures</b>   | <b>125</b> |
| <b>Bibliography</b>  | <b>129</b> |
| <b>Publications</b>  | <b>139</b> |

# 1. Introduction

Since the early 1980s a significant increase of research activities in the field of nanotechnology has taken place. This was triggered on the one hand by the invention of new analytic tools—like the scanning tunneling microscope (STM) in 1981 [1] and the atomic force microscope (AFM) in 1986 [2]—that allow for the observation of new phenomena and the refinement of lithography towards smaller sizes, now enabling the fabrication and manipulation of nano-scale devices. On the other hand the enhancement of computer power and the exponentially growing production costs demand for new solutions involving the integration of novel materials into electronic devices. The interaction between fundamental research and future industrial applications explains the rapid growth of this interdisciplinary field of science.

Among the new materials under investigation, carbon nanotubes are one of the most intensively studied. After the discovery of fullerenes in 1985 [3], in 1991 multi-walled carbon nanotubes were observed to grow at the carbon cathode during the arc-discharge synthesis of fullerenes [4]. Two years later single-walled carbon nanotubes (SWNTs) were found to form in the gas phase of a similar process [5].

Single-walled carbon nanotubes are hollow cylinders made of carbon. A SWNT can be considered to consist of a single graphene sheet rolled up into a seamless cylinder. Such a nanotube is a unique molecular system due to several reasons [6, 7]: with a typical diameter of  $\sim 1$  nm and a length up to 1 cm, nanotubes yield a hitherto unmatched aspect ratio; they show little structural disorder and are chemically inert; depending on the direction about which the graphene is rolled into a cylinder, single-walled carbon nanotubes exist in two electronic manifestations—they can be either metallic or semiconducting; in addition, they exhibit outstanding mechanical properties, like very high tensile strength and elastic modulus.

From the viewpoint of fundamental science, a single-walled carbon nanotube is a quasi-one-dimensional—conducting or semiconducting—system that offers the possibility to verify theoretical predictions of, for example, the electronic and thermal transport properties. Regarding future implementations, SWNTs are promising candidates for a wide range of applications, e. g. as building blocks in molecular electronics [8] or as field emitters [9]. Currently, nanotubes are already used as additive to the graphite component in Li-ion batteries and as reinforcement of composite materials [10].

For an efficient integration of single-walled carbon nanotubes into electronic devices several problems have to be overcome. One of them is the lack of a selective growth process—so far no synthesis method exists that allows to control the chirality and therefore the electronic type of the nanotubes. However, some of the future applications require samples containing only metallic or only semiconducting nanotubes; therefore a separation process is essential. Another obstacle is the precise and reproducible assembly of individual nanotubes within an electronic circuit. Current device fabrication often involves a random dropping of nanotubes onto pre-defined electrodes, or else, electrodes are lithographically structured onto nanotubes which were before randomly deposited and located on a substrate. The use of AC (alternating current) dielectrophoresis led to a substantial progress in both the separation of metallic and semiconducting nanotubes and their controlled assembly in electronic devices [11, 12].

Dielectrophoresis describes the motion of polarizable particles dispersed in liquid media under inhomogeneous external electric fields [13]. Unlike electrophoresis, dielectrophoresis does not require the particles to be charged—when using solely AC fields, the force acting on the particle is independent of the charge. Instead it is determined by the size and geometry and the dielectric properties of the particle: a particle that is more polarizable than its surrounding medium undergoes positive dielectrophoresis, i. e. the particle is attracted towards regions of high field inhomogeneity, while a particle which is less polarizable experiences negative dielectrophoresis, i. e. it is repelled from these regions. The polarizability of a particle is a complex function, the Clausius-Mossotti function, which depends on the permittivity  $\varepsilon$  and the conductivity  $\sigma$  of the particle and the surrounding medium as well as on the frequency  $f$  of the electric field and the particle's size and shape. As a consequence, the direction of the dielectrophoretic force exerted on a particle can vary with the field frequency, such that a particle might experience positive dielectrophoresis at low frequencies and negative dielectrophoresis at high frequencies or the other way around.

Already in the 1960s, dielectrophoresis was used for the manipulation and collection of cells and other micrometer particles [14]. Only recently, due to the advances in lithography techniques, the generation of sufficiently high electric fields was possible that allow to manipulate sub-micrometer particles. From 1990 on, a wide range of particles like DNA [15], proteins [16], latex particles [17] and viruses [18] have been collected and manipulated by dielectrophoresis. Additionally, it was demonstrated that dielectrophoresis allows for the separation of heterogeneous populations of viruses [19] and latex spheres [20] according to their dielectric properties (for an overview see also Reference [21]).

AC dielectrophoresis was first introduced in 2003 as a tool to assemble and contact bundles of individual single-walled carbon nanotubes [22]. When using surfactant-stabilized suspensions of individual carbon nanotubes, a self-limiting deposition process was observed resulting in devices which contain single carbon

---

nanotubes [12,23]. Recently, this technique was employed to produce high-density arrays of individual single-walled carbon nanotube devices [24]. These experimental results indicate an important step towards a precise and reproducible integration of carbon nanotubes into electronic devices.

Furthermore, dielectrophoresis was presented as the first method to nondestructively sort single-walled carbon nanotubes according to their electronic type [11]. While both electronic types experience a positive dielectrophoretic force for low electric field frequencies, semiconducting nanotubes undergo negative dielectrophoresis and metallic nanotubes undergo positive dielectrophoresis in the high-frequency regime [25]. The use of interdigitated micro-electrodes allows to deposit thin films of predominantly metallic nanotubes onto the sample surface, while semiconducting nanotubes remain in the suspension [26]. There have been several reports regarding a method to upscale the dielectrophoretic separation process, e. g. by using macroscopic electrodes [27], filtration [28], microfluidic setups [29] and dielectrophoresis field flow fractionation [30]. However, the fact that inhomogeneous fields are a prerequisite for an efficient dielectrophoresis process implies that an upscaling of the separation is non-trivial and further work is necessary in this context.

In this work fundamental aspects of nanotube dielectrophoresis are treated, regarding both its application for separation as well as assembly. This thesis is structured as follows: In **Chapter 2** the theoretical framework is presented which is necessary to comprehend the measurements and interpretations given in the subsequent chapters. This involves a summary of the basic properties of single-walled carbon nanotubes as well as a short introduction into dielectrophoresis and finite element simulations.

**Chapter 3** focuses on the properties of continuous films of single-walled carbon nanotubes which are produced by dielectrophoretic deposition onto interdigitated electrodes using very large electric fields. The experimental procedure is described and the sample characterization is presented. Polarization dependent absorption spectra measured on the nanotube films reveal a significant difference in the alignment of metallic and semiconducting nanotubes. Furthermore, semiconducting nanotubes are observed to deposit at frequencies higher than the cross-over frequency observed before. To explain these results, an advanced model for carbon nanotube dielectrophoresis is introduced, which explicitly incorporates the structural and dielectric anisotropy of single-walled carbon nanotubes. On the basis of this model, the average alignment of metallic and semiconducting nanotubes under the experimental conditions is predicted and compared to the experimental findings.

To optimize the experimental setups for dielectrophoretic assembly or separation of single-walled carbon nanotubes a profound understanding of the dielectrophoretic force fields is required. **Chapter 4** provides an overview of finite element simulations which were performed for this purpose. The calculations presented

here were essential for the understanding of experimental results obtained at the Institute for Nanotechnology, INT.

According to the model discussed in Chapter 3, the alignment of dispersed single-walled carbon nanotubes exposed to an external electric field is a function of the properties of the electric field and of the nanotubes. Therefore, monitoring the degree of alignment under variation of the field strength and frequency allows to determine the dielectric properties of the nanotubes under investigation. In **Chapter 5** an experimental setup to measure *in situ* the absorbance spectra of suspended carbon nanotubes exposed to AC electric fields is presented. The evolution of the absorption with the applied voltage—which is a measure for the electronic-type-specific alignment—is examined and compared to the theoretical predictions.

The concept of electrodeless dielectrophoresis might offer the possibility to up-scale the dielectrophoretic separation of single-walled carbon nanotubes. In electrodeless dielectrophoresis an—initially homogeneous—electric field in a conducting liquid is generated between two macroscopic electrodes. An insulating material is placed between the electrodes, and channels through the insulator are used to confine the electric field, thereby creating high local field inhomogeneities. An experimental setup to study the applicability of this concept for nanotube dielectrophoresis is introduced in **Chapter 6**. The translocation of nanotubes through nanopores is monitored by means of absorption spectroscopy and the influence of DC and AC voltages as well as hydrostatic pressure is investigated.

In **Chapter 7** this work is summarized and an outlook towards future investigations is given.

## 2. Theoretical framework

### 2.1. Single-walled carbon nanotubes (SWNTs)

Since their discovery in 1993 by Iijima [5], single-walled carbon nanotubes (SWNTs) are in the focus of interest of both experimentalists and theoreticians due to the outstanding properties of these one-dimensional systems, e.g. their mechanical stability and their electronic properties ranging from metallic to semi-conducting character. In the following sections a short introduction into the basic properties of single-walled carbon nanotubes is presented.

#### 2.1.1. Structure of SWNTs

A single-walled carbon nanotube can be constructed geometrically from a graphene sheet, i.e. a single layer of graphite. In a graphene sheet the carbon atoms are placed on a hexagonal lattice, thus forming a honeycomb structure. Figure 2.1 shows the unit cell and the Brillouin zone of graphene. The unit cell is spanned by the graphene lattice vectors  $\vec{a}_1$  and  $\vec{a}_2$  with  $|\vec{a}_1| = |\vec{a}_2| = a_0 = 2.461 \text{ \AA}$ . The graphene lattice constant  $a_0$  is related to the distance between neighboring carbon sites  $a_{cc}$  by  $a_0 = \sqrt{3} \cdot a_{cc} \cong \sqrt{3} \cdot 1.42 \text{ \AA}$ . The vectors  $\vec{b}_1$  and  $\vec{b}_2$  are the reciprocal lattice vectors.

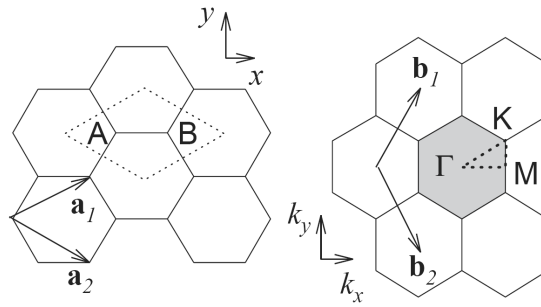


**Figure 2.1:** 2d graphene in real (left) and reciprocal space (right). The vectors  $\vec{a}_{1,2}$  and  $\vec{b}_{1,2}$  are the basic vectors and reciprocal lattice vectors. The unit cell (dotted rhombus) contains two carbon atoms on sites  $A$  and  $B$ . The high symmetry points  $\Gamma$ ,  $K$ ,  $M$  within the Brillouin zone (shaded hexagon) are indicated. From Ref. [31].

As depicted in Figure 2.2, a SWNT is modeled by taking a rectangular section

of the graphene sheet and rolling it into a hollow cylinder. The unit cell of the nanotube is spanned by the chiral vector  $\vec{C}_h$ , connecting two equivalent atomic sites on the circumference perpendicular to the cylinder axis, and the translational vector  $\vec{T}$ , which marks the translational period along the axis. While there are an infinite number of possibilities to roll the graphene sheet into a cylinder, every individual nanotube can be uniquely specified by its chiral indices  $(n, m)$ , which define the chiral vector in terms of the graphene lattice vectors  $\vec{a}_1$  and  $\vec{a}_2$ :  $\vec{C}_h = n\vec{a}_1 + m\vec{a}_2$ . The diameter of a nanotube can be derived from the length of the chiral vector as

$$d = |\vec{C}_h|/\pi = \frac{a_0}{\pi} \sqrt{n^2 + nm + m^2}. \quad (2.1)$$

The typical diameter of a single-walled carbon nanotube is  $\sim 1$  nm. The angle  $\Theta$  between  $\vec{C}_h$  and  $\vec{a}_1$ , which is called the chiral angle, can be calculated as follows

$$\cos \Theta = \frac{\vec{C}_h \cdot \vec{a}_1}{|\vec{C}_h| |\vec{a}_1|}. \quad (2.2)$$

Due to the rotational symmetry of the graphene lattice, the value of the chiral angle can be restricted to  $0 \leq \Theta \leq 30^\circ$ , corresponding to a restriction of the chiral indices to  $n \geq m \geq 0$ . Nanotubes with  $m = 0$  ( $\Theta = 0^\circ$ ) are called zig-zag tubes, because the atoms form a zig-zag pattern along the circumference. Nanotubes of the type  $(n, n)$  ( $\Theta = 30^\circ$ ) exhibit an armchair pattern along the circumference and are therefore called armchair tubes. While zig-zag tubes display carbon-carbon bonds parallel to the nanotube axis, armchair tubes display bonds perpendicular to the tube axis.

Nanotubes with  $m \neq n \neq 0$  are chiral tubes, whereas zig-zag and armchair tubes are achiral. The translational period  $t = |\vec{T}|$  varies strongly with the chirality: chiral nanotubes often have very large unit cells, whereas in the case of armchair and zig-zag nanotubes the length of the translational vector is  $t = a_0$  and  $t = \sqrt{3} \cdot a_0$ , respectively.

To derive the electronic properties of a single-walled carbon nanotube it is essential to know the Brillouin zone in the reciprocal space. Just as the unit cell spanned by  $\vec{C}_h$  and  $\vec{T}$  is unique for any pair of  $(n, m)$ , the Brillouin zone is unambiguously defined by the vectors  $\vec{k}_z$  along the direction of the nanotube axis and  $\vec{k}_\perp$  along its circumference. The reciprocal vectors are given by the following relations

$$\begin{aligned} \vec{k}_\perp \cdot \vec{C}_h &= 2\pi & \vec{k}_\perp \cdot \vec{T} &= 0 \\ \vec{k}_z \cdot \vec{C}_h &= 0 & \vec{k}_z \cdot \vec{T} &= 2\pi. \end{aligned} \quad (2.3)$$

Due to the high aspect ratio of a SWNT, it can be regarded to be infinitely long along its axis and the wave vector  $\vec{k}_z$  is continuous. The extension of the first Brillouin zone in  $z$ -direction is  $-\pi/t < k_z \leq \pi/t$ . The vector  $\vec{k}_\perp$ , on the other

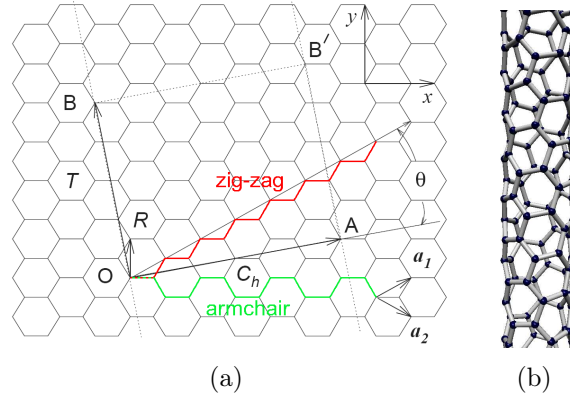


**Figure 2.2:** (a) The honeycomb lattice of graphene with lattice vectors  $\vec{a}_1$  and  $\vec{a}_2$  is shown as well as the unit cell of a (4,2) nanotube defined by the chiral vector  $\vec{C}_h$  and the translational vector  $\vec{T}$ . Highlighted in red and green are the pattern displayed along the circumference of zig-zag and armchair nanotubes, respectively. Modified from Ref. [31]. (b) Model of the (4,2) nanotube.

hand, is quantized: The wave function of any quasi-particle on the nanotube must acquire a phase shift of an integer multiple of  $2\pi$  around the circumference to allow for the formation of a standing wave. Thus, the boundary condition for  $k_\perp$  is

$$\mu \cdot \lambda = |\vec{C}_h| = \pi d \quad \Leftrightarrow \quad k_{\perp,\mu} = \frac{2\pi}{\lambda} = \frac{2}{d} \cdot \mu. \quad (2.4)$$

Here  $\mu$  is an integer related to the number of graphene hexagons in the SWNT unit cell,  $q$ , by  $\mu = -q/2, -q/2 + 1, \dots, q/2$ . The first Brillouin zone now consists of  $q$  lines of allowed  $k$ -states which are parallel to the  $z$ -axis and separated by  $k_\perp = \pi/d$ , with  $k_z \in (-\pi/t, \pi/t]$ . As an example, Figure 2.3 shows the first Brillouin zone of an armchair and a zig-zag nanotube. Note that the graphene lattice is rotated by  $30^\circ$  in the case of the zig-zag nanotube.

## 2.1.2. Electronic properties of SWNTs

Due to the generally very large number of atoms in the unit cell of a nanotube, deriving the band structure for each specific chirality through *ab initio* calculations is very time-consuming or even impossible. Instead the band structure of a SWNT is deduced from the energy dispersion of graphene by the zone-folding approximation.

### Band structure of graphene

In the hexagonal graphene lattice the four valence orbitals of the carbon atoms show planar  $sp^2$  hybridization. The  $2s$ ,  $2p_x$  and  $2p_y$  orbitals form the bonding

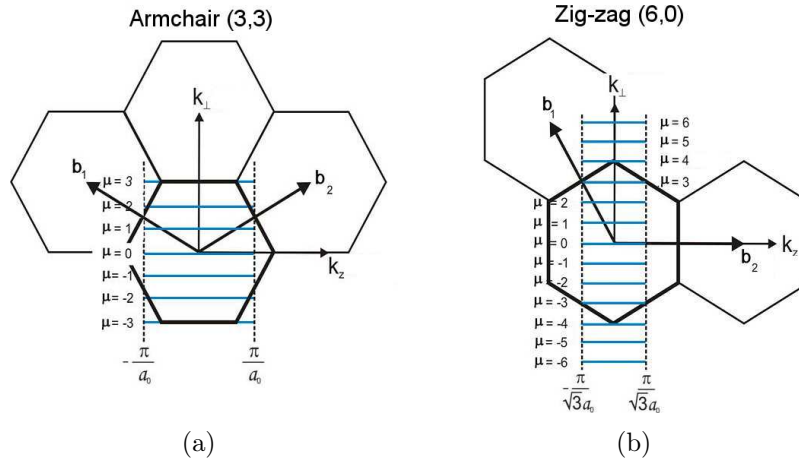


**Figure 2.3:** Schematic drawing of the first Brillouin zone of a (3,3) nanotube (a) and a (6,0) nanotube (b). Adapted from Ref. [7].

$\sigma$  and the anti-bonding  $\sigma^*$  orbitals, which are in-plane with the graphene sheet. While these  $\sigma$  orbitals are responsible for the binding energy and the elastic properties of the sheet, they are energetically far away from the Fermi level and therefore contribute very little to the electronic properties. The  $2p_z$  orbital, on the other hand, is perpendicular to the graphene sheet and through interaction with neighboring  $2p_z$  orbitals forms non-localized bonding  $\pi$  and anti-bonding  $\pi^*$  orbitals. The  $\pi$  bonds pointing out of the plane are responsible for the weak interactions between different graphene layers in graphite—or between bundled SWNTs—and play the key role in the determination of the electronic properties.

Figure 2.4 shows the electronic band structure of graphene as calculated using a tight-binding model. The  $\pi$  and  $\pi^*$  bands, corresponding to the last valence and the first conduction band, cross the Fermi level with  $E_F = 0$  at the corners of the first Brillouin zone, the high symmetry  $K$  points. This means that graphene exhibits a metallic character, but since its Fermi surface consists of only six distinct points (the  $K$  points), it is often called semimetal. Additionally, in a first approximation, the  $\pi$  bands show a linear dispersion near the  $K$  points. The  $\sigma$  and  $\sigma^*$  bands are well separated by several eV.

### Zone-folding approximation

As discussed above, the Brillouin zone of a specific single-walled carbon nanotube displays a unique set of parallel lines corresponding to the allowed  $k$  states. In the zone-folding approximation the electronic band structure of a nanotube is defined by the electronic energies of graphene along these lines,  $E_{\mu}^{\pi, \pi^*}(k_z)$ , which are projected ('folded') onto the  $\vec{k}_z$  direction. Due to the one dimensional character

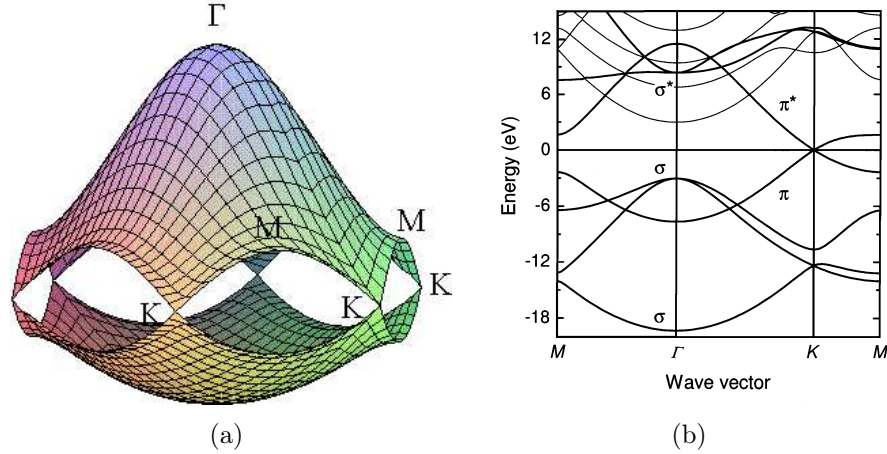


**Figure 2.4:** (a) Energy dispersion for the  $\pi$  and  $\pi^*$  bands in graphene [32]. (b) Electronic band structure of graphene along the high symmetry directions of the 2D Brillouin zone [7].

of carbon nanotubes, the resulting Brillouin zone is one dimensional as well. The wave vector  $k \equiv k_z$  defines the continuous momentum along the nanotube axis and  $\mu$  specifies the index of the allowed line. The zone edge of the Brillouin zone is generally labeled  $X$ , with  $\vec{X} = \pm(\pi/t)\vec{k}$ . Figure 2.5 illustrates this approach.

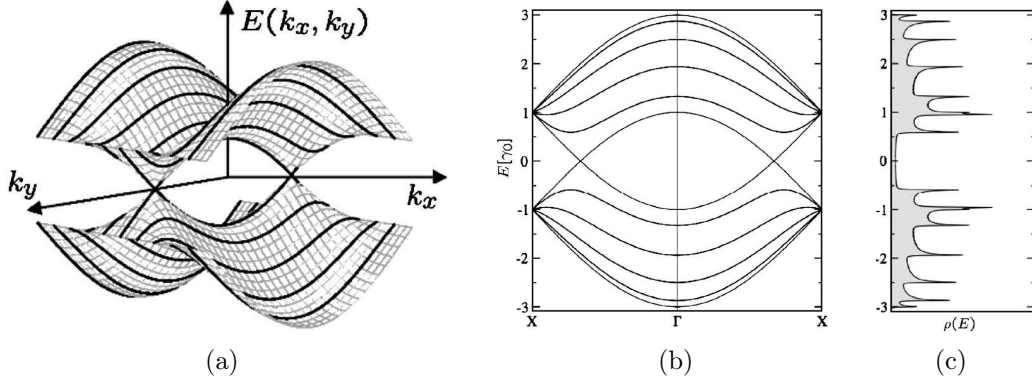


**Figure 2.5:** (a) Energy dispersion,  $E^{\pi,\pi^*}(k_x, k_y)$ , of graphene within the Brillouin zone of an armchair nanotube. In the zone-folding approach, the energy values on the lines of allowed  $k$ -states,  $E_{\mu}^{\pi,\pi^*}(k)$ , are projected onto the  $\vec{k}_z$  direction to obtain the band structure (b) and density of states (c) for a (5,5) armchair nanotube. Modified from Ref. [33].

The zone-folding technique offers a simple way to predict the electronic structure of a  $(n, m)$  nanotube. As stated above, the valence and conduction bands of graphene cross at the  $K$  point of the Brillouin zone. Only in the case where this  $K$  point lies on a line of allowed  $k$  states, does the nanotube show metallic character, else it is a semiconductor. Using Equation (2.4) and the location of the

$K$  point in the reciprocal space,  $\vec{K} = \frac{1}{3}(\vec{b}_1 - \vec{b}_2)$ , it follows

$$\begin{aligned}\vec{K} \cdot \vec{C}_h &= 2\pi\mu = \frac{1}{3}(\vec{b}_1 - \vec{b}_2) \cdot (n\vec{a}_1 + m\vec{a}_2) = \frac{2\pi}{3}(n - m) \\ \Leftrightarrow 3\mu &= n - m.\end{aligned}\quad (2.5)$$

This means that whenever  $n - m$  is an integer multiple of 3, the SWNT is metallic with a linear dispersion relation close to  $E_F$  and a non-zero density of states at the Fermi level (see Figure 2.5 (b & c)). By projecting the  $K$  point onto the nanotube axis, the value of the wave vector  $k$  at which the band crossing occurs can be predicted in a similar way. It turns out that for most metallic nanotubes, including armchair nanotubes, the crossing occurs at  $2/3 \cdot X$ , while in the case of zig-zag nanotubes the bands cross at the  $\Gamma$  point.

The condition for a semiconducting nanotube is  $n - m = 3\mu \pm 1$ . In this case, an energy gap  $\Delta E$  exists at the Fermi level, which is given in a first approximation by [33]

$$\Delta E = \frac{2\pi a_{cc}\gamma_0}{|\vec{C}_h|} = \frac{2a_{cc}\gamma_0}{d}.\quad (2.6)$$

Here,  $\gamma_0$  is the transfer integral between first neighbor  $\pi$  orbitals used in the tight-binding derivation of the energy dispersion of graphene. A typical value for  $\gamma_0$  is 2.9 eV.

### Curvature effects

The zone-folding approach gives reliable values for the electronic energies close to the Fermi level and for single-walled carbon nanotubes with  $d \geq 1.5$  nm and it also provides a general rule for the metallicity of a specific  $(n, m)$  nanotube. However, the approach treats nanotubes as stripes of graphene and neglects any curvature effects which are introduced by rolling up the graphene sheet to form a nanotube.

Placing the carbon atoms on a cylinder wall yields a difference between the carbon-carbon bonds parallel and perpendicular to the nanotube axis. As a result, the basis vectors  $\vec{a}_1$  and  $\vec{a}_2$  have different lengths and the parameter  $\gamma_0$  in the tight-binding calculation takes different values for the three neighboring atoms of the central carbon atom. Additionally the planar symmetry is broken and the  $\pi$  and  $\sigma$  states can mix to form hybrid orbitals.

These curvature effects shift the  $k_F$  point at which the  $\pi$  and  $\pi^*$  bands cross away from the Brillouin zone corners of graphene, the  $K$  point. Figure 2.6 (a) illustrates this shift for an armchair (3,3) and a zig-zag (6,0) nanotube. Obviously, in the case of the armchair nanotube the  $k_F$  point is shifted along a line of allowed states (represented by the set of green lines), which means that armchair nanotubes preserve their metallic character. For zig-zag nanotubes on the other hand, the  $k_F$  point moves perpendicular to the allowed lines and a small energy gap opens at

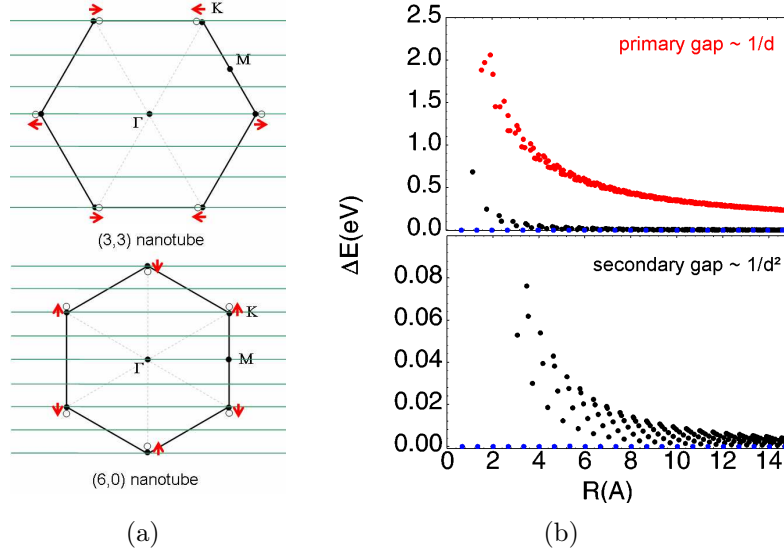


**Figure 2.6:** (a) Due to curvature effects, the Fermi point  $k_F$  ( $\circ$ ) moves away from the graphene  $K$  points as indicated by the red arrows. The direction of this shift is a function of the chirality of the nanotube. (b) Primary and secondary energy gaps calculated for small diameter SWNTs. Three types can be distinguished: nanotubes with non-zero primary gap  $\Delta E \sim 1/d$  (red dots), nanotubes with zero primary gap and secondary gap  $\Delta E_2 \sim 1/d^2$  (black dots) and armchair nanotubes with  $\Delta E = 0$  (blue dots). Modified from Ref. [34].

the Fermi energy [35, 36]. This so called secondary gap depends on the diameter and the chirality of the specific nanotubes as [33]

$$\Delta E_2 = \frac{3a_{cc}^2 \gamma_0}{4d^2}. \quad (2.7)$$

Figure 2.6 (b) shows the magnitude of the energy gaps for small-diameter nanotubes.  $(n, n)$  armchair tubes (represented by blue dots) are the only zero-band-gap nanotubes, while all  $n - m = 3\mu$  nanotubes with  $n \neq m$  (represented by black dots) exhibit a secondary gap. However, for zig-zag nanotubes fulfilling this condition  $\Delta E_2$  is very small and it suffices for most practical purposes to consider them as metallic.

For very small diameter SWNTs, e. g. nanotubes synthesized inside zeolite channels [37], the curvature effect is strong enough to allow for the rehybridization of  $\pi$  and  $\sigma$  states. In this case, the zone-folding approach fails completely and *ab initio* calculations are required for a correct description of the electronic band structure.

### Density of states

The number of available electronic states  $\Delta N$  per energy interval  $\Delta E$  with  $\Delta E \rightarrow 0$  is called the density of states,  $n(E)$ . The shape of this function depends critically

on the dimensionality of the material under investigation. If one dimensional systems exhibit energy bands that can be approximated by a parabolic shape near the extrema, the density of states consists of a set of singularities where  $n(E) \sim 1/\sqrt{E}$ , the so called van Hove singularities (vHs).

For  $i$  one dimensional electronic bands the density of states can be derived by [7]

$$n(E) \propto \sum_i \int dk \delta(k - k_i) \left| \frac{\partial E_i^\pm}{\partial k} \right|^{-1}. \quad (2.8)$$

Here  $E_i^\pm$  is the set of eigenvalues resulting from the tight binding calculation for graphene and  $k_i$  is given by the equation  $E - E_i^\pm(k) = 0$ . Figure 2.5 (c) shows the density of states for a (5,5) nanotube and clearly illustrates that the position of the van Hove peaks corresponds to points of vanishing slope in the energy dispersion in Figure 2.5 (b).

Under the assumption of linear bands near the  $K$  points in the Brillouin zone the density of states in the vicinity of the Fermi energy can be expressed by a universal relationship [38]. In this approximation the position of a vHs depends only on the electronic type of the carbon nanotube and goes with  $1/d$ , independent of the chirality. For the first van Hove peak this approach is in very good agreement with *ab initio* calculations, but for higher energies the results only qualitatively agree. The so called Kataura plot presented in Figure 2.7 shows the position of the vHs with respect to the Fermi energy as a function of the nanotube diameter as calculated with the tight binding method and illustrates how the different chiralities introduce a broadening for higher energies.

The vHs are very important for many physical properties of single-walled carbon nanotubes, because the density of states is very high at the singularities. As an example, the probability for optical absorption will be very pronounced if the energy of the incoming photon equals the difference between vHs in the valence and conduction bands. Besides optical absorption and emission measurements [39], scanning tunneling spectroscopy [40] and resonant Raman scattering [41] provide tools to verify the density of states experimentally.

## Polarizability

The electronic structure of a specific single-walled carbon nanotube, and in particular its energy gap has a major influence on the response of carbon nanotubes when exposed to an external electric field. The main response to the presence of a uniform electric field  $\vec{E}$  is the formation of an induced dipole moment  $\vec{p}$ , which is related to the electric field via the polarizability tensor  $\alpha$  by  $\vec{p} = \alpha \vec{E}$ .

The static polarizability per unit length of a  $(n, m)$  nanotube can be calculated by a method presented in Reference [42]. (The notation used in the following corresponds to that in Reference [42].) Here a tight-binding model is used to first

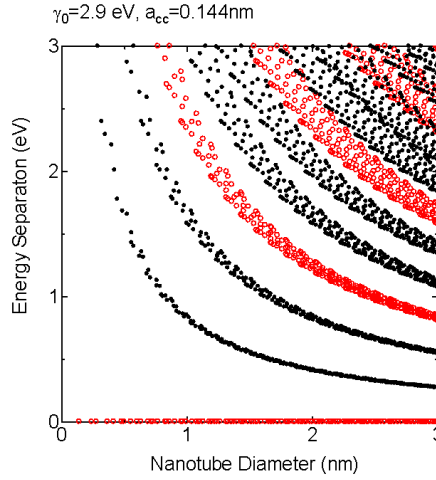


**Figure 2.7:** Kataura plot presenting the position of the van Hove singularities in the density of states of carbon nanotubes as a function of nanotube diameter as calculated using the tight-binding method. Red circles and black dots represent metallic and semiconducting nanotubes, respectively. From Ref. [32].

derive the real part of the dielectric function  $\varepsilon(\vec{q}, \omega)$  in the random phase approximation, e. g. neglecting local electric fields. From this quantity, the unscreened polarizability per unit cell,  $\alpha_0$ , is deduced according to

$$\lim_{\vec{q} \rightarrow 0} \varepsilon(\vec{q}, \omega) = 1 + \frac{4\pi}{\Omega} \alpha_0(\omega), \quad (2.9)$$

where  $\Omega$  represents the area of the unit cell and  $\vec{q}$  is the wave vector. Due to the cylindrical shape of a carbon nanotube, only two principal axes have to be considered: the  $z$  axis parallel to the nanotube axis and the  $x$  axis perpendicular to it. (As a consequence, only the  $xx$  and the  $zz$  element in the polarizability tensor will be non-zero.) By choosing  $\vec{q}$  along either of these directions and then performing  $\vec{q} \rightarrow 0$ ,  $\alpha_{0xx}$  and  $\alpha_{0zz}$  can be calculated. It follows that

$$\alpha_{0xx} \sim r^2 \quad \text{and} \quad \alpha_{0zz} \sim \frac{r}{\Delta\bar{E}}, \quad (2.10)$$

where  $r$  is the radius of the nanotube and  $\Delta\bar{E}$  is the average energy of a single-particle transition, which is of the order of the minimum direct band gap  $\Delta E$ .

In the next step a classical reasoning is used to determine the relation between the unscreened polarizability  $\alpha_0$  and the screened polarizability  $\alpha$ , which is the experimentally accessible quantity. With  $\vec{p} = \alpha\vec{E}$  and  $\vec{p} = \alpha_0\vec{E}_{\text{tot}}$ , the crucial parameter obviously is the local electric field  $\vec{E}_{\text{loc}} = \vec{E}_{\text{tot}} - \vec{E}$ . If  $\vec{E}$  points along the  $x$  direction, the existence of bound surface charges leads to a local depolarization field. Under the assumption that this local field is constant inside the nanotube,

$$\alpha_{xx} = \frac{\alpha_{0xx}}{1 + 2\alpha_{0xx}/r^2} \quad (2.11)$$

is obtained. For  $\vec{E}$  along the  $z$  direction,  $\vec{E}_{\text{loc}} = 0$  due to the absence of bound surface charges. This, of course, is only true in the approximation of an infinitely long nanotube. In the case of a finite length, charges will accumulate at the ends, thereby building up a depolarization field. However, if the length is much larger than the diameter of the nanotube this effect is negligible and therefore

$$\alpha_{zz} = \alpha_{0zz}. \quad (2.12)$$

The fact that—unlike  $\alpha_{xx}$ — $\alpha_{zz}$  remains unscreened implies that for arbitrary electric fields the induced electric dipole moment of a single-walled carbon nanotube always points primarily along the nanotube axis. As a consequence, it is expected that nanotubes will align parallel to an external field.

According to Equation (2.10), the polarizability parallel to the nanotube axis depends critically on the electronic band structure of the specific nanotube. In particular, it diverges for metallic  $(n, n)$  nanotubes with  $\Delta E = 0$ . For large-gap semiconducting nanotubes an effective  $\varepsilon_{zz} \approx 30\varepsilon_0$  can be obtained [43].  $\alpha_{xx}$ , on the other hand, is completely independent of the tube chirality and band gap.

### 2.1.3. Optical characterization of SWNTs

Optical spectroscopy, including absorbance and photoluminescence measurements, resonant Raman spectroscopy and time-resolved optical spectroscopy, provide an efficient tool to characterize the electronic properties of single-walled carbon nanotubes, provided that individual nanotubes are examined. In particular, the electronic band structure and the phonon dispersion can be probed with these techniques. However it turns out that due to the presence of excitonic effects the single-particle picture is not sufficient for a detailed analysis.

#### Absorbance spectra and photoluminescence

As stated above, the accumulation of electronic states at the van Hove singularities implies that the absorption of single-walled carbon nanotubes will be dominated by transitions between these peaks [44]. However, when the incoming light is linearly polarized, selection rules predict whether a transition between two vHs is allowed or suppressed. Due to the strong depolarization effect in SWNTs perpendicular to the nanotube axis, transitions between subbands with the same angular momentum  $\mu$  prevail in the case of light polarized parallel to the nanotube axis, yielding the  $E_{ii}$  energies [42, 45]. In this interpretation the Kataura plot (see Figure 2.7), in which the transition energies  $E_{ii}$  are mapped versus the nanotube diameter, can be used to analyze the diameter range of the nanotube sample under investigation. However for samples containing a wide selection of different  $(n, m)$  nanotubes (especially for large diameter nanotubes), a detailed analysis of the indices is not possible: The sharp absorption peaks of specific  $(n, m)$  nanotubes

with similar  $E_{ii}$  values form broad absorption features in the sample spectrum (see Figure 2.13), thus hampering the assignment. If the diameter range and chiralities present in the sample are known, the absorption spectra can be calculated [46].

When using cross-polarized light in an absorption measurement, transitions between valence and conduction bands with  $\Delta\mu = \pm 1$  are allowed. These measurements can be used to probe the asymmetry between valence and conduction bands.

Samples containing isolated SWNTs allow for the detection of photoluminescence in semiconducting nanotubes [39], as do individual nanotubes grown suspended on Si/SiO<sub>2</sub> substrates [47]. Photoluminescence maps can be measured by exciting a sample with monochromatic light in a broad energy range, e. g. covering  $E_{ii}^S, i = 1-4$ , and detecting the emitted  $E_{11}^S$  [48]. The intensity of the observed features can be related to the relative abundance of a specific  $(n, m)$  semiconducting nanotube. This method is limited to isolated semiconducting nanotubes, since non-radiative electron-hole recombination inhibits the  $E_{11}$  emission in metallic nanotubes. Therefore light emission from isolated metallic SWNTs or bundles containing both semiconducting and metallic nanotubes is strongly suppressed.

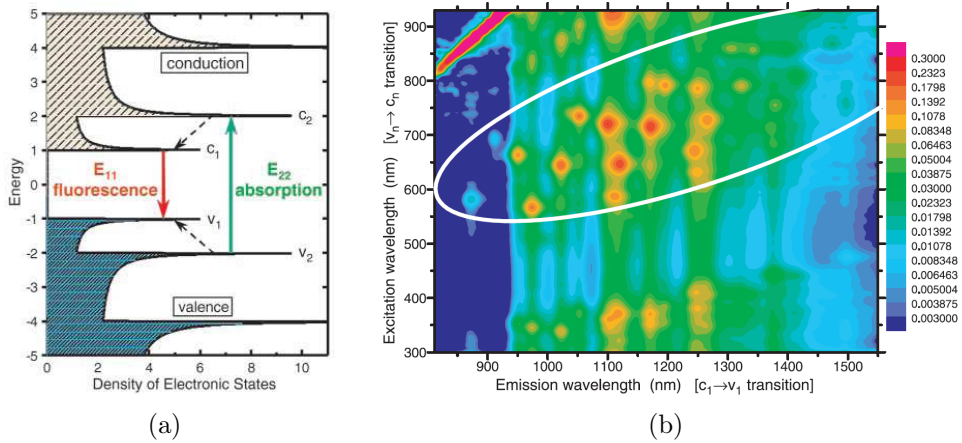


**Figure 2.8:** (a) Schematic of a photoluminescence process involving absorption via  $E_{22}$  and emission via  $E_{11}$ ; dashed arrows indicate non-radiative relaxations. (b) Photoluminescence map for SWNTs suspended in a surfactant solution. Each peak in the intensity corresponds to a  $E_{ii}$  transition of a specific  $(n, m)$  nanotube species. From Ref. [49].

Both absorption spectroscopy and photoluminescence measurements allow for a comparative analysis of different nanotube samples. An absolute population analysis, however, is not possible without a detailed knowledge of the optical absorption efficiency and the cross section for photoluminescence efficiency as a function of  $(n, m)$ . Since both the efficiency and the  $E_{ii}$  levels strongly depend on the environment, extensive studies are necessary either on the single-nanotube level or using samples with known population [6].

### Excitons in carbon nanotubes

More accurate studies reveal a systematic deviation between the peaks in the absorption spectra and the transition energies  $E_{ii}$  between vHs. Comparing the energies of one-photon and two-photon transitions in semiconducting nanotubes, it was shown that the optical properties are in fact dominated by excitonic interactions [50]. Due to the one dimensional character of single-walled carbon nanotubes, the Coulomb interaction between the optically excited electron-hole pairs is strongly enhanced with respect to bulk semiconductors. The observed binding energies are in the range of 0.3–0.4 eV, which can be correlated to a spatial extent of the ground state exciton of  $R = 1.2$  nm.

Recently, the existence of bound excitonic states was also observed for metallic carbon nanotubes [51]. However, due to enhanced screening in metallic nanotubes the calculated binding energies of  $\sim 50$  meV are much smaller than for semiconducting nanotubes of similar diameter, in good agreement with theoretical predictions [52].

### Resonant Raman spectroscopy

The inelastic scattering of light under the emission or absorption of an optical phonon is called Raman scattering [53]. By measuring the Raman spectrum of a material, i. e. measuring the intensity of the scattered light as a function of its energy loss, an accurate probe of the material's phonon frequencies is obtained. The scattering intensity is very low when the intermediate electronic states are virtual (non-resonant Raman scattering), but it is strongly enhanced if the optical absorption or emission occurs to or from a real electronic state, in which case the process is called resonant Raman scattering. In the case of single-walled carbon nanotubes, the van Hove singularities in the density of states further increase the intensity. Therefore it is possible to measure the signal of an individual nanotube fulfilling the resonance condition, which makes resonant Raman spectroscopy one of the most sensitive characterization tools available for carbon nanotubes [31]. Figure 2.9 shows Raman spectra of individual carbon nanotubes.

The two dominant Raman features of SWNTs are the radial breathing mode (RBM) with  $\omega_{\text{RBM}}$  between 120 and 350  $\text{cm}^{-1}$  for  $0.7 \text{ nm} < d < 2 \text{ nm}$  and the so called *G* band at 1550–1590  $\text{cm}^{-1}$ . The RBM corresponds to a coherent vibration of all carbon atoms in the radial direction and is unique for carbon nanotubes. It can be used to prove the presence of carbon nanotubes in a given sample and to characterize the diameter distribution according to  $\omega_{\text{RBM}} = A/d + B$ , where  $A$  ( $\text{cm}^{-1} \text{ nm}$ ) and  $B$  ( $\text{cm}^{-1}$ ) are to be determined experimentally with typical values of  $A$  between 204 and 248 [55, 56]. The *G* band in graphite involves a tangential vibration between the two carbon atoms in the unit cell and exhibits a single peak at 1582  $\text{cm}^{-1}$  [6]. In SWNTs the *G* band is composed mainly of two strong

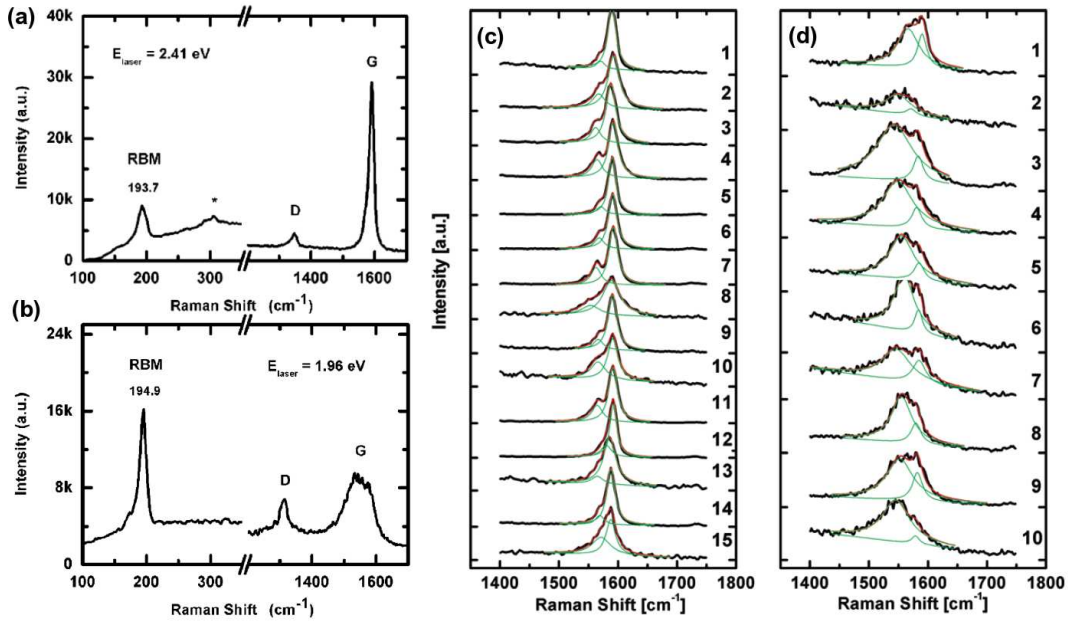


**Figure 2.9:** Resonant Raman spectra of individual semiconducting (a) and metallic (b) carbon nanotubes. The spectra show the radial breathing mode (RBM) and the G band, whose shape depends strongly on the electronic type of the nanotube. This is emphasized in subfigures (c) and (d) by a comparison of the G modes of individual semiconducting and metallic nanotubes, respectively. Modified from Ref. [54].

features,  $G^+$  and  $G^-$ , associated with vibrations along the nanotube axis and along the circumference, respectively. The splitting of the G band peaks as well as their intensity depend on the chirality, but the exact relationship is not yet established [6]. However, there is a strong dependence of the  $G^-$  line shape on the nanotube type, which is often used to distinguish between semiconducting and metallic nanotubes. The appearance of a Breit-Wigner-Fano line shape accompanied by a downshift of the peak frequency is considered as indicator for metallic nanotubes [57, 58].

#### 2.1.4. Fabrication and processing of SWNTs

The method of preparation and any further processing steps are essential for the characteristics of a nanotube sample, i. e. structural properties (chirality, diameter and length) and quality (amount of defects and impurities). Current challenges for the various synthesis methods are on the one hand the development of large-scale and low-cost processes yielding high-quality single-walled carbon nanotubes and on the other hand control over the structural and electronic properties and over the location on a substrate. So far, arc discharge [59], laser ablation [60] and

chemical vapor deposition (CVD [61]) are the most commonly used production methods allowing for bulk synthesis of SWNTs. Recently, ‘supergrowth’ of high-quality vertically aligned SWNTs was achieved through a water assisted CVD method [62]. Processing of the raw material can involve purification, e. g. by acid treatment or centrifugation, debundling using ultra-sonification and stabilization of the individual nanotubes in surfactant solutions [39].

### Pulsed laser vaporization technique

The nanotubes used in this work were produced by the pulsed laser vaporization (PLV) method [63,64]. They were synthesized and processed by Frank Hennrich.

The PLV technique is based on the vaporization of a carbon target by laser irradiation under an inert atmosphere. A schematic of the laser vaporization setup is shown in Figure 2.10. A Nd:YAG laser (1064 nm, 0.5 J/pulse, 30 Hz) irradiates a target placed inside a T-shaped quartz tube, which is situated inside an oven. The target, which is composed of graphite and Ni and Co powder as catalyst (1 atom % each), is mounted on a ceramic rod and can be rotated or axially translated to ensure a uniform consumption at a typical vaporization rate of  $\sim 0.15$  g/h. In the vaporization process the temperature of the oven is  $1150^\circ$  and the inert atmosphere is established by 0.5 bar Ar gas flowing at  $\sim 80$  sccm. The gas flow ensures that the produced SWNT material can be collected on a paper filter in a cold downstream region of the quartz tube.

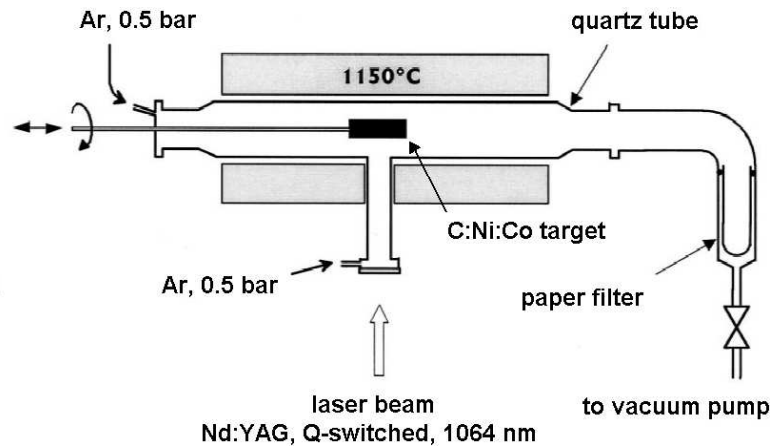


**Figure 2.10:** Schematic of the pulsed laser vaporization setup for the preparation of single-walled carbon nanotubes. A Nd:YAG laser irradiates a target composed of graphite and Ni and Co powder as catalyst and placed inside a T-shaped quartz tube, which is situated inside an oven. The Ar gas flow ensures that the produced SWNT material can be collected on a paper filter in a cold downstream region of the quartz tube. Modified from Ref. [64].

The raw material produced with this method contains bundles of metallic and semiconducting single-walled carbon nanotubes with a narrow diameter distribu-

tion of 1.0–1.5 nm, but also impurities like carbon or catalyst particles. Further processing is required to remove the impurities and debundle the nanotubes.

### Preparing suspensions with individual nanotubes

To prepare stable suspensions of individual SWNTs, the raw material (typically 1 mg) is first dispersed in D<sub>2</sub>O (~ 1 ml) with 1 weight % surfactant using a tip sonicator. Subsequently the suspension is centrifuged (typically 20000 g for about 1 hour) and the supernatant is decanted to remove large agglomerates and non-nanotube impurities. The resulting sample contains individual nanotubes surrounded by adsorbed surfactant molecules (called surfactant micelle in the following) which prevents the re-formation of bundles [39]. Additionally, the surfactant-stabilized SWNTs can be fractionated according to their length by size-exclusion chromatography [65]. The quality of the individualization can be probed by photoluminescence spectroscopy and atomic force microscopy (AFM). The latter allows for statistics on the diameter and length distribution of a sample.

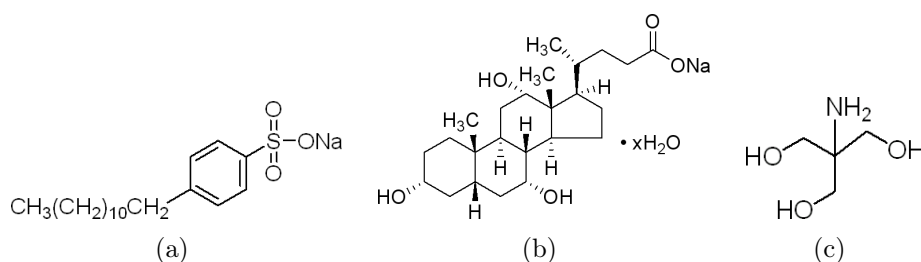


**Figure 2.11:** (a-c) Chemical structures of SDBS (a), sodium cholate (b) and Tris(hydroxymethyl)aminomethane (c). In Tris cholate the Na<sup>+</sup> ion of sodium cholate is substituted by a Tris molecule.

In this work, suspensions with three different surfactants were used for comparative studies: sodium cholate (NaCh), Tris cholate (TrisCh) and sodium dodecylbenzene sulfonate (SDBS). The chemical structure of these molecules is shown in Figure 2.11. While SDBS features an anionic head group and a flexible hydrophobic tail, the bile salts (NaCh and TrisCh) exhibit a molecularly rigid structure with charged face opposing a hydrophobic one, which is expected to interact with the nanotube surface [66]. The results of molecular dynamics simulation [67] which exploits the formation of micelle structures around single-walled carbon nanotubes support this assumption (see Figure 2.12).

An efficient micelle formation around the SWNTs occurs only if the concentration of the surfactant molecules is high enough to enable a spontaneous assembly into groups. This value is called the critical micelle concentration (CMC) and depends on the surfactant type. The micelle itself is a dynamic complex with a continuous exchange of the constituting molecules and the neighboring molecules.

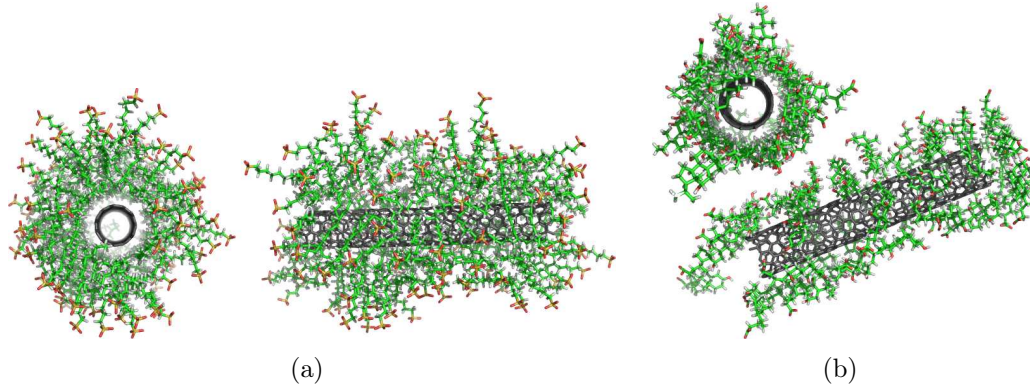


**Figure 2.12:** Formation of surfactant micelles around SWNTs according to molecular dynamics simulations. While SDBS molecules encapsulate the nanotube in a radial arrangement (a), NaCh molecules align with their hydrophobic face pointing towards the nanotube surface (b). The different colors illustrate C atoms of the nanotube (grey) and of the molecules (green), S atoms (yellow), O atoms (red) and H atoms (white). From Ref. [67].

Alternatively to the above presented procedure, suspensions with individual nanotubes can be prepared using density gradient centrifugation [68]. For nanotubes dispersed in NaCh (or other bile salts) this approach allows for a separation by diameter due to differences in the buoyant density. In addition to that, it also provides means to produce highly concentrated suspensions with SWNTs concentrations of the order  $1 \mu\text{g}/\mu\text{l}$ .

### Characterization of the suspension

To characterize the quality of the suspension, in particular the success of the individualization of SWNTs and their diameter range, photoluminescence spectroscopy of the suspension and atomic force microscopy (AFM) of nanotubes spin coated onto silicon wafers were employed [65]. For a qualitative comparison of the content of metallic and semiconducting nanotubes in different suspensions, absorbance spectra of the suspensions were taken with a Varian Cary 500 UV-Vis-NIR spectrophotometer. Figure 2.13 shows a typical absorbance spectrum of single-walled carbon nanotubes produced with the PLV method dispersed in  $\text{D}_2\text{O}$  with 1 weight % NaCh. The absorbance bands can be assigned to certain  $E_{ii}$  transitions: the ‘M1’ band centered around 650 nm corresponds to the  $E_{11}^M$  transition of metallic nanotubes, while the ‘S2’ and ‘S1’ bands—centered around 950 nm and 1670 nm—correspond to the  $E_{22}^S$  and  $E_{11}^S$  transition in semiconducting nanotubes, respectively. The broadness of these bands is indicative for the diameter range of the PLV nanotubes,  $d = 1.0\text{--}1.5 \text{ nm}$ .

Details of the suspensions used in this work are shown in appendix A.

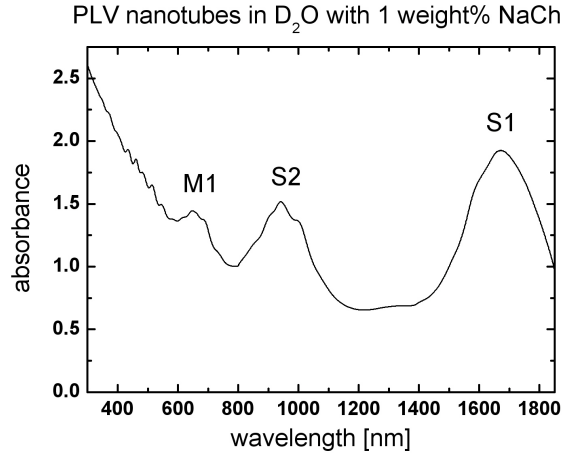


**Figure 2.13:** Typical absorbance spectrum of single-walled carbon nanotubes produced with the PLV method dispersed in  $D_2O$  with 1 weight % NaCh. The ‘M1’ band centered around 650 nm corresponds to the  $E_{11}^M$  transition of metallic nanotubes, while the ‘S2’ and ‘S1’ bands—centered around 950 nm and 1670 nm—correspond to the  $E_{22}^S$  and  $E_{11}^S$  transition in semi-conducting nanotubes, respectively.

## 2.2. Dielectrophoresis (DEP)

The motion of neutral particles under the influence of an inhomogeneous external electric field is called dielectrophoresis (DEP) [13, 69]. Since the dielectrophoretic force is based on induced multipolar moments, it is observed only in nonuniform electric fields with both DC or AC excitation. In contrast, electrophoresis—which is based on the interaction between the net charge of a particle and the external field—occurs also in uniform electric fields. If the polarizability of the particle is larger than that of the surrounding dielectric medium, the dielectrophoretic force points into the region of high field inhomogeneity, else it is repelled. These two types are called positive and negative dielectrophoresis, respectively. The magnitude of the dielectrophoretic force depends also on the particle volume. In recent years, dielectrophoresis has emerged as an important technique to remotely move and manipulate suspended micro- and nano-sized particles [21, 70, 71].

### 2.2.1. Basic theory of dielectrophoresis

A dielectric material (with zero net charge) under the influence of an external electric field experiences a polarization. Due to the movement of bound charges within the material induced multipolar moments are formed.

Considering a particle (index  $p$ ) surrounded by a liquid (index  $\ell$ ), these multipolar moments are in general a function of the size and shape of the particle, the external electric field  $E_{\text{ext}}$  and the dielectric constants  $\varepsilon_p$  and  $\varepsilon_\ell$ . For a lossy par-

particle exposed to an alternating electric field  $\vec{E}_{\text{ext}}(\vec{r}, t) = \Re \left[ \vec{E}_0(\vec{r}) \exp(i\omega t) \right]$ , the multipolar moments also depend on the conductivities  $\sigma_p$  and  $\sigma_\ell$  and the angular field frequency  $\omega$ .

Within the dipole approximation of the effective moment theory higher order terms induced by the electric field are neglected [13]. Except for the case where the particle is located near zero field, this approximation yields accurate results as compared to full Maxwell stress tensor calculations [72]. The particle is assumed to be small compared to the characteristic length scale of the electric field, i. e.  $\nabla \vec{E}$  is constant along the length of the particle. It is also assumed that the presence of the particle does not change the surrounding electric field [69]. The energy of the induced dipole in the electric field and the dielectrophoretic force then follows from  $U = -\frac{1}{2} \vec{p}_{\text{eff}} \cdot \vec{E}_{\text{ext}}$  and  $\vec{F} = -\nabla U$  using the appropriate form of  $\vec{p}_{\text{eff}}$ . In addition to the dielectrophoretic force, particles which exhibit an anisotropy due to either intrinsic—e. g. dielectric—or extrinsic—e. g. structural—properties experience a dielectrophoretic torque given by the expression  $\vec{T} = \vec{p}_{\text{eff}} \times \vec{E}_{\text{ext}}$ .

### Spherical particles

The simplest case is that of a homogeneous spherical particle with radius  $r$ , whose effective dipole moment is given by

$$\vec{p}_{\text{eff}} = 4\pi r^3 \varepsilon_\ell \Re \left( \frac{\varepsilon_p^* - \varepsilon_\ell^*}{2\varepsilon_\ell^* + \varepsilon_p^*} \right) \vec{E}_0 \quad \text{with } \varepsilon_{p,\ell}^* = \varepsilon_{p,\ell} - i \frac{\sigma_{p,\ell}}{\omega}. \quad (2.13)$$

The term  $(\varepsilon_p^* - \varepsilon_\ell^*) / (2\varepsilon_\ell^* + \varepsilon_p^*)$ , which is called Clausius-Mossotti function (*CMF*), provides a measure of the effective polarization of the particle as a function of  $\varepsilon_\ell^*$  and  $\varepsilon_p^*$ . Its precise form depends on the shape of the particle.

With the approximation that the frequency of the electric field is sufficiently high and the particle therefore only responds to time averages [69], the time averaged dielectrophoretic force can be written as

$$\langle \vec{F}_{\text{DEP}} \rangle = \pi r^3 \varepsilon_\ell \Re \left( \frac{\varepsilon_p^* - \varepsilon_\ell^*}{2\varepsilon_\ell^* + \varepsilon_p^*} \right) \text{grad} \left| \vec{E}_0 \right|^2. \quad (2.14)$$

### Ellipsoidal particles

For an ellipsoidal particle the dipole moment depends on the orientation of the particle with respect to the external field.<sup>1</sup> The geometric anisotropy of the particle alters the internal electric field  $E_i^-$  of a particle with semi-major axes  $a, b$  and  $c$

---

<sup>1</sup>Of the non-spherical particles, ellipsoidal particles are the only ones for which the dipole moment is analytically describable.

(w.l.o.g.,  $a > b, c$ ) such that

$$E_i^- = \frac{\varepsilon_\ell}{\varepsilon_\ell^* + (\varepsilon_{p,i}^* - \varepsilon_\ell^*) L_i} E_{0,i} \quad \text{with } i = 1, 2, 3. \quad (2.15)$$

$L_i$  is the depolarization factor in the coordinate system of the ellipsoidal particle, with

$$L_1 = \frac{abc}{2} \int_0^\infty \frac{ds}{(s+a^2)R_s}, \quad (2.16)$$

where  $R_s = \sqrt{(s+a^2)(s+b^2)(s+c^2)}$ .  $L_2$  and  $L_3$  are defined by expressions similar to Equation (2.16), in which the term  $(s+a^2)$  is then substituted by  $(s+b^2)$  and  $(s+c^2)$ , respectively. It follows that  $0 \leq L_i \leq 1$  and  $L_1 + L_2 + L_3 = 1$ .<sup>2</sup>

From this the effective moment in the particle's coordinate system can be derived as follows

$$\vec{p}_{\text{eff}} = \begin{pmatrix} \alpha_{11} & 0 & 0 \\ 0 & \alpha_{22} & 0 \\ 0 & 0 & \alpha_{33} \end{pmatrix} \begin{pmatrix} E_{0,1} \\ E_{0,2} \\ E_{0,3} \end{pmatrix} \quad (2.17)$$

$$\text{with } \alpha_{ii} = \frac{4\pi abc}{3} \varepsilon_\ell \Re \left( \frac{\varepsilon_{p,i}^* - \varepsilon_\ell^*}{\varepsilon_\ell^* + (\varepsilon_{p,i}^* - \varepsilon_\ell^*) L_i} \right) \quad (2.18)$$

The time averaged dielectrophoretic torque is given by the expression

$$\langle T_{\text{DEP}} \rangle_\alpha = \frac{1}{2} \Re \left[ (p_{\text{eff}})_\beta E_{0,\gamma} - (p_{\text{eff}})_\gamma E_{0,\beta} \right] \quad (2.19)$$

with  $\alpha, \beta, \gamma = 1, 2, 3$  in the particle's coordinate system. With Equations (2.17) and (2.18) it follows for ellipsoidal particles

$$\langle T_{\text{DEP}} \rangle_\alpha = \frac{1}{2} E_{0,\beta} E_{0,\gamma} \frac{4\pi abc}{3} \varepsilon_\ell \Re \left[ \frac{\varepsilon_{p,\beta}^* - \varepsilon_\ell^*}{\varepsilon_\ell^* + (\varepsilon_{p,\beta}^* - \varepsilon_\ell^*) L_\beta} - \frac{\varepsilon_{p,\gamma}^* - \varepsilon_\ell^*}{\varepsilon_\ell^* + (\varepsilon_{p,\gamma}^* - \varepsilon_\ell^*) L_\gamma} \right]. \quad (2.20)$$

While the dielectrophoretic torque can be specified within the particle's coordinate system, the dielectrophoretic force is generally defined in the global coordinate system. For this a coordinate transformation from the particle's to the global system is necessary:

$$\tilde{\vec{p}}_{\text{eff}} = R^T \vec{p}_{\text{eff}} R \quad \text{with rotation matrix } R. \quad (2.21)$$

Obviously, the expression for the dielectrophoretic force acting on an ellipsoidal particle is much more complicated than in the case of a spherical particle. However, assuming a rod-shaped particle with  $a \gg b = c$  to be aligned with its

---

<sup>2</sup>Note that the use of  $\varepsilon_{p,i}^*$  in Equation (2.15) also allows for an anisotropy in the dielectric properties of the particle.

long axis parallel to and positioned on the axis of an axially symmetric field, the dielectrophoretic force resembles that for a sphere:

$$\langle \vec{F}_{\text{DEP}} \rangle = \frac{\pi ab^2}{3} \varepsilon_\ell \Re \left[ \frac{\varepsilon_{\text{p},\parallel}^* - \varepsilon_\ell^*}{\varepsilon_\ell^* + (\varepsilon_{\text{p},\parallel}^* - \varepsilon_\ell) L_\parallel} \right] \frac{\partial E_{0,z}^2}{\partial^2 z} \hat{z}. \quad (2.22)$$

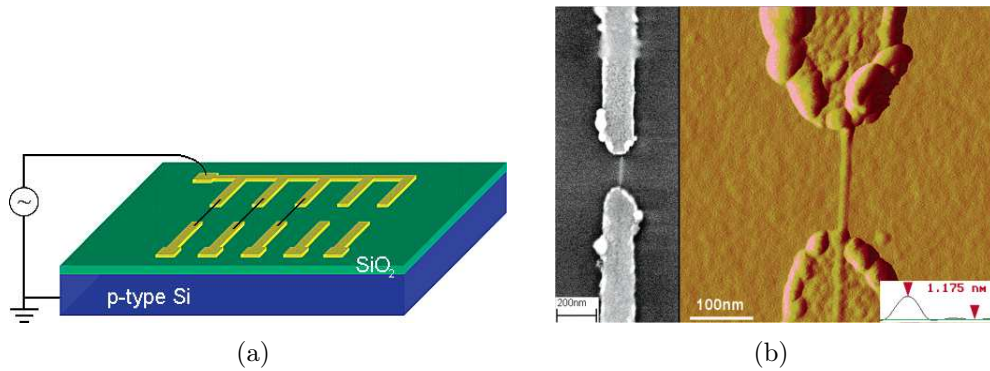
From this, Equation (2.14) for the special case of a spherical particle can be easily reproduced with  $a = b = c = r$  and  $L_i = 1/3$ .

### 2.2.2. Dielectrophoresis of single-walled carbon nanotubes

In the field of carbon nanotube research, dielectrophoresis was first introduced as a tool to assemble and contact individual or bundled single-walled carbon nanotubes on predefined electrode structures [12, 22]. It was then demonstrated that dielectrophoresis allows for a electronic type specific sorting of SWNTs due to the difference in polarizability of semiconducting and metallic nanotubes [11].

#### Assembly by dielectrophoresis

Single-walled carbon nanotubes are considered to hold great promise as building blocks in future nanoscale electronics such as field effect transistors or interconnects due to their nanoscale dimensions and outstanding electronic properties like ballistic transport and insensitivity to electromigration [73–75]. The controlled assembly and contacting of the nanotubes is a prerequisite for an effective device fabrication.



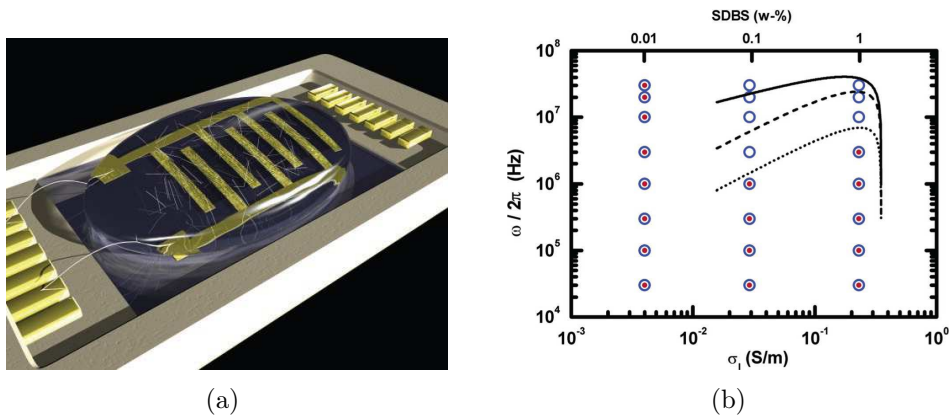
**Figure 2.14:** Single-walled carbon nanotube assembly by dielectrophoresis. (a) Schematic drawing of the layout for SWNT assembly. (b) SEM and AFM image of one individual SWNT deposited by dielectrophoresis. Modified from Ref. [12].

Figure 2.14(a) shows a schematic layout of an electrode structure that allows for the precise deposition of individual single-walled carbon nanotubes onto multiple

submicrometer electrode pairs by dielectrophoresis [12]. The device consists of Ag electrodes on a p-type silicon substrate with a thin layer of thermally oxidized  $\text{SiO}_2$ . A unique feature of the setup is the fact that the AC signal is applied only to one driven electrode, while the other electrode is capacitively coupled with the grounded Si substrate, which allows to upscale the process to high-density arrays. In addition, the deposition process exhibits a self-limiting behavior resulting in the assembly of merely one or few individual nanotubes per contact. Both topics will be discussed in greater detail in Section 4.2. An example of an individual nanotube deposited onto Ag electrodes is shown in Figure 2.14(b).

### Separation of metallic and semiconducting nanotubes

An analysis of the metallicity of the nanotubes deposited between electrode pairs by dielectrophoresis at a frequency  $f = 1$  MHz reveals a selectivity of the process towards metallic nanotubes, suggesting that AC dielectrophoresis might allow for an electronic type specific separation at high field frequencies [12]. This was verified in Reference [11].



**Figure 2.15:** Electronic type specific separation of SWNTs. (a) Illustration of the experimental setup showing metallic SWNTs (depicted as black rods) deposited between interdigitated electrodes, while the semiconducting nanotubes (depicted as white rods) remain in suspension. (b) Dielectrophoretic deposition of semiconducting and metallic SWNTs versus electric field frequency  $\omega$  and conductivity  $\sigma_\ell$  of the suspension. Deposition of metallic and semiconducting nanotubes is marked by blue open circles and red filled circles, respectively. Taken from Ref. [11] and [25].

The inhomogeneous electric field in this experiment was generated by interdigitated Au electrodes. In this setup the dielectrophoretic deposition is not limited to individual nanotube contacts—instead a large number of nanotubes is deposited between the electrodes. By applying a high-frequency AC voltage to the pair of interdigitated electrodes, the metallic nanotubes are attracted to and deposited

between the electrodes, while the semiconducting nanotubes remain in the suspension, as illustrated in Figure 2.15(a). To verify the separation and prove its efficiency, resonant Raman spectra of the samples after deposition are recorded. A comparison with the Raman spectra of a reference sample shows that  $(80 \pm 5)$  % of the deposited nanotubes are indeed metallic.

The dielectrophoretic deposition turns out to strongly depend on the experimental conditions, in particular the electric field frequency  $f = \omega/2\pi$  and the conductivity  $\sigma_\ell$  of the suspension, which is determined by the type and concentration of the surfactant [25]. The result of a systematic study of this dependence for SWNTs dispersed in SDBS is presented in Figure 2.15(b), revealing a cross-over from positive to negative dielectrophoresis for semiconducting nanotubes at a critical frequency  $f_c$ , which depends on the surfactant.

The above findings were explained using a generalized form of Equation (2.22)

$$\langle \vec{F}_{\text{DEP}} \rangle = \frac{\pi d^2 l}{8} \varepsilon_\ell \Re \left[ \frac{\varepsilon_p^* - \varepsilon_\ell^*}{\varepsilon_\ell^* + (\varepsilon_p^* - \varepsilon_\ell) L_{\parallel}} \right] \nabla E^2, \quad (2.23)$$

i. e. considering the nanotubes as rod-like particles. The depolarization factor  $L_{\parallel}$  is of the order of  $10^{-5}$  for the nanotubes used in the experiment. The high- and low-frequency limit of the Clausius-Mossotti function ( $CMF$ ) is then given by

$$\lim_{\omega \rightarrow \infty} CMF = \frac{\varepsilon_p - \varepsilon_\ell}{\varepsilon_\ell} \quad \text{and} \quad (2.24)$$

$$\lim_{\omega \rightarrow 0} CMF = \frac{\sigma_p - \sigma_\ell}{\sigma_\ell}. \quad (2.25)$$

In the case of metallic nanotubes, both dielectric constant and conductivity are higher than those of the liquid and the nanotubes therefore experience a positive dielectrophoresis irrespective of the field frequency. The observed cross-over for semiconducting nanotubes on the other hand implies that the conductivity is higher and the dielectric constant is lower than for the aqueous suspension. While the latter agrees with the theoretically predicted low dielectric constant (Section 2.1.2), the positive dielectrophoresis for low frequencies obviously contradicts the zero intrinsic conductivity of semiconducting nanotubes. To solve this contradiction, a finite surface conductivity was suggested to exist in the semiconducting SWNTs caused by the diffusive ions of the surfactant molecules [25].

As explained in Section 2.1.3, resonant Raman spectroscopy depends on the resonance condition, i. e. for a specific excitation wavelength only those nanotubes contribute to the signal whose transition energy equals the excitation energy. Optical absorbance spectroscopy on the other hand measures any nanotubes present in a sample and thus provides a fast and reliable tool to compare the composition of different samples. However, while the Raman features of carbon nanotubes are easily distinguishable from additional (background) features caused for example by the silicon substrate, the differentiation between sample and background

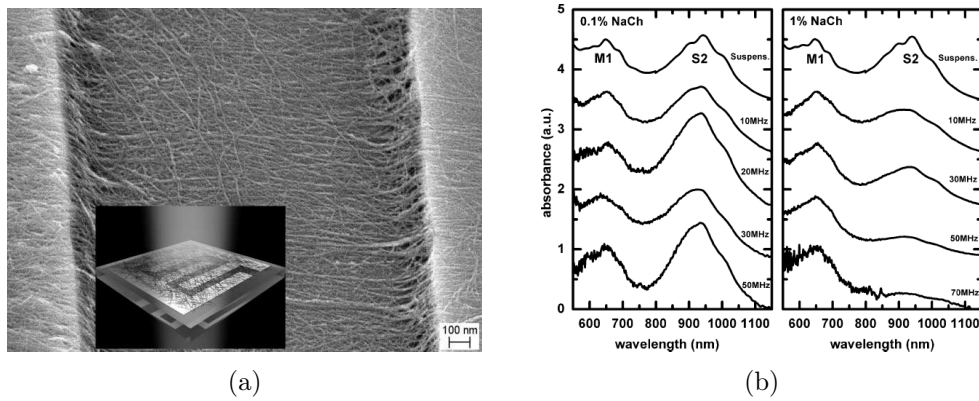


**Figure 2.16:** Thin films of single-walled carbon nanotubes and their optical absorbance spectra. (a) SEM image showing a thin film of SWNTs deposited by DEP onto an array of interdigitated electrodes. The inset illustrates the absorbance measurement in transmission. (b) Absorbance spectra of thin films of SWNTs deposited with AC-frequencies as specified in the graphs. Taken from Ref. [26].

contribution is more difficult in the case of optical absorption spectroscopy. Consequentially, a higher amount of nanotubes is required for a good signal-to-noise ratio in the case of optical absorption as compared to Raman spectroscopy.

By using Al electrodes on quartz glass substrate and a higher AC voltage, the yield of the dielectrophoretic deposition can be increased sufficiently to observe absorbance spectra with a good signal-to-noise ratio [26]. Figure 2.16(a) shows an SEM image of a thin film of metallic carbon nanotubes and a schematic of the experimental setup to acquire the absorption spectra measured with a Fourier-transform infrared (FTIR) spectrometer in transmission mode. The resulting spectra for different concentrations of NaCh are presented in Figure 2.16(b). The decrease in the S2 band for SWNTs dispersed with 1 weight % NaCh with increasing field frequency clearly confirms the preferential deposition of metallic nanotubes under these conditions. The situation changes drastically for 0.1 weight % NaCh, in which case no preferential deposition whatsoever is observed, because this concentration falls below the critical micelle concentration for NaCh. These results demonstrate that a high degree of individualization of the suspended nanotubes is essential for the success of the dielectrophoretic separation.

## 2.3. Finite element simulations

For the assembly and separation of SWNTs a number of different experimental setups/electrical devices are used, each providing a characteristic external electric field. To optimize the dielectric force fields for a specific application and to better understand the experimental observations it is necessary to model and visualize

the electric fields. This is achieved by the use of finite element simulations.

### 2.3.1. Principles of finite element simulation

The finite element method (FEM) is a numerical technique used to find approximate, but numerically stable solutions for partial differential equations (PDEs) or integral equations. In the next section the basic principle of FEM will be sketched similar to Reference [76].

#### Weak formulation

Assuming a PDE of the following form

$$\begin{cases} -\Delta u = f \\ u|_{\Gamma_1} = \gamma & \text{Dirichlet boundary} \\ \frac{\partial u}{\partial n}|_{\Gamma_2} = 0 & \text{Neumann boundary,} \end{cases} \quad (2.26)$$

where  $u \equiv u(x, y, z)$  (similarly  $f \equiv f(x, y, z)$  etc.) and  $\Delta u$  exists within a domain  $\Omega$  with boundaries  $\partial\Omega = \Gamma_1 \cup \Gamma_2$ .

In a first step such a PDE is rephrased into the corresponding variational formulation (also called weak formulation). When deriving the weak form one generally aims to minimize the highest order of derivatives that occur in the integrals. The weak form of the above PDE (2.26) is given by

$$\begin{cases} \text{Find } u \text{ smooth, such that } u|_{\Gamma_1} = \gamma \text{ and} \\ \int_{\Omega} \nabla u \cdot \nabla v \, dA = \int_{\Omega} f v \, dA \text{ for all smooth } v|_{\Gamma_1} = 0. \end{cases} \quad (2.27)$$

The smooth function  $v$  is referred to as test function.

#### Discretization

The second step is the discretization of the weak form. The domain  $\Omega$  is divided into subdomains  $\Omega_i$  with  $i \in \{1, \dots, n\}$ , which are called ‘finite elements’ (see Figure 2.17). Within each of these subdomains Equation (2.27) holds true, but the integration now runs over  $\Omega_i$  which is of much smaller dimension than  $\Omega$ . To complete the discretization  $u$  is now written as a sum of basis functions  $\varphi_i$  in  $\Omega_i$  which satisfy

$$\varphi_i|_{\Gamma_1} = 0. \quad (2.28)$$

These functions might be polynomials or trigonometric functions, depending on the context. Note that the choice of the basis functions strongly influences the

accuracy and speed of the solution. Then

$$\tilde{u} = \sum_{i=1}^n c_i \varphi_i \rightarrow u \quad \text{as } n \rightarrow \infty, \quad (2.29)$$

where  $\tilde{u}$  is the approximate solution.

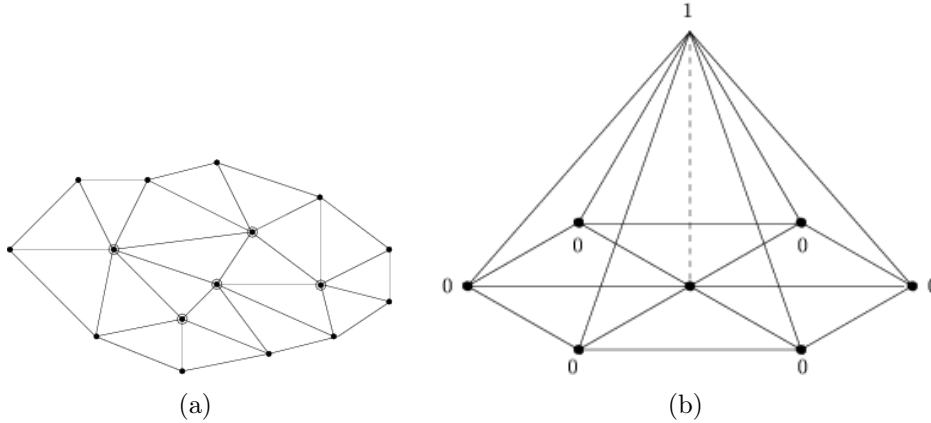


**Figure 2.17:** finite element discretization in 2d: (a) a triangular subdivision of the domain  $\Omega$ ; (b) a typical basis function  $\varphi_i$ . From Ref. [77].

Assuming that the test functions  $v|_{\Gamma_1} = 0$  are represented by the set of  $\varphi_i$ , the finite element representation of the weak form (2.27) is:

$$\left\{ \begin{array}{l} \text{Find the set of constants } \{c_1, \dots, c_n\}, \text{ such that} \\ \sum_{j=1}^n \int_{\Gamma} c_j \nabla \varphi_j \cdot \nabla \varphi_i \, dA = \int_{\Gamma} f \varphi_i \, dA \quad \text{for all } i \in \{1, \dots, n\}. \end{array} \right. \quad (2.30)$$

For an efficient solution, the discretization matrix  $A$  with

$$A_{ij} = \int_{\Gamma} \nabla \varphi_i \cdot \nabla \varphi_j \, dA \quad (2.31)$$

should contain as many zeros as possible. The ideal choice of  $\{\varphi_i\}$  for this would be a set of orthogonal functions; since this is often not possible in practice,  $\{\varphi_i\}$  are chosen such that

$$A_{ij} \begin{cases} \neq 0 & \text{for } j = i - 1, i, i + 1 \\ = 0 & \text{else.} \end{cases} \quad (2.32)$$

Equation (2.30) implies a set of linear equations of  $\{\varphi_i\}$ . With the definition of the vectors  $x = (c_1, c_2, \dots, c_n)^T$  and  $b = (b_1, b_2, \dots, b_n)^T$ , where  $b_i = \int_{\Gamma} f \varphi_i \, dA$ , this set of linear equation can be written as  $Ax = b$ .

### The solution process

Finding a solution for the original PDE (2.26) now implies solving the set of linear equations represented by  $Ax = b$ . A commonly used approach for systems with a high number of variables is the use of an iterative method. While the direct approach would be to calculate the inverse of the matrix  $A$  (which would be very expensive in terms of computing power or even impossible), an iterative solution process attempts to solve a problem by finding successive approximations to the solution starting from an initial guess.

A limited number of problems can be solved by stationary iterative methods, e. g. the Jacobi method. Starting with an initial guess  $x_0$  this method solves the equation  $Dx^{k+1} = b + (D - A)x^k$ ,  $k \in \{0, 1, 2, \dots\}$ . It can be shown that this algorithm only converges if the matrix  $A$  is strictly diagonally dominant, meaning that for each row the absolute value of the diagonal term is greater than the sum of absolute values of other terms.

The so called Krylov subspace class represents a class of completely different methods to iteratively solve a system of linear equations. While the mathematical theory is very complicated, a common feature of these methods is that the algorithm involves only matrix-vector multiplications, which is very efficient if the matrix contains many zeros, and then proceeds with the resulting vectors. These methods are fast converging and also suitable for large systems.

### Improving the accuracy of the simulation

To improve the accuracy of a finite element simulation, i. e. diminish the error in the approximative solution, there are mainly two options. One consists in reducing the sizes of the subdomains especially in regions with high residual errors, the other option is to redefine the basis function, e. g. increase the degree of polynomials. Both methods obviously result in more complex systems, resulting in longer computation times.

#### 2.3.2. The FlexPDE package

For the simulations shown in this work the software package FlexPDE 5 was used, a commercial finite element solver for partial differential equations [78].

#### Solution process

FlexPDE can solve systems of PDE of first or second order in various coordinate systems (cartesian or cylindrical coordinates). In a first step the software reduces second order terms through integration by parts (weak form). A mesh generation module then divides the problem domain—in two dimensions this mesh consist

of unstructured triangular cells, while in three dimensions the mesh is formed by unstructured tetrahedrons. (Cells in contact with a curved boundary have cell sides which are slightly curved.) The numerical analysis module selects a solution scheme appropriate to the given problem and defines quadratic or cubic basis functions. During the iterative solution process the mesh is redefined in regions where the approximate solution has a large residual error. When the user defined accuracy is achieved, the solution or any algebraic function of the solution can be plotted. (For a more detailed discussion, see Reference [79].)

### Basic usage of FlexPDE

Any simulation done with FlexPDE is based on a script written by the user which defines the physical situation to be modeled. In this script a number of control parameters are specified (e. g. the coordinate system or the accuracy), the dependent variable is named and the PDE to be solved is stated. The geometry of the domain and the relevant boundary conditions are described by walking the perimeter of the domain. If the domain consists of regions with differing material parameters, these regions are defined successively. Here, in case of overlap, later defined regions will overwrite regions defined before.

### Some comments

In general, the automatic mesh generation by FlexPDE works rather well. In some cases it might be advisable to manually define a certain mesh density in regions where the solution is expected to vary significantly. This can speed up the solution process.

While a problem domain in a two-dimensional simulation can be arbitrarily complex, the definition of three-dimensional structures in FlexPDE is more restricted. After dividing the vertical range into several layers, predefined two-dimensional structures are extruded in specific layers and thereby a three-dimensional domain is constructed. Thus, extrusion of a two-dimensional circle results in a cylinder with a vertical axis, as depicted in Figure 2.18. Layer interfaces as well as extrusion sidewalls may be non-planar but must not intersect.

One disadvantage of this software package is its inability to compute path or surface integrals of the solution along arbitrary lines and surfaces. Instead, only integrals along boundaries are accessible. Another drawback is the fact that—except for a few exceptions, see e. g. Figure 6.1—it is generally not possible to plot a map of field lines for a given electrostatic problem. Therefore in this work combined maps of the electrostatic potential (illustrated in a color plot) and the electric field (represented by vectors) are shown, as in Figure 4.12. Unlike in the case of field lines, the vector density in these plots does not correspond to the field strength.

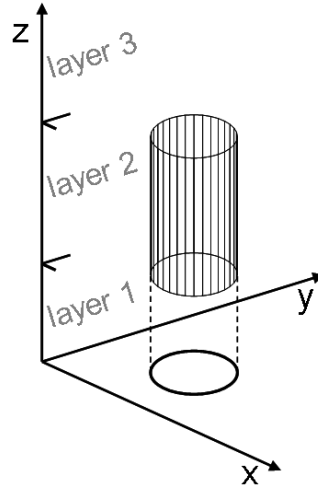


**Figure 2.18:** Creating a three-dimensional domain in FlexPDE: The  $z$  range is divided into three layers and a circle is defined in the  $x$ - $y$  plane. By extrusion of the circle in layer 2, a cylinder is generated within this layer.

### 2.3.3. Choice of the partial differential equation and appropriate boundary conditions

The electrical potential of an oscillating field of frequency  $\omega$  can be expressed by a potential  $\Phi(\vec{x}, t) = \Re[\tilde{\Phi}(\vec{x}) e^{i\omega t}]$  where  $\tilde{\Phi} = \Phi_R + i\Phi_I$  is the potential phasor. The electric field is then given by  $\vec{E}(\vec{x}, t) = \Re[\vec{E}(\vec{x}) e^{i\omega t}]$  with  $\vec{E} = -\nabla\tilde{\Phi}$ .

Considering the electromagnetic material properties, the system dimensions and the frequency used in a typical SWNT dielectrophoresis experiment, magnetic effects can be safely ignored. It is therefore appropriate to work with the Maxwell equations in the quasi-electrostatic limit [80], where the potential is given by [81]

$$\nabla[(\sigma + i\epsilon\omega) \nabla\tilde{\Phi}] = 0. \quad (2.33)$$

Unlike in traveling wave dielectrophoresis, where the phase shift between the potential applied to neighboring electrodes is  $90^\circ$ , the phase shift between two electrode tips (see e. g. section 4.2) or in an interdigitated electrode setup (see section 4.3) is  $180^\circ$ , i. e. the potential phasor is entirely real, such that  $\Phi \equiv \Phi_R$ .

To find an unique solution to Equation (2.33) boundary conditions have to be specified. To any metallic surface connected to a voltage source the Dirichlet boundary condition  $\Phi = \Phi_0$  is applied. Thereby the potential within the metal volume is fixed and no electric field exists inside. As a consequence, depending on the geometry to simulate, it sometimes suffices to define the metallic surface and exclude the metal volume from the simulation. To non-metallic surfaces the Neumann condition  $\partial\Phi/\partial n = \text{constant}$  can be employed, resulting in a continuous normal component of the dielectric displacement  $\vec{D}$ . In the absence of free surface

charges,  $constant = 0$ . Apart from internal boundaries of non-metallic materials, this equation is also applied to external boundaries representing symmetry planes or very distant boundaries.

A double layer between the metallic electrodes and the bulk electrolyte can be modeled by a capacitor between the electrode surface and the bulk resulting in a mixed boundary condition  $\Phi - \frac{\sigma}{i\omega C} \frac{\partial \Phi}{\partial n} = \Phi_0$  [80]. If the experimental frequency is above the ionic charge relaxation frequency  $(\tau_q)^{-1} = \sigma/\varepsilon = 2\pi f_q$ , the formation of double layers at the electrode surfaces can be ignored. For frequencies  $f < f_q$ , the influence of a double layer can be probed experimentally by impedance spectroscopy of the sample within the critical frequency range (see Section 3.1). According to the measurements, the double layer can be neglected at the operational frequency for any system studied in this work.

Under these conditions the problem is well described within the electrostatic limit where the potential is determined by the Laplace equation

$$\nabla (\varepsilon \nabla \Phi) = 0 \quad (2.34)$$

and with the potential at the electrodes equal to the applied voltage  $\Phi_0$ .

The main purpose of the simulations presented in this work is to visualize dielectric forces acting on SWNTs in aqueous solution due to electronic potentials being applied to electrodes of a specific geometry. Nevertheless the explicit physical presence of the nanotubes is ignored in most calculations (see sections 4.1 and 4.3). Unless in a few cases this is a valid approximation—although the dielectric constant of the SWNT can differ strongly from the dielectric constant of the surrounding media, its extremely small size compared to the typical dimensions of the electrodes causes the distortion of the field in the vicinity of the nanotube to be negligible. Therefore the nanotube can be omitted from the simulation, thus reducing the computation time dramatically.

This argument no longer holds true if a nanotube connects a pair of electrodes one of which is at a fixed potential while the other is electrically floating. Such a situation is discussed in sections 4.2 and 4.4.



## 3. Absorption spectra of thin films of single-walled carbon nanotubes

The dielectrophoretic deposition of single-walled carbon nanotubes onto interdigitated electrode structures (IDEs) enables the production of thin film of carbon nanotubes, whose composition can be probed with optical absorption spectroscopy (see Section 2.2.2). In the following study the yield and separation efficiency of this process is examined under variation of characteristic parameters, e. g. the type of surfactant, the conductivity of the suspension and the nanotube concentration. It turns out that due to the very large electric fields used in this survey, the cross-over frequencies for semiconducting nanotubes reported before no longer hold true. Instead both electronic types of nanotubes are deposited on the electrode array, but they exhibit a severe difference in their alignment with respect to the electric fields during deposition. These effects can be explained using an advanced model of nanotube dielectrophoresis, which incorporates for the first time both the longitudinal and transversal polarizability.

### 3.1. Experimental

#### 3.1.1. Dielectrophoretic deposition of single-walled carbon nanotubes onto interdigitated electrodes

The experiments are conducted using a procedure similar to that described in Reference [26]. The interdigitated electrode structure, which was provided by Dr. Rapp from the Institut für Mikrostrukturtechnik at the Forschungszentrum Karlsruhe, is illustrated in Figure 3.1. The electrodes are made of either 145 nm thick pure aluminum or 54 nm thick gold, structured on a 500  $\mu\text{m}$  quartz glass substrate by optical lithography. The width of the electrode fingers as well as the gap between them is 1.8  $\mu\text{m}$ . Each sample contains two active areas—in the following called *A* and *B*—of approximately 0.15 mm<sup>2</sup> size, which can be individually connected to an AC voltage source. For this purpose, the sample is mounted on a ceramic package/chip carrier and the bonding pads are connected by wire-bonding to the leads (see also Figure 2.15(a)). To apply a continuous AC voltage

an Agilent 33250A Function/Arbitrary Waveform Generator is used, whose signal is amplified with a Empower RF Systems High Power RF Amplifier.

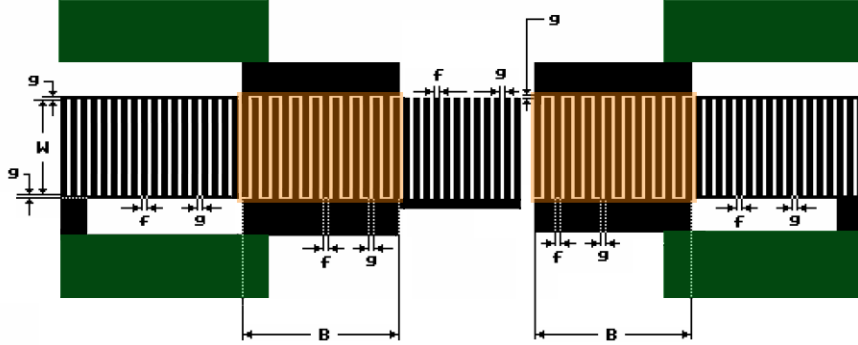


**Figure 3.1:** Schematic of the interdigitated electrode structure. On each sample there are two active areas (marked in orange), which can be individually connected via the bonding pads (green). The width of the fingers and the gaps are  $f = g = 1.8 \mu\text{m}$ , the size of the active area is  $W \cdot B \approx 0.15 \text{ mm}^2$ .

After placing a droplet of  $15 \mu\text{l}$  of nanotube suspension onto the electrode array, an AC signal is applied to the sample. During the duration of the experiment, the active area of the sample is observed through a light microscope to monitor the formation of the nanotube film. After switching off the AC voltage, the sample is rinsed with  $\text{H}_2\text{O}$  and gently dried off with nitrogen gas.

In Reference [26] a peak-to-peak voltage of  $V_{\text{pp}} = 20 \text{ V}$  was applied for  $t = 5 \text{ min}$ . In this work the peak-to-peak voltage was increased to  $V_{\text{pp}} = 40 \text{ V}$ <sup>1</sup> corresponding to an electric field  $E_{\text{pp}}$  of the order of  $2 \cdot 10^7 \text{ V/m}$ . For high solution conductivity such large fields cause electrothermally induced motion of the liquid obstructing dielectrophoresis [80], which is observable under a light microscope. It was found that electrothermal motion can be efficiently suppressed by using AC-voltage bursts of duration  $t_{\text{ON}} = 10 \text{ ms}$  and period  $\tau = 80 \text{ ms}$  instead of a continuous signal. The total deposition time  $t = 10 \text{ min}$  was chosen such that  $V_{\text{pp}}^2 \cdot t_{\text{eff}}$  with  $t_{\text{eff}} = t \cdot t_{\text{ON}}/\tau$  is equal to  $(20 \text{ V})^2 \cdot (5 \text{ min})$  as in Reference [26].<sup>2</sup> To generate the pulsed AC signal, a second Waveform Generator is employed as external trigger.

<sup>1</sup>Unless stated otherwise, this peak-to-peak voltage was used for the preparation of all samples presented in the following.

<sup>2</sup>With  $F_{\text{DEP}} \propto E_{\text{pp}}^2$  and  $p = \int F dt$ ,  $V_{\text{pp}}^2 \cdot t_{\text{eff}}$  is a measure for the momentum of the nanotubes under dielectrophoresis.

Typical characterization of the samples include

- impedance spectroscopy before and after the deposition to qualify the electrical contact between the nanotubes and the electrodes (see Figure 3.3) and
- observation of the sample during the dielectrophoretic deposition with a light microscope to monitor the formation of the nanotube film and to detect electrothermally induced motion of the liquid.

After the sample has been rinsed and dried, further characterization involves:

- incident light dark field microscopy and scanning electron microscopy (SEM) to determine the homogeneity of the deposited nanotube film (see Figure 3.6(a)),
- atomic force microscopy (AFM) to measure the thickness of the nanotube film (see Figure 3.6(b)),
- optical absorption spectroscopy (see Figure 3.8) and
- resonant Raman spectroscopy to specify the composition of the film and thereby the degree of separation (see Figures B.8 and B.9).

In this work the characteristic dielectrophoresis parameters were varied in independent series of experiments. First, the dielectrophoretic deposition experiment was conducted at a fixed frequency of  $f = 10$  MHz using single-walled carbon nanotubes produced with the PLV method and dispersed in different surfactants: Suspension #24.2 and 24.4, which contain long nanotubes ( $\sim 1000$  nm) in  $D_2O$  with 1 weight % NaCh, Suspension #26.3 containing long nanotubes dispersed in  $D_2O$  with 1 weight % TrisCh and finally Suspension #23.12, which contains short nanotubes ( $\sim 300$  nm) dispersed in  $D_2O$  with 1 weight % SDBS (see Appendix A). Next, the electric field frequency was varied between  $f = 300$  kHz and  $f = 80$  MHz using Suspension #26.3. Finally, at a fixed frequency of  $f = 80$  MHz the concentration of Suspension #24.4 was varied by diluting the original suspension with pure surfactant solution. The results and interpretations presented in Section 3.2 were obtained by taking the experimental observations of any of these series into account.

### 3.1.2. Morphology of the samples

In earlier experiments, gold was used as material for the interdigitated electrodes [11]. However comparing the amount of nanotubes deposited by dielectrophoresis under equal experimental conditions on both Au and Al electrodes it turns out that a much higher yield is reached using Al electrodes.

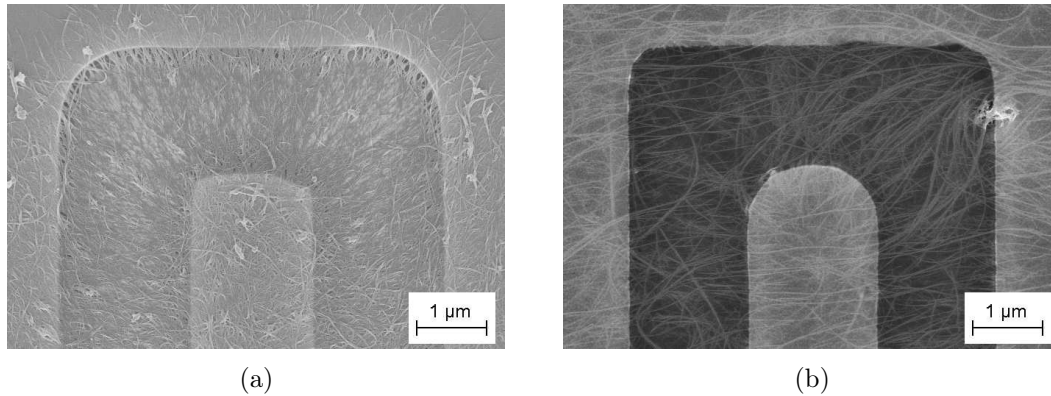


**Figure 3.2:** Morphology of nanotubes deposited on Al and Au electrodes under similar experimental conditions. In the case of Al electrodes (a), the nanotubes form a dense and continuous network and contrast changes in the SEM image are mainly due to differences in the local morphology. On the other hand, only few nanotubes are deposited onto the Au electrodes (b) and the material properties of quartz glass (dark), gold (semi-bright) and carbon nanotubes (bright) cause strong differences in the local contrast.

Figure 3.2 shows SEM images of nanotubes deposited under similar conditions on Al and Au electrodes. In the case of the Al electrodes (Figure 3.2(a)) a continuous film of nanotubes covers both the electrodes and the gap between them (see also Figure 3.6(a)). The small contrast observable in the SEM image is mainly due to local variations in the morphology. The image of nanotubes deposited on Au electrodes (Figure 3.2(b)) on the other hand shows strong differences in contrast which arise from the material properties of nanotubes (bright), gold (semi-bright) and quartz glass (dark). Obviously, in this case, the amount of nanotubes on the electrode array is significantly smaller compared to the Al electrodes and the nanotubes do not form a compact network.

The enhanced yield of deposited nanotubes when using Al electrodes is attributed to the natural oxide layer which covers the surface of the Al electrodes and degrades the electric contact between the electrode fingers and the nanotubes deposited between them. Another consequence of the oxide layer is the observation that heat dissipation in the evolving nanotube film is greatly suppressed when using Al electrodes as compared with Au electrodes.

### 3.1.3. Impedance spectroscopy of the electrode arrays

Impedance spectra in the frequency range  $f = 50\text{--}10^6$  Hz were measured routinely before and after the dielectrophoretic deposition for all samples with an Agilent 4284A Precision LCR Meter. In addition, a few samples were probed with an Agilent 8712C RF Network Analyzer in the frequency range  $f = 3 \cdot 10^5\text{--}1.3 \cdot 10^9$  Hz.

### Gold and aluminum electrodes

Impedance spectroscopy on interdigitated electrodes after deposition of single-walled carbon nanotubes allows to test the quality of the electronic contact between the nanotubes and the electrodes. A comparison between Al and Au electrodes should reveal a fundamental difference in the electronic contact due to the natural oxide layer covering the Al electrodes.

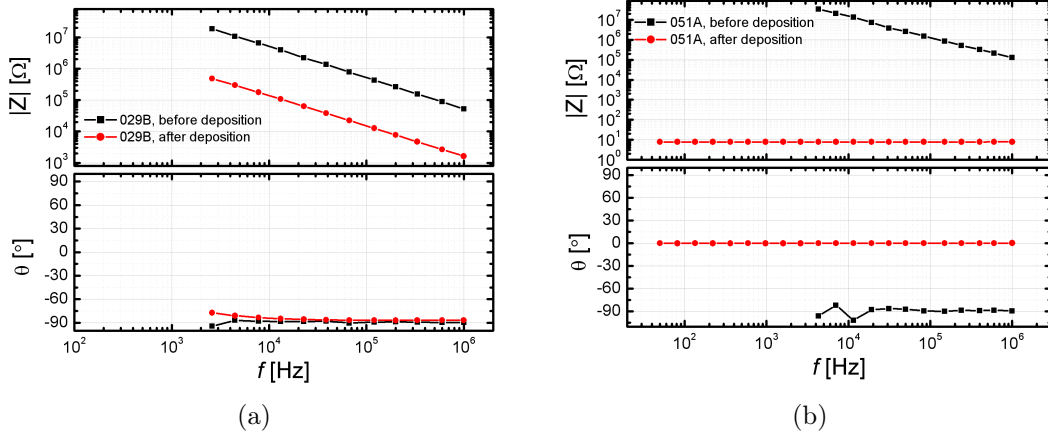


**Figure 3.3:** Impedance spectra of interdigitated electrode structures. Plotted are the absolute value of the impedance  $|Z|$  and the phase  $\Theta$  versus frequency for Al (a) and Au electrodes (b). The Al sample shows a purely capacitive behavior before and after dielectrophoretic deposition. The Au sample becomes purely ohmic after the deposition of nanotubes.

Figure 3.3 shows a comparison between the impedance spectra measured for Al and Au electrodes before and after deposition of nanotubes dispersed in TrisCh (suspension # 26.3).<sup>3</sup> Before the deposition both structures show a purely capacitive behavior ( $\Theta \approx -90^\circ$ ) with  $C_{\text{Al-IDE}} = 3.26 \text{ pF}$  and  $C_{\text{Au-IDE}} = 0.824 \text{ pF}$ . These numbers are within the typical range determined by measurements on other structures.

After a dielectrophoretic deposition using the standard parameters of  $t = 10 \text{ min}$ ,  $t_{\text{ON}} = 10 \text{ ms}$  and  $\tau = 80 \text{ ms}$  with a deposition frequency  $f = 10 \text{ MHz}$ , the Al structure is still purely capacitive, but the capacitance is higher by up to two orders of magnitude, e. g. for the sample shown in Figure 3.3(a)  $C_{\text{SWNT-film}} = 155.86 \text{ pF}$ . A comparison of the capacitance values and the nanotube film extension as estimated by SEM and light microscopy reveals a clear correlation between these quantities, which can be explained qualitatively in the model of a parallel plate capacitor ( $C \propto A_{\text{SWNT-film}}/d_{\text{Al}_2\text{O}_3}$ , with the area of the nanotube film  $A_{\text{SWNT-film}}$

<sup>3</sup>SEM images of the nanotubes deposited on those samples are shown in Figure 3.6(a) and Figure B.3.

and the oxide thickness  $d_{Al_2O_3}$ ). A detailed analysis of the functional dependence was not in the focus of this work.

A very different situation is observed in the case of the Au electrodes, as presented in Figure 3.3(b). This sample was prepared with a deposition frequency  $f = 300$  kHz.<sup>4</sup> Due to severe heat dissipation the duration and period of the pulsed AC-voltage were reduced to  $t_{ON} = 0.5$  ms and  $\tau = 4$  ms and the deposition was stopped after only  $t \approx 5$  s. The sample shows a purely ohmic behavior ( $\Theta \approx 0^\circ$ ) and the resistance is  $R = 7.69 \Omega$ . These results clearly demonstrate that the aluminum oxide layer inhibits a metallic contact of the nanotubes to the electrodes—which leads to a short-circuiting of the AC voltage, obstructing further dielectrophoresis—and thereby allows for an assembly of continuous nanotube films.

### Impedance spectra in the high-frequency range

As stated before, the impedance of a few samples was additionally measured in the high-frequency range. The spectra presented in Figure 3.4 were obtained by combining the data of the LCR Meter ( $f = 50$ – $10^6$  Hz) and the Network Analyzer ( $f = 3 \cdot 10^5$ – $1.3 \cdot 10^9$  Hz). The results of the two measurement methods match very well.

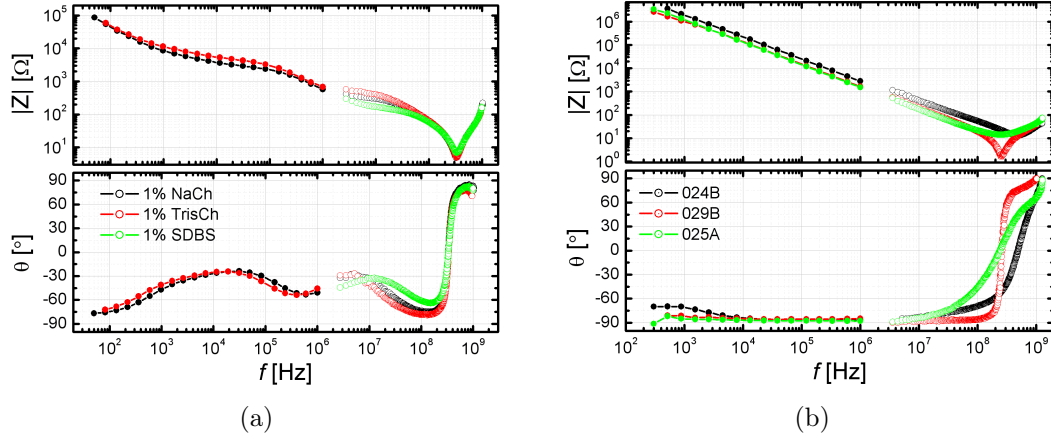


**Figure 3.4:** Combined impedance spectra in the low- and high-frequency range for the interdigitated electrode structure after application of  $15 \mu\text{l}$  of pure surfactant solution (no nanotubes) (a) and for several samples containing nanotube films (b). In the high frequency range ( $f > 200$  MHz) the total impedance is dominated by an inductive component, that originates from the interdigitated electrode structure. The ‘wave-like’ variation of the impedance in (a) is caused by the presence of constant phase elements (CPEs).

<sup>4</sup>The absence of an insulating oxide layer in the case of Au electrodes allows for a deposition at low frequencies.

The impedance spectra of the interdigitated electrode structure after application of  $15 \mu\text{l}$  of pure surfactant solution (no nanotubes) of various types is presented in Figure 3.4(a). Figure 3.4(b) shows the impedance spectra of several samples prepared by dielectrophoresis from nanotubes dispersed in TrisCh (suspension # 26.3) with  $t = 10 \text{ min}$ ,  $t_{\text{ON}} = 10 \text{ ms}$ ,  $\tau = 80 \text{ ms}$  and  $f = 10 \text{ MHz}$ . SEM images of the corresponding samples are shown in Figures B.1(a), B.1(b) and B.2. Two interesting features can be observed in these plots: In the high-frequency range ( $f > 200 \text{ MHz}$ ) the total impedance is dominated by an inductive component. Since this inductance is present in both systems, it must originate from the interdigitated electrode structure or the wiring that is used to contact the devices and does not result from the presence of nanotubes. Furthermore there is a ‘wave-like’ variation of the impedance in Figure 3.4(a). These can be explained by so-called constant phase elements (CPEs). Following the notation of Reference [82], the impedance of a constant phase element  $Q$  is given by  $1/Z = (i\omega)^n A_0$  with  $0 \leq n \leq 1.0$ . For  $n$  close to 1.0, the CPE resembles a capacitor with a constant phase angle somewhat less than  $90^\circ$ . CPEs have been identified in electrical circuits containing metal-insulator-liquid interfaces [83].

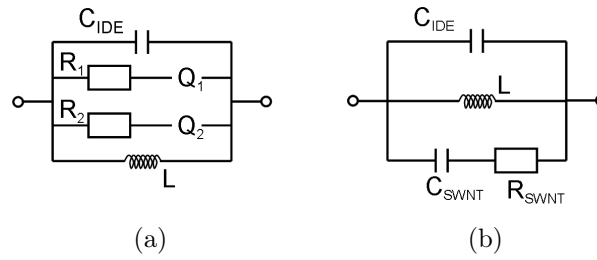
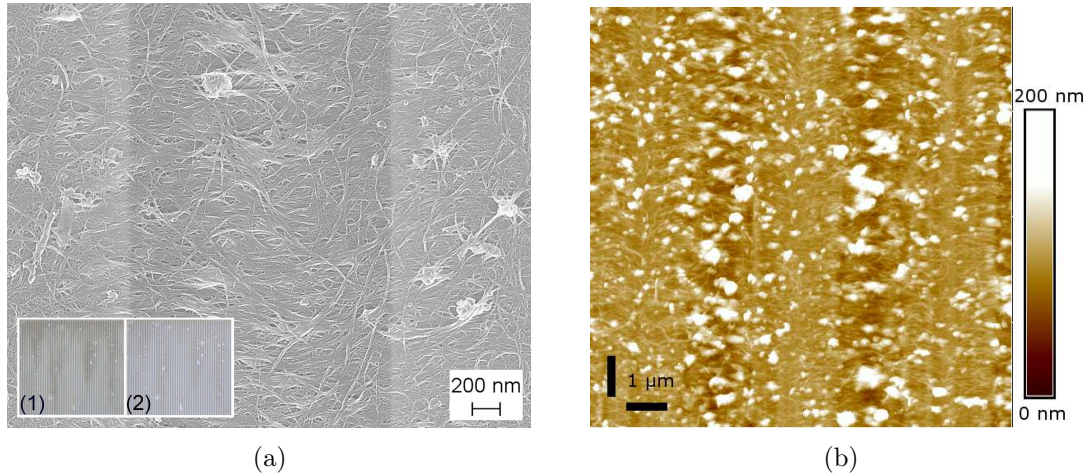


**Figure 3.5:** Equivalent circuit for interdigitated electrode structures with pure surfactant solution (a) or in the presence of a nanotube film (b). In subfigure (a),  $Q_1$  and  $Q_2$  mark the constant phase elements.

The equivalent circuits for the interdigitated electrode structures with nanotube film or surfactant solution are illustrated in Figures 3.5(b) and 3.5(a), respectively. Assuming these networks the impedance spectra can be fitted. However, the fit involves up to 7 parameters and its result strongly depends on the choice of initial values. Therefore only the order of magnitude of the parameters will be reported here: As stated before, the capacitance of the interdigitated electrodes and of the nanotube film are  $C_{\text{IDE}} \approx 1 \text{ pF}$  and  $C_{\text{SWNT-film}} \approx 10\text{--}100 \text{ pF}$ . The other parameters were determined as: inductance  $L \approx 10^{-8} \text{ H}$ , resistors  $R_1 \approx 1 \text{ k}\Omega$  and  $R_2 \approx 10 \text{ k}\Omega$  and CPEs  $Q_1$  and  $Q_2$  with  $n \approx 0.8$ ,  $A_{0,1} = A_{0,2} \approx 10^{-7} \text{ F}$ . The two parallel resistances arise from an ohmic conduction through the liquid between the electrode fingers on the one hand and between the large bonding pads on the other hand (see Figure 3.1).

## 3.2. Results and discussion

### 3.2.1. Polarization dependent absorbance spectra of SWNT films



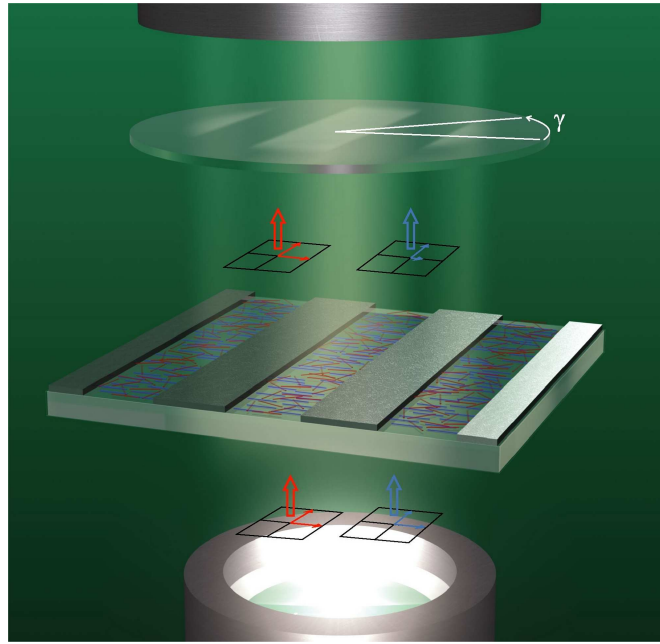
**Figure 3.6:** SEM and AFM image of a SWNT film on interdigitated electrodes. (a) The SEM image shows a section of the sample containing one gap (dark gray area) and two half electrodes (light gray areas), both covered completely with a continuous film of dielectrophoretically deposited nanotubes. (b) AFM image of the same SWNT film (with different magnification). The areas with light brown background correspond to three electrodes, the darker background marks the gaps. The thickness of the nanotube film is  $\sim 60$  nm. The inset in (a) shows incident-light dark-field micrographs of a larger area of a sample. The comparison between two different settings of the analyzer, perpendicular to the electrode fingers in (1) and parallel to them in (2), unveils a difference in the absorption of the nanotube film. Modified from Ref. [84].

Figure 3.6(a) shows a SEM image of a sample prepared from nanotubes dispersed in NaCh (Suspension #24.4, see Figure A.1) using the standard pulsed deposition method described before. The image clearly demonstrates that the interdigitated electrode array is completely covered by a continuous film of nanotubes. Incident-light dark-field micrographs of a larger area of the same sample are presented in the inset. The comparison between two different settings of the analyzer, perpendicular to the electrode fingers in (1) and parallel to them in (2), unveils a difference in the absorption of the nanotube film. This effect will be studied in greater detail in the following. An atomic force microscopy image of the same SWNT film is presented in Figure 3.6(b). The thickness of the nanotube film was determined to  $\sim 60$  nm.<sup>5</sup>

<sup>5</sup>The film thickness is strongly correlated to the concentration of the nanotube suspension used for the dielectrophoretic deposition and the deposition time. For a fixed deposition voltage the maximum film thickness is expected to be limited due to screening of the electric field

To measure the absorption spectra of the nanotube films, a Fourier transform infrared spectrometer (Bruker Equinox 55) combined with an infrared microscope (Bruker Hyperion 2000) was used. In addition to the setup used in Reference [26], an analyzer is inserted into the light path between sample and detector. This allows to investigate the difference in absorption that became apparent in the incident light micrographs presented in Figure 3.6(a).

A schematic of the measurement setup is illustrated in Figure 3.7. Non polarized light from the light source passes through an aperture and illuminates the sample from the bottom. Since the electrodes are non-transparent, light passes only through the gaps and is partly absorbed by the SWNT film. By varying the angle  $\gamma$  of the analyzer the polarization dependence of the absorption is determined. As discussed in Section 2.1.3, SWNTs preferentially absorb the component of the light parallel to the nanotube axis due to a large depolarization effect [45]. It is therefore possible to determine the alignment of nanotubes in a sample by analyzing the polarization dependence of the absorption spectra [85].



**Figure 3.7:** Schematic of the setup used for polarization dependent absorption measurements on dielectrophoretically deposited SWNTs. Non-polarized light illuminates the sample from the bottom and is partly absorbed by the nanotube film covering the electrode gaps. An analyzer between sample and detector allows for polarization dependent measurements. Taken from Ref. [84].

The black curves in Figure 3.8 show absorption spectra measured on the sample shown in Figure 3.6(a). The spectral range was chosen to cover the M1 absorp-

---

by the nanotube film.

tion band of metallic SWNTs (centered around 650 nm for NiCo nanotubes) as well as the S2 absorption band of semiconducting nanotubes (centered around 950 nm) [48]. The main observation is that the shape of the S2-peak is virtually independent of the setting of the analyzer, which is characterized by the angle  $\gamma$  between the axis of the analyzer and the direction of the external electric field during the dielectrophoretic deposition. By contrast, the height of the M1 peak depends strongly on the analyzer setting. It is very pronounced for  $\gamma = 0^\circ$  and almost completely suppressed for  $\gamma = 90^\circ$ . A similar behavior was observed in samples prepared by dielectrophoresis of SWNTs dispersed with different surfactants and length distributions but comparable deposition parameters (see Figures B.4-B.7).

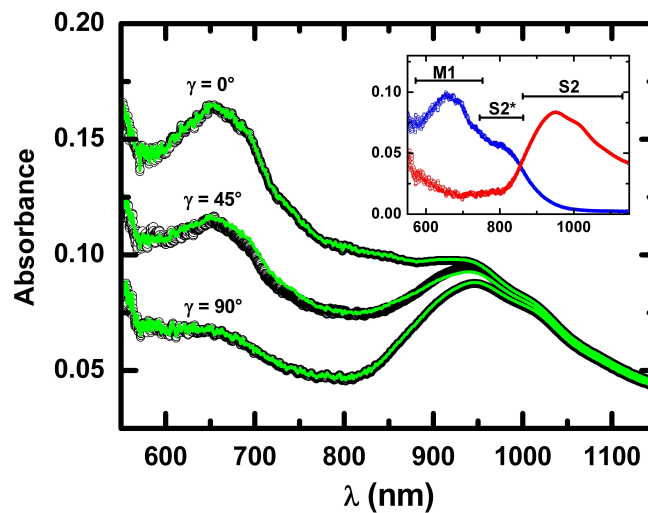


**Figure 3.8:** Absorbance spectra for three settings of the analyzer (black curves). The angle  $\gamma$  is defined with respect to the external field during deposition. While the peak around 650 nm, which corresponds to metallic nanotubes (M1), strongly depends on the setting of the analyzer, the peak around 950 nm, corresponding to semiconducting nanotubes (S2), is virtually independent. However, there is a fraction of small diameter semiconducting nanotubes (S2\*), that show a similar dependence as the metallic nanotubes. Note that this S2\* shoulder at  $\sim 800$  nm can be seen more clearly in the raw data of Figures B.4-B.7. Green curves: fitted data using the basic spectral data M1/S2\* and S2 shown in the inset and fit parameters given in the text. Taken from Ref. [84].

Obviously the degree of alignment of metallic and semiconducting nanotubes differs greatly in the sample. Metallic nanotubes are well aligned and their preferential orientation is parallel to the electric field during the deposition process. The majority of the semiconducting nanotubes are randomly oriented, but small-diameter semiconducting nanotubes (S2\* at  $\sim 800$  nm, see Reference [48]) show an alignment similar to the metallic nanotubes. There are two important conclusions to be drawn from this analysis: (1) the SWNTs are deposited individually, not in bundles; (2) although both nanotube types apparently undergo positive dielec-

trophoresis for the chosen experimental conditions, their response to the external electric field is different. In addition to the absorbance measurements, Raman spectroscopy was performed on the same sample. The data confirm the incisively different degree of alignment of the two nanotube types (see Figures B.8 and B.9).<sup>6</sup>

### 3.2.2. Advanced model for nanotube dielectrophoresis

In Section 2.2 the basic theory of dielectrophoresis was introduced and its application to the case of single-walled carbon nanotubes was presented. In particular, it was shown that any experimental results reported earlier in this field of work could be explained with Equation (2.23). However, the different forms of alignment of metallic and semiconducting nanotubes reported here can not be accounted for in this framework.

In the derivation of Equation (2.23), a certain orientation of the nanotube with respect to the external electric field was assumed: the particle was considered to be both aligned with its long axis parallel to the electric field and positioned on the axis of an axially symmetric field. In a more general picture, the orientation will be defined on the one hand by the torque  $\vec{T} = \vec{p}_{\text{eff}} \times \vec{E}_{\text{ext}}$  generating a rotational movement into the orientation for which the potential energy  $U$  is minimal. On the other hand the particle undergoes a random brownian motion associated with the thermal energy  $k_B T$ , with the Boltzmann constant  $k_B = 1.381 \cdot 10^{-23}$  J/K. Consequently, the assumption of a specific orientation is a severe simplification. Additionally, so far only the polarizability along the nanotube axis was taken into account. Thereby the strong anisotropy exhibited by SWNTs in both their structure as well as their dielectric properties (see Section 2.1.2) was neglected. In the following an advanced model for nanotube dielectrophoresis will be presented which incorporates explicitly their longitudinal and transverse polarizability.

#### The effective dipole moment in global coordinates

The nanotube is approximated by a rod-shaped particle ( $a \gg b = c$ ) with arbitrary orientation with respect to a fixed reference frame ( $x, y, z$  coordinates). The particle's coordinate system with axes 1, 2, 3 is chosen such that the 1-axis is parallel to the long axis of the rod-like particle. Since  $b = c$ , the orientation of the axes 2 and 3 is not defined and can be chosen according to the problem on hand, respecting the right hand convention. Let  $\varphi$  denote the angle between the global  $x$ -axis and the projection of the 1-axis onto the  $x$ - $y$ -plane and  $\theta$  be the angle between the  $z$ -axis and the 1-axis as depicted in Figure 3.9. This choice then corresponds to the common spherical coordinate system with  $0 \leq \varphi < 2\pi$  as azimuthal angle and  $0 \leq \theta < \pi$  as polar angle.

---

<sup>6</sup>The case of the S2\* nanotubes will be discussed in Section 3.2.3.

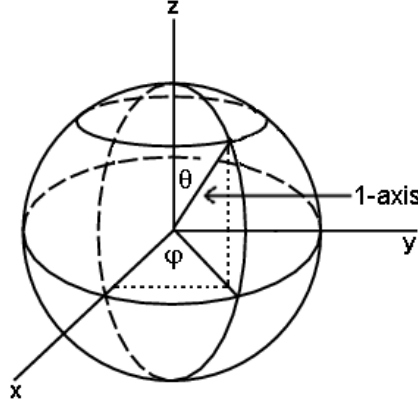


**Figure 3.9:** Cartesian and spherical coordinates. The 1-axis corresponds to the nanotube axis.

Using  $a \approx 1 \mu\text{m}$  and  $b = c \approx 1 \text{ nm}$ , it follows that  $L_{\parallel} \equiv L_1 \approx \frac{b^2}{a^2} [\ln(\frac{2a}{b}) - 1] \approx 10^{-5}$  and  $L_{\perp} \equiv L_2 = L_3 \approx 1/2$ . With the definition of

$$\alpha_{\parallel} \equiv \alpha_{11} \approx \frac{4\pi ab^2}{3} \varepsilon_{\ell} \Re \left( \frac{\varepsilon_{\text{p},\parallel}^* - \varepsilon_{\ell}^*}{\varepsilon_{\ell}^*} \right) \quad \text{and} \quad (3.1)$$

$$\alpha_{\perp} \equiv \alpha_{22} \approx \alpha_{33} = \frac{4\pi ab^2}{3} \varepsilon_{\ell} \Re \left( \frac{\varepsilon_{\text{p},\perp}^* - \varepsilon_{\ell}^*}{\varepsilon_{\ell}^* + \varepsilon_{\text{p},\perp}^*} \right) \quad (3.2)$$

the effective moment in the global coordinate system is given by

$$\vec{p}_{\text{eff}} = \begin{pmatrix} \alpha_{\perp} s_{\varphi}^2 + c_{\varphi}^2 (\alpha_{\parallel} - c_{\theta}^2 \Delta_{\alpha}) & \Delta_{\alpha} s_{\varphi} c_{\varphi} s_{\theta}^2 & \Delta_{\alpha} c_{\varphi} c_{\theta} s_{\theta} \\ \Delta_{\alpha} s_{\varphi} c_{\varphi} s^2 \theta & \alpha_{\perp} s_{\varphi}^2 + c_{\varphi}^2 (\alpha_{\parallel} - c_{\theta}^2 \Delta_{\alpha}) & \Delta_{\alpha} s_{\varphi} c_{\theta} s_{\theta} \\ \Delta_{\alpha} c_{\varphi} c_{\theta} s_{\theta} & \Delta_{\alpha} s_{\varphi} c_{\theta} s_{\theta} & \alpha_{\parallel} c_{\theta}^2 + \alpha_{\perp} s_{\theta}^2 \end{pmatrix} \vec{E}_0 \quad (3.3)$$

(with  $s_{\varphi} \equiv \sin(\varphi)$ ,  $c_{\varphi} \equiv \cos(\varphi)$ ,  $s_{\theta} \equiv \sin(\theta)$ ,  $c_{\theta} \equiv \cos(\theta)$  and  $\Delta_{\alpha} \equiv \alpha_{\parallel} - \alpha_{\perp}$ ). The derivation of this expression is presented in Appendix C.

When considering 2 dimensional problems, this reduces to

$$\vec{p}_{\text{eff}} = \begin{pmatrix} \alpha_{\parallel} \cos^2 \varphi + \alpha_{\perp} \sin^2 \varphi & (\alpha_{\parallel} - \alpha_{\perp}) \sin \varphi \cos \varphi \\ (\alpha_{\parallel} - \alpha_{\perp}) \sin \varphi \cos \varphi & \alpha_{\parallel} \sin^2 \varphi + \alpha_{\perp} \cos^2 \varphi \end{pmatrix} \vec{E}_0. \quad (3.4)$$

### Dielectrophoretic torque and potential energy

A lossless particle achieves equilibrium when any of its three principal axes is parallel to the external field  $\vec{E}_0$ . The only stable orientation, though, is that one with the longest axis aligned parallel to the field vector, no matter what the relative magnitudes of  $\varepsilon_{\ell}$  and  $\varepsilon_{\text{p}}$  are [69].

For lossy particles the situation is more complex, as the stable orientation now depends on the field frequency. Depending on the relation between the complex dielectric functions of the particle and the surrounding liquid, abrupt changes from one stable orientation into another can be observed at certain critical frequencies. This can be explained by the fact that a distinct relaxation time of the Maxwell-Wagner polarization exists for each of the three principal axes. These relaxation times and the corresponding critical frequencies are defined as

$$f_{\alpha}^{\text{MW}} = [\tau_{\alpha}^{\text{MW}}]^{-1} = \frac{(1 - L_{\alpha})\sigma_{\ell} + L_{\alpha}\sigma_{\text{p},\alpha}}{(1 - L_{\alpha})\varepsilon_{\ell} + L_{\alpha}\varepsilon_{\text{p},\alpha}}, \quad \alpha = 1, 2, 3. \quad (3.5)$$

As stated before, for a rod-shaped particle the orientation of the 2- and 3-axes can be chosen freely. The easiest approach for the torque calculation is to define the 2-axis such that the vector of the electric field lies within the 1-2-plane and therefore  $E_{0,3} = 0$ . In this case,  $\langle T_{\text{DEP}} \rangle_1 = \langle T_{\text{DEP}} \rangle_2 \equiv 0$ .<sup>7</sup>

Then  $\langle T_{\text{DEP}} \rangle_3$  is given by

$$\begin{aligned} \langle T_{\text{DEP}} \rangle_3 &= \frac{1}{2} E_{0,1} E_{0,2} [\alpha_{\parallel} - \alpha_{\perp}] \\ &= \frac{1}{2} E_0^2 [\alpha_{\parallel} - \alpha_{\perp}] \sin \phi \cos \phi, \end{aligned} \quad (3.6)$$

with  $\phi$  denoting the angle between the 1-axis of the particle and the electric field vector  $\vec{E}_0$  and therefore  $E_{0,1} = E_0 \cos \phi$  and  $E_{0,2} = E_0 \sin \phi$ .

Using Equation (3.6) the rotational energy for a rod-shaped particle can be derived

$$\begin{aligned} U_{\text{rot}} &= \int \langle T_{\text{DEP}} \rangle_3 d\phi = -\frac{1}{4} E_0^2 [\alpha_{\parallel} - \alpha_{\perp}] \cos^2 \phi \\ &\equiv U_0 \cos^2 \phi. \end{aligned} \quad (3.7)$$

### Nematic order parameter

During a dielectrophoretic deposition experiment, both translational and rotational movement activated by the dielectrophoretic force and torque respectively are opposed by the random Brownian motion of the nanotubes due to their thermal energy. Therefore, the degree of alignment of the nanotubes in suspension and the efficiency of their deposition or repulsion depends on the relation between the rotational energy  $U_{\text{rot}}$  or the translational energy  $U_{\text{DEP}} = \int \langle F_{\text{DEP},z} \rangle dz$  on the one hand and the thermal energy  $k_B T$  on the other hand.

---

<sup>7</sup>Note that  $\langle T_{\text{DEP}} \rangle_1 \equiv 0$  independent of the chosen orientation of the 2- and 3-axes, since  $L_2 = L_3$ .

The torque (and the rotational energy) acting on each individual nanotube is a quantity which is not accessible in a typical dielectrophoresis experiment used in this work. However, the average alignment of the collectivity of nanotubes can be determined experimentally.

The ensemble of such particles can be described by the theory of liquid crystals [86, 87]. Liquid crystals are a form of condensed matter which can exhibit long-range orientational order in the absence of translational order. These systems consist of highly anisotropic molecules, which can be approximated by rigid rods or ellipsoids with lengths  $l$  much greater than their widths  $d$ . In the isotropic phase, both orientation and position of the particles are random. In the so called nematic phase the orientation is no longer arbitrary, but the particles tend to be aligned parallel to a common axis (specified by the unit vector  $\vec{n}$ , called director).

The degree of alignment can be measured by an order parameter, which is zero in the disordered phase and non-zero in the ordered phase. For liquid crystals the order parameter  $S$  is a function of the unit vector  $\vec{v}^\alpha$  pointing along the long axis of molecule  $\alpha$  at position  $\vec{r}^\alpha$ . Since the orientations parallel or anti-parallel to the director are equally probable, the order parameter must be even in  $\vec{v}^\alpha$ . It can be shown that for three-dimensional problems the nematic order parameter is

$$S_{3d} = \frac{1}{2} \overline{(3(\vec{v}^\alpha \cdot \vec{n})^2 - 1)} = \frac{1}{2} \left( 3 \overline{(\cos^2 \theta^\alpha)} - 1 \right), \quad (3.8)$$

where  $\theta^\alpha$  is the angle between the long axis of the molecule and the director and the bare indicates the mean value for the ensemble of molecules. For two-dimensional problems

$$S_{2d} = \overline{(2(\vec{v}^\alpha \cdot \vec{n})^2 - 1)} = 2\overline{(\cos^2 \theta^\alpha)} - 1 = \overline{(\cos 2\theta^\alpha)}. \quad (3.9)$$

Considering the degree of alignment of carbon nanotubes in an external electric field, the director is defined by the direction of the external field and therefore  $\theta^\alpha$  is equal to the angle  $\phi$  defined above.

To calculate the expected values of  $\cos^2 \phi$ , a distribution function for  $\phi$  is needed. Since the alignment of each individual particle is controlled by the rotational energy  $U_{\text{rot}}$  compared to the thermal energy  $k_B T$ , the Boltzmann distribution function is used

$$f(\phi)d\Omega = \frac{\exp(-U_{\text{rot}}/k_B T)d\Omega}{\int \exp(-U_{\text{rot}}/k_B T)d\Omega} \quad (3.10)$$

The differential  $d\Omega$  has to be chosen according to the dimensionality of the specific problem. Considering the alignment of the particles within a two-dimensional plane, e. g. the  $x$ - $y$  plane of the sample surface, the differential reduces to  $d\varphi$ . If the coordinate system is chosen such that the direction of the electric field

corresponds to the  $x$ -axis, then  $\varphi \equiv \phi$ . In the case of a three-dimensional problem with external field  $\vec{E}_0 = E_0 \hat{z}$ , the potential energy depends only on the polar angle  $\theta$  and therefore  $d\Omega = \sin\theta d\theta d\varphi = 2\pi \sin\theta d\theta$ . The direction of the rod-shaped particles is then confined to lie within a cone with average angle  $\langle\theta\rangle$ .

### 3.2.3. Application to the experimental results

The model sketched above will now be employed to analyze the experimental results, in particular the observation that the two nanotube types show a distinct deposition pattern with a high degree of alignment of metallic SWNTs and a random orientation of semiconducting nanotubes. The deposition of semiconducting nanotubes at high frequencies will be discussed in Section 4.3.

#### Calculation of the average alignment on the sample surface

In a first step the average alignment of single-walled carbon nanotubes in suspension under the influence of an external field is calculated. The experimentally accessible quantity is the degree of alignment of nanotubes deposited by dielectrophoresis onto a sample surface, which can be extracted from the polarization dependent absorption spectra. Therefore the two-dimensional nematic order parameter  $S_{2d}$  is calculated using the projection of the electric field vector during deposition onto a plane parallel to the sample surface (the  $x$ - $y$  plane) as common axis. With the appropriate choice of the coordinate system and combining Equations (3.7), (3.9) and (3.10), it follows

$$S_{2d} = \overline{(\cos 2\varphi)} = \int_{-\pi/2}^{\pi/2} \cos 2\varphi \cdot f(\varphi, U_0) d\varphi \quad \text{and} \quad (3.11)$$

$$f(\varphi, U_0) = \frac{\exp(-U_0 \cos^2 \varphi / k_B T)}{\int_{-\pi/2}^{\pi/2} \exp(-U_0 \cos^2 \varphi / k_B T) d\varphi}. \quad (3.12)$$

Figure 3.10 shows the result of the calculation assuming the following geometric and dielectric properties of the nanotube: length  $l = 0.5 \mu\text{m}$  and diameter  $d = 1 \text{ nm}$ , depolarization factors  $L_{||} = 10^{-5}$  and  $L_{\perp} = 0.5$ , an isotropic conductivity of both metallic and semiconducting nanotubes of  $\sigma_p = 0.35 \text{ S/m}$ <sup>8</sup> and permittivities  $\varepsilon_{||}^{\text{met}} = 10^4 \varepsilon_0$  and  $\varepsilon_{\perp}^{\text{met}} = \varepsilon_{\perp,||}^{\text{semi}} = 30 \varepsilon_0$ . For the surfactant suspension  $\sigma_{\ell} = 0.1 \text{ S/m}$  and  $\varepsilon_{\ell} = 85 \varepsilon_0$  was used.

---

<sup>8</sup>In Reference [25] it was argued that the conductivity of micellated semiconducting nanotubes is dominated by surface conductivity rather than the intrinsic conductivity. Also, the dielectrophoretic forces acting on metallic nanotubes in the low-frequency regime are comparable to those acting on semiconducting SWNTs, indicating a similar value of the conductivity. Therefore, an equal and isotropic value of  $\sigma_p$  is assumed here for both nanotube types.

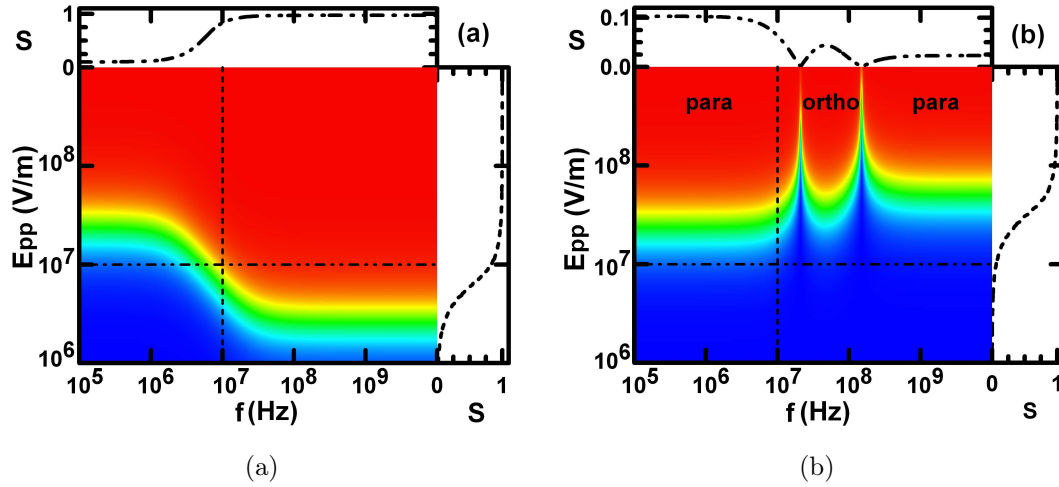


**Figure 3.10:** Nematic order parameter  $S$  as a function of the frequency  $f$  and amplitude  $E_{pp}$  of the applied electric field. (a) Metallic nanotubes: Moderate deposition parameters lead to a high degree of alignment in the high-frequency range. (b) Semiconducting nanotubes: While the alignment at low frequencies resembles that of metallic nanotubes, the situation changes drastically for  $f > 10^6$  Hz: much higher field strengths are necessary to overcome the random orientation and two turn-over frequencies ( $f_{1,2}^{TO}$ ) are predicted, which mark the transition from one stable orientation into another. Taken from Ref. [84].

The nematic order parameter  $S$  for metallic nanotubes is shown in Figure 3.10(a), while Figure 3.10(b) illustrates the predicted alignment for semiconducting nanotubes. The values of  $S$  are color coded from blue ( $S = 0$ ) to red ( $S = 1$ ). Also shown are sections of the contour plot, tracing  $S$  at the frequency  $10^7$  Hz and electric field amplitude  $10^7$  V/m. For low frequencies ( $f < 10^6$  Hz) the conductivity dominates the polarizability and the alignment of both nanotube types is equal. For high frequencies, moderate field strengths suffice to perfectly align the metallic nanotubes. The semiconducting nanotubes, on the other hand, are randomly oriented up to much higher field strengths. Once this random orientation is overcome, the stable orientation with respect to the external field depends on the frequency. Two turn-over frequencies ( $f_{1,2}^{TO}$ ) mark the transitions from parallel to orthogonal and again to parallel alignment.

### Analysis of the absorption spectra

To analyze the absorption spectra presented in Figure 3.8, two sets of basic spectral data are extracted in the first step, one of them describing the absorption of the aligned nanotubes, the other one representing the randomly oriented nanotubes. The first set of data, corresponding to M1/S2\* in the inset of Figure 3.8, is obtained by subtracting the data of the measurement with  $\gamma = 90^\circ$  from the measurement with  $\gamma = 0^\circ$ , thereby eliminating the polarization independent con-

tributions. To generate the basic spectrum of the randomly oriented nanotubes (S2), the plain data of the  $90^\circ$  measurement cannot be used, because there is obviously some contribution between 600 and 800 nm from the aligned nanotubes. Therefore the data of the  $0^\circ$  measurement is modified by subtracting a fraction of the M1/S2\* data until a flat background between 600 and 800 nm is obtained.

With this choice of basic spectra the absorbance  $Abs$  for a specific angle  $\gamma$  is given by the function [88]

$$Abs(\gamma) = \frac{1}{\int_{-\pi/2}^{\pi/2} \cos^2(\varphi - \gamma) d\varphi} \cdot \int_{-\pi/2}^{\pi/2} \left[ Abs_{M1/S2^*} f(\varphi, U_0^{M1/S2^*}) + Abs_{S2} f(\varphi, U_0^{S2}) \right] \cos^2(\varphi - \gamma) d\varphi \quad (3.13)$$

A large value of  $U_0$  then corresponds to a narrow angular distribution, while a small value matches a wide angular distribution. The green curves shown in Figure 3.8 were obtained using for the M1/S2\* tubes a value of  $U_0^{M1/S2^*}/k_B T = 2.3$  and for the S2 nanotubes a value of  $U_0^{S2}/k_B T = 0$ . The values for  $U_0$  are consistent with model calculations for SWNTs close to the substrate surface ( $\sim 1 \mu\text{m}$ ). This self-consistency as well as the excellent agreement of the fit with the measured data justifies the procedure for constructing the S2 spectrum.

Obviously, the different forms of alignment of metallic and semiconducting nanotubes strongly affect the determination of the composition of samples by optical absorption spectroscopy. A simple comparison of the peak heights or the peak area measured with non-polarized light will not render the correct result, since the amount of metallic nanotubes will be underestimated. For instance, even if aligned nanotubes would absorb all parallelly polarized light, the absorbance measured with non-polarized light would never exceed 0.3. The fitting procedure described above depends strongly on the choice of the basic spectra and is therefore not appropriate for a quantitative analysis of the sample composition.

It remains to be discussed why the alignment of small-diameter semiconducting nanotubes S2\* resembles that of metallic nanotubes M1. As the conductivity  $\sigma_p$  of all nanotubes was assumed to be dominated by the surface conductance  $\kappa$ , a smaller nanotube diameter  $d$  results in a bigger value of  $\sigma_2 \propto \kappa/d$  [25, 89, 90] and therefore a larger value of  $U_0$ , which increases the alignment. Another possible explanation would be a diameter-selective dispersion of the nanotubes in the surfactant, which allows for residual bundles of small-diameter semiconducting nanotubes with metallic nanotubes. A comparison of fluorescence maps of nanotubes dispersed in SDS (sodium dodecyl sulfate) and SDBS indeed suggests such selectivity in the case of SDBS [48]. Further analysis is necessary to verify either of these interpretations.

## Summary

The dielectrophoretic deposition of single-walled carbon nanotubes onto interdigitated electrodes was studied under variation of the experimental parameters. It was shown that the insulating oxide layer which covers the surface of aluminum electrodes allows for the production of continuous films of carbon nanotubes on the electrode array. The application of very large electric fields during the deposition process leads to a strikingly different alignment behavior of metallic and semiconducting nanotubes, which was analyzed using polarization dependent absorption measurements. The experimental results show that the model of nanotube dielectrophoresis, which has been used so far and is based on a scalar dependence of the polarizability of the external field, is not sufficient to describe the dielectrophoretic deposition of SWNTs due to their structural and dielectric anisotropy. Within an advanced model that also incorporates contributions from the polarizability orthogonal to the nanotube axis, the observed high degree of alignment of metallic nanotubes and the random orientation of semiconducting nanotubes can be explained.

Another experimental observation is the deposition of semiconducting nanotubes at frequencies above the cross-over frequency observed before. The advanced dielectrophoresis model predicts the existence of a further critical frequency,  $f_{c,\perp}$ , defined by the transversal dielectric properties of single-walled carbon nanotubes. As a result, semiconducting nanotubes exposed to very large electric fields experience a positive dielectrophoresis above the cross-over frequency defined before, which corresponds to the cross-over defined by the longitudinal dielectric properties. The decisive influence of the orthogonal polarizability onto the dielectric force acting on semiconducting nanotubes will be illustrated by means of finite element simulations in Section 4.3.

## 4. Finite element simulations

A major part of this work aimed at explaining the dielectrophoretic forces that were experimentally realized at INT in various electrode setups by finite element simulations. These simulations, which will be presented in this chapter, are motivated by experimental findings in the context of dielectrophoretic separation or assembly. The corresponding experiments were carried out by Christoph W. Marquardt (Section 4.1), Aravind Vijayaraghavan (Sections 4.2 and 4.4) and by the author of this work (Section 4.3). The results of the simulations allow for a deeper understanding of the experimental observations.

### 4.1. Probing dielectrophoretic force fields with metallic carbon nanotubes

By studying the deposition pattern of single-walled carbon nanotubes on surfaces, it can be shown that carbon nanotubes are effective probes for dielectrophoretic force fields [91]. Different force fields were generated by electrodes on insulating oxides, with or without conducting substrates underneath. The patterns were recorded by scanning electron microscopy and simulated by finite element calculations. The data show that a sign change of the normal component of the dielectrophoretic force close to the substrate surface can lead to a repulsion of metallic carbon nanotubes from the surface. Geometrical constraints are presented to avoid such a sign change in the dielectrophoretic force.

#### Motivation

In this study, short, dispersed single-walled carbon nanotubes were exposed to two different types of dielectrophoretic force fields, which were generated by electrode structures of type *A*, microelectrodes on insulating substrates, and of type *B*, microelectrodes on oxidized conducting substrates. Type *A* structures are interdigitated electrodes of 140 nm thick aluminum with a gap of 1.8  $\mu\text{m}$ , prepared by optical lithography on 0.5 mm thick quartz substrates (see also Section 3.1). Type *B* structures are electrode pairs of 40 nm thick aluminum with a gap of 3  $\mu\text{m}$ , prepared by electron beam lithography on 0.5 mm thick oxidized *p*-type silicon substrate with 800 nm thermal oxide. For details about the experiment see Reference [91].

The analysis of the pattern formed by the dielectrophoretically deposited SWNTs reveals a systematic difference for the two types of structures. The SEM image of a type *A* structure in Figure 4.1(a) shows that the SWNTs are deposited homogeneously over the whole gap between the electrodes with some fluctuations in their spatial distribution. The same result was obtained for type *A* structures with a gap of  $4.4\ \mu\text{m}$  at the same electric field strength. Figure 4.2(a) shows an image from a type *B* structure. Obviously the distribution of SWNT is very different from the type *A* structure with SWNTs now deposited mainly in the vicinity of the electrodes. Note that under the chosen conditions with  $f = 50\ \text{MHz}$  primarily metallic SWNTs are attracted towards the electrodes as shown in Reference [25].

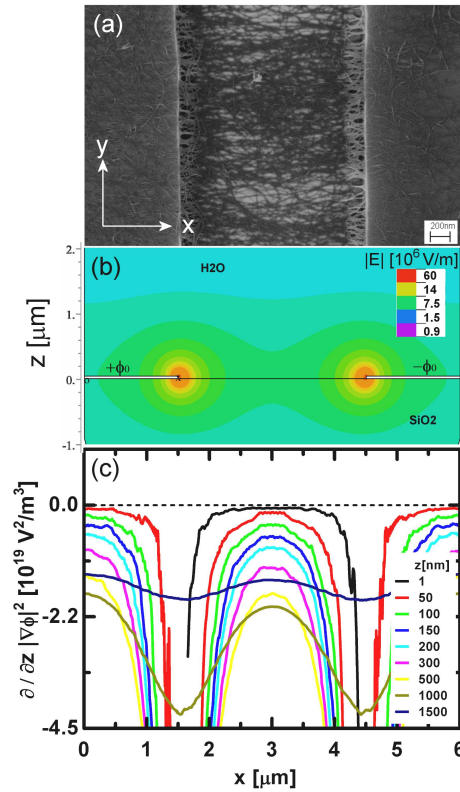


**Figure 4.1:** Type *A* structure on insulating quartz substrate. (a) Top view SEM image showing a homogeneous distribution of metallic SWNTs in the electrode gap. (b) Cross sectional plot of the magnitude of the electric field  $|E|$ . The applied potentials and the dielectric materials are indicated in the drawing. (c) The normal component of the dielectric force acting on metallic SWNTs,  $F_{\text{DEP},z}$  is proportional to  $\frac{\partial}{\partial z} |\nabla\Phi|^2$ , which is plotted for various heights  $z$  above the substrate surface. Metallic SWNTs feel attractive forces close to as well as far away from the substrate surface. Taken from Ref. [91].

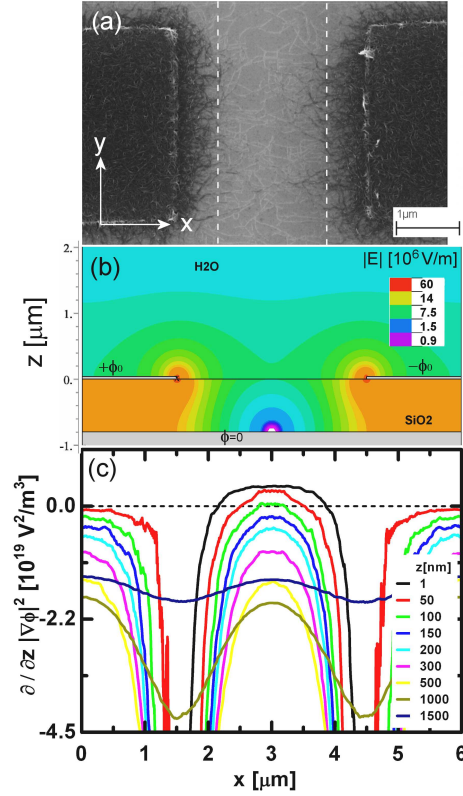


**Figure 4.2:** Type *B* structure on conducting p-type silicon substrate. (a) Top view SEM picture showing metallic SWNTs only in the vicinity of the electrodes. (b) Cross sectional plot of the magnitude of the electric field  $|E|$ . The applied potentials and the dielectric materials are indicated in the drawing. Note the 800 nm thick oxide layer. (c) The normal component of the dielectric force acting on metallic SWNTs,  $F_z^{\text{DEP}}$  is proportional to  $\frac{\partial}{\partial z} |\nabla\Phi|^2$ , which is plotted for various heights  $z$  above the substrate surface. In the center of the electrode gap at small heights  $\frac{\partial}{\partial z} |\nabla\Phi|^2 > 0$ , leading to a repulsion of metallic SWNTs from the surface. The area of repulsive forces for a height  $z = 1$  nm is indicated in (a) by the dashed white lines. Taken from Ref. [91].

### Details of the simulation

To validate the claim that the deposition patterns are directly related to the distribution of the dielectrophoretic force field, numerical field simulations were performed. Since the field frequency  $f = 50$  MHz is above the ionic charge relaxation frequency of sodium cholate,  $f_q \approx 20$  MHz, the partial differential equation to solve is the Laplace equation (2.34) with the potential at the electrodes equal to the applied potential  $\Phi_0 = \pm V_{pp}/2$ .

The extension of the interdigitated electrode fingers of the type *A* structures in  $y$  direction ( $\sim 360 \mu\text{m}$ ) is much larger than both the width of the electrode and the gap in  $x$  direction (each  $1.8 \mu\text{m}$ ). For calculations concerning type *A* structures

the three dimensional problem can therefore be reduced to a two dimensional one (defined in the  $x$ - $z$  plane). A similar approach was used for type  $B$  structures: The finite width of  $3\ \mu\text{m}$  in the  $y$  direction of the electrodes leads to non-zero  $y$ -components in the electric field. However within the  $x$ - $z$  plane along the electrode center, these components add up to zero. By neglecting the finite width in a two dimensional approach, the simulation is constrained to the center line.

For a better comparison of the simulation results the dimensions of the type  $A$  structure were slightly changed to match those of the type  $B$  structure. The unit cell of the type  $A$  structure then consists of two  $40\ \text{nm}$  thick half electrodes (each  $1.5\ \mu\text{m}$  wide) separated by a gap of  $3\ \mu\text{m}$ . The electrodes are situated on top of a  $100\ \mu\text{m}$  thick quartz substrate with permittivity  $\varepsilon = 5\varepsilon_0$ , and below a  $100\ \mu\text{m}$  thick water layer with  $\varepsilon = 80\varepsilon_0$ . The Neumann condition  $\partial\Phi/\partial n = 0$  was assigned to all boundaries of the unit cell [92]. The unit cell and boundary conditions of type  $B$  structure are based on the same model, however a conducting layer below  $800\ \text{nm}$  of  $\text{SiO}_2$  ( $\varepsilon = 5\varepsilon_0$ ) was added, representing the  $p$ -type silicon substrate. In the experiment the substrate is electrically floating—i. e. not connected to a voltage source—and acquires a certain potential through capacitive coupling. Due to the symmetric leads this potential will adjust to the mean potential of the biased electrodes ( $\Phi_0 = \pm V_{\text{pp}}/2$ ). In the electrostatic simulation this is accounted for by defining the potential at the surface of the floating layer as  $\Phi = 0$  and excluding the substrate volume from the simulation (see Section 2.3.3).

Figures 4.1(b) and 4.2(b) show the magnitude of the electric fields  $|\vec{E}(x, y)| = |\nabla\Phi|$  for the two electrodes structures as derived by the simulation. To calculate the corresponding dielectrophoretic force acting on a single-walled carbon nanotube, Equation (2.23) is employed. For the frequency and surfactant concentration used in the experiment, the prefactor of  $\nabla E^2$  is positive for metallic nanotubes and negative for semiconducting ones [26]. This means that only metallic nanotubes are attracted towards the regions of high field inhomogeneity due to their interaction with the electric field. With respect to the chosen coordinate system, a positive or negative value of  $\nabla E^2$  translates directly into repulsive or attractive forces for metallic nanotubes. Whether or not a metallic nanotube will be deposited on the surface depends thereby on the normal component of  $\nabla E^2$  in close proximity to the substrate surface ( $z < 1\ \mu\text{m}$ ). That quantity is plotted in Figures 4.1(c) and 4.2(c) as a function of the height  $z$  above the substrate surface.

## Results and Interpretation

The calculations show a strong dependence of the normal component of  $\nabla E^2$  on the distance to the substrate. For large distances from the surface ( $z > 1\ \mu\text{m}$ ), the corresponding forces are similar for the two types of structures. However near the surface the results differ significantly. For type  $A$  structures the forces are getting weaker towards the substrate surface but remain attractive. For type  $B$

structures on the other hand, the forces in the middle of the gap become repulsive for nanotubes which are closer than 100 nm to the surface. With decreasing  $z$ , the repulsive range extends further to the electrodes. This means that the nanotubes are pushed towards the electrodes when approaching the substrate. Comparing the deposition pattern in Figure 4.2(a) to the calculation, it becomes obvious that nanotube deposition is indeed absent within the region of repulsive forces as marked by the dashed lines, except for a few SWNTs of anticipated semiconducting type. The homogeneous deposition in Figure 4.1(a) is consequentially due to the absence of repulsive forces at the surface.

Type *B* structures are often used for device fabrication if a gate electrode is required. Table 4.1 presents the minimum oxide thickness that is required to avoid a sign change in the normal component of the dielectrophoretic force close to and far away from the surface for a number of electrode gap sizes and dielectric solvents.

|   | 1 $\mu\text{m}$ gap         | 2 $\mu\text{m}$ gap         | 3 $\mu\text{m}$ gap         |
|---|-----------------------------|-----------------------------|-----------------------------|
| Water ( $\varepsilon = 80\varepsilon_0$ )       | $0.66 \pm 0.02 \mu\text{m}$ | $1.4 \pm 0.03 \mu\text{m}$  | $1.75 \pm 0.05 \mu\text{m}$ |
| Isopropanol ( $\varepsilon = 12\varepsilon_0$ ) | $1.3 \pm 0.02 \mu\text{m}$  | $2.53 \pm 0.03 \mu\text{m}$ | $3.45 \pm 0.06 \mu\text{m}$ |

**Table 4.1:** Minimum oxide thickness required to avoid repulsion of metallic nanotubes ( $\partial/\partial z |\nabla\Phi|^2 \leq 0$  at 1 nm height) from the midpoint of the electrode gap, given as a function of the electrode gap size and of the dielectric solvent used for the dielectrophoretic deposition. Taken from Ref. [91].

## 4.2. Ultra-large-scale directed assembly of single-walled carbon nanotube devices

Recently, dielectrophoresis has been used to assemble a small number of devices of individual or bundled carbon nanotubes [12, 22, 23]. In this context a self-limiting single-nanotube assembly has been observed at the electrode gap under specific deposition conditions [12, 23]. The widely accepted mechanism for this phenomenon is the short-circuiting of the electrodes by the contacted object. However using impedance spectroscopy it was demonstrated that this mechanism can not explain the formation of single-tube devices [24]. Instead an alternate and more universal mechanism was suggested that involves redistribution of the electric field around the deposited nanotube in the electrode gap. This claim was backed by finite-element simulations, which will be presented in the following.

## Motivation

In Section 2.2.2 dielectrophoresis was introduced as a means to precisely assemble single-walled carbon nanotubes onto electrode pairs. Due to the capacitively coupled electrodes used in this deposition scheme, it was possible to upscale the deposition and produce high density arrays of individually accessible devices. Figure 4.3 shows a schematic of the electrode arrangement and nanotube deposition. The important feature of this setup is that only one of the surface electrodes (biased electrode, BE) is connected directly to the voltage source. The other electrode of each device is a floating counter electrode (CE). The AC voltage is applied between the BE and the underlying silicon gate electrode (GE). For high electric-field frequencies ( $\omega_d > 100$  kHz), the impedance of the CE/SiO<sub>2</sub>/GE structure ( $1/i\omega_d C_{CE-Ge}$ ) reduces significantly. The CE is now capacitively coupled to the GE and acquires a similar potential as that of the GE. This allows to bias all the distinct CEs without having to bond wires individually to each.

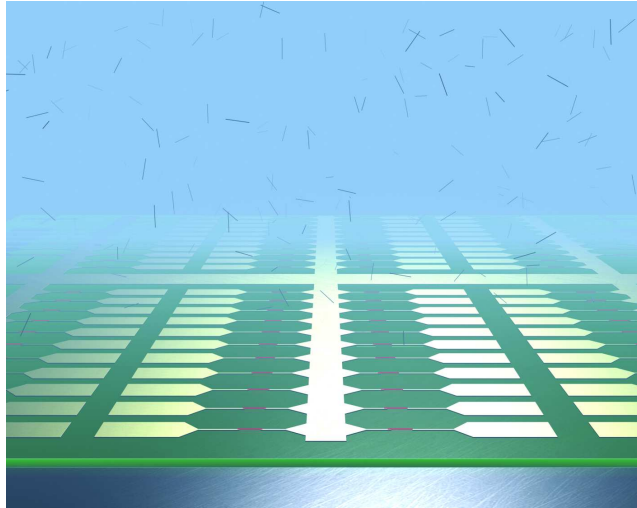


**Figure 4.3:** Schematic of the high-density array of single-tube devices, comprising of interconnected biased electrodes and counter electrodes (yellow) which are capacitively coupled to the p type silicon substrate (grey) via 800 nm of SiO<sub>2</sub> (green). Individual single walled carbon nanotubes (black) dispersed in aqueous surfactant solution (blue) form single tube devices (magenta) at a density of several million per square centimeter due to self-limiting dielectrophoretic assembly onto each of the 0.8  $\mu\text{m}$  wide electrode gaps. Taken from Ref. [24].

Depositions were performed at a frequency  $\omega_d = 300$  kHz to allow both metallic and semiconducting nanotubes to be deposited [12, 25]. Scanning electron microscopy (SEM) and atomic force microscopy (AFM) were used to count and image the deposited nanotubes. Figure 4.4(a) shows the bridging of 5 adjacent electrode pairs fabricated with the above scheme, which is representative of the whole array. Most of the electrode pairs were bridged by one individual nanotube or small bundle, as verified by AFM in Figure 4.4(b).

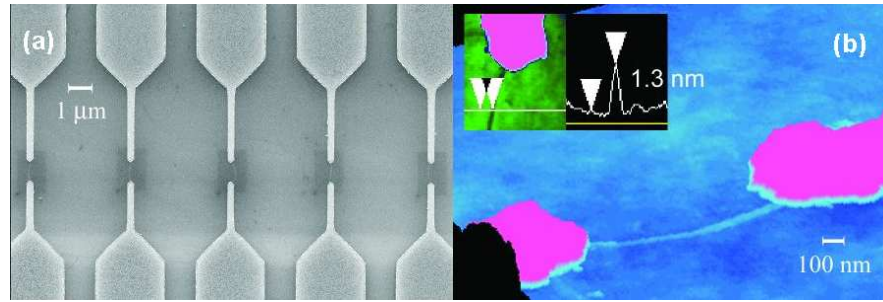


**Figure 4.4:** (a) SEM image of the electrode array showing five adjacent devices with each electrode pair bridged by one carbon nanotube, visible as fine white lines within the dark central areas. (b) AFM image of one single-nanotube device. The height profile confirms the bridging by an individual nanotube. Modified from Ref. [24].

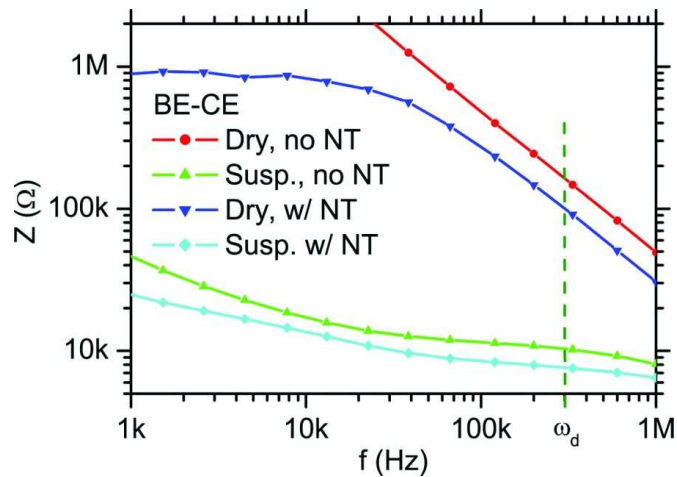


**Figure 4.5:** Impedance spectroscopy measurements between the biased electrode (BE) and a counter electrode (CE). The interpretation is given in the text. Taken from Ref. [24].

Now the self-limiting behavior will be discussed. At first sight the deposition of a nanotube in the gap would appear to ‘short-circuit’ the electrodes, equalizing their potentials and thereby limiting further nanotube deposition. This mechanism, proposed in Reference [12, 22], requires nanotube contact resistances to be low compared to the impedance of the CE/SiO<sub>2</sub>/GE structure and the suspension. Figure 4.5 shows impedance spectroscopy measurements of single tube devices before and after dielectrophoretic nanotube deposition. In the absence of both nanotube and suspension (red curve), the impedance is dominated by the oxide capacitance. After placing a droplet of suspension on the electrode array (green curve), the capacitance of the Helmholtz double layer dominates the impedance at low frequencies, while the ionic conductivity  $\sigma$  of the suspension dominates for high frequencies ( $> 100$  kHz). When there is a nanotube but no suspension (blue

curve), the nanotube contact resistance ( $\sim 1 \text{ M}\Omega$ ) dominates at low frequencies, while the oxide capacitance dominates at high frequencies ( $> 25 \text{ kHz}$ ). When there is a nanotube and suspension (cyan), the impedance is the same as if there was only the suspension, because the impedance of a device (nanotube and its contact resistances) is significantly higher than either the impedance of the suspension or of the CE/SiO<sub>2</sub>/GE structure. Consequentially, the potential difference across the electrodes does not reduce upon nanotube deposition, e. g. the nanotube does not short-circuit the electrodes, and therefore a new explanation for the self-limiting deposition is sought. For this purpose the potential distribution as well as the dielectrophoretic force field were calculated using Finite Element simulations.

### Details of the simulation

As in the work presented in Section 4.1, the three-dimensional experimental device was reduced to a two-dimensional model for the simulation. The device resembles the type *B* electrode structures discussed before and the same argument holds true for the simplification to two dimensions. However, in this work two independent two-dimensional calculations were used to simulate both the potential distribution in the  $x$ - $z$  plane (perpendicular to the sample surface, as before) and the  $x$ - $y$  plane (parallel to the sample surface).

In accordance with the dimensions of the electrode array, the modeled area consists of two round-tipped electrodes in the  $x$ - $y$  (substrate) plane, each  $1 \mu\text{m}$  long and  $100 \text{ nm}$  wide, being  $1 \mu\text{m}$  apart from each other. In the  $z$  direction (perpendicular to the substrate), the simulated area includes the  $40 \text{ nm}$  thick electrodes and  $2 \mu\text{m}$  of surfactant solution ( $\varepsilon = 85\varepsilon_0$ ) above the substrate surface. In the real device the gate electrode is separated from the surface by  $800 \text{ nm}$  of insulating oxide. According to Table 4.1, its influence on the electric field above can be neglected as its thickness is larger than the critical thickness for such effects. The substrate is therefore considered entirely insulating and excluded from the simulation.

In the experiment the AC voltage is applied between the gate electrode and the biased surface electrode. As explained above, due to capacitive coupling the floating counter electrode acquires a potential similar to the gate electrode. Since the gate is not included in the simulation, this effect is imitated by defining the potential  $\Phi$  of the BE and CE as  $\Phi = \pm V_{\text{pp}}/2$ . The absence of free charge carriers and the fact that the double layer does not affect the impedance at the deposition frequency (see Figure 4.5) validates the use of the Laplace equation (2.34) and Dirichlet boundary conditions.

To simulate the situation after deposition, a dielectric rod with  $1 \text{ nm}$  diameter, which represents the nanotube, is centered between the electrode pair. According to theoretical calculations [93, 94] at a nanotube-metal-contact the voltage drops within the first few nanometers of the nanotube adjacent to the metal, due to

a very high contact resistance (1–5 M $\Omega$ ). Comparatively, the resistance of the bulk nanotube ( $h/2e^2 \approx 12.9 \text{ k}\Omega$ ) can be neglected. To account for this in the simulation a small gap of 5 nm is introduced between the ends of the electrodes and the nanotube. The potential of the nanotube is either set to the intermediate potential of the electrode pair, i.e.  $\Phi = 0 \text{ V}$ , or the bulk nanotube is defined as a floating object, i.e. a material with high permittivity whose potential adjusts according to the surrounding local potential. Both approaches yield the same result.

As before, Equation (2.23) is used to calculate the dielectrophoretic force acting on the nanotubes in the suspension. The frequency of  $\omega_d = 300 \text{ kHz}$  however results in a positive Clausius-Mossotti factors for both metallic and semiconducting nanotubes, i.e. both electronic types undergo a positive dielectrophoresis [12, 25]. Therefore,  $\nabla E^2$  is a direct measure of the dielectrophoretic force experienced by the nanotubes both in magnitude and direction.

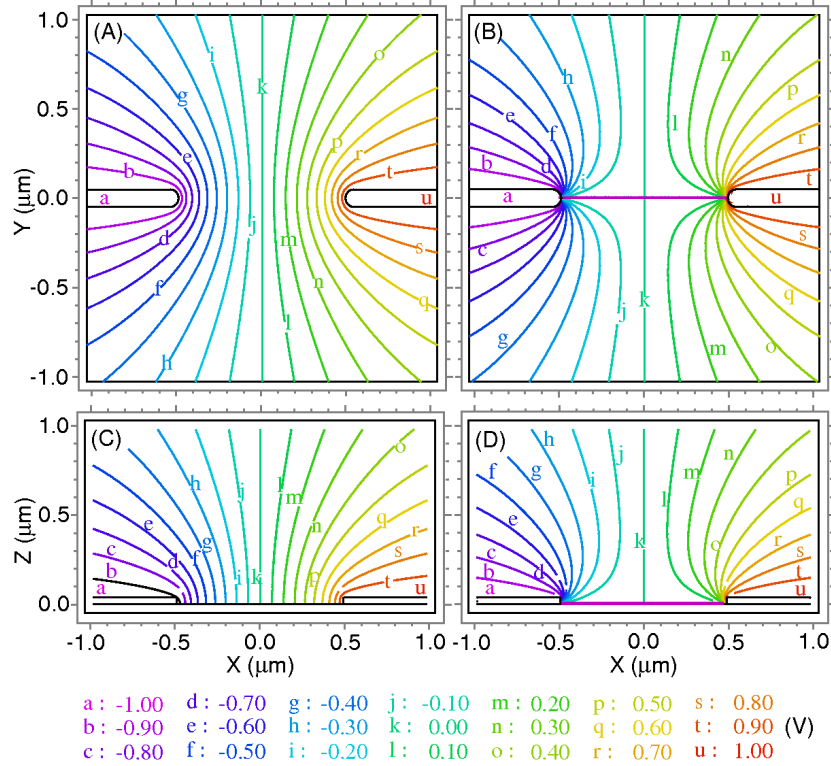
## Results and Interpretation

Figure 4.6 shows the potential distribution ( $\Phi$ ) in the absence (a & c) and presence (b & d) of a nanotube, along two orthogonal planes, one in plane with the substrate surface (a & b) and the other perpendicular to it and along the axis of the electrodes (c & d). In the absence of a nanotube the potential drops uniformly between the electrodes, whereas after the deposition of a nanotube (depicted by the magenta line) the potential drop is restricted to the vicinity of the metal-nanotube contact. In this case the region between the electrodes is almost field free.

In Figure 4.7 the corresponding  $\nabla E^2$  is plotted, which under the experimental conditions is a measure for the dielectrophoretic force acting on the nanotube. The direction of the vector denotes the direction of the force experienced by the nanotube, while the background color quantifies the magnitude. As before, the series (a – d) shows the results in the absence and presence of a nanotube along two different cut planes.

Before any nanotube is deposited, nanotubes experience attractive forces towards the gap at all points, directing a nanotube to deposit between the electrodes. However once a nanotube has been deposited, the dielectrophoretic force-field changes incisively and the region at and around the nanotube develops strong repulsive forces, preventing further nanotube deposition. This change of the dielectrophoretic force field is due to the permittivity of the nanotube surfactant hybrid being much larger than the aqueous solution [25].

For self-limiting single-nanotube deposition, it is critical that only one nanotube at a time enters the central region between the electrode gap. By repeating the assembly experiment using suspensions with various nanotube concentrations, a nanotube concentration of no more than 5 nanotubes/ $\mu\text{m}^3$  for an applied bias



**Figure 4.6:** Simulation of the potential distribution near the electrodes, for two orthogonal cross sections. (a & b)  $\Phi$  at the substrate surface ( $x$ - $y$  plane at  $z = 0$ ); (c & d)  $\Phi$  perpendicular to the substrate ( $x$ - $z$  plane at  $y = 0$ ). The potential drops uniformly between the electrodes in the absence of any deposited nanotubes (a & c) while the potential drop is concentrated around the metal-nanotube contacts, once a nanotube (magenta line) has been deposited (b & d). Taken from Ref. [24].

of  $2.5 \cdot 10^6$  V/m was determined in this setup. In the case of higher nanotube concentration or electric field strength more than one nanotube is attracted and simultaneously deposited in the gap. The small fraction of multiple-nanotube devices observed is attributed to such simultaneous deposition. The control over single-nanotube deposition is most robust with thicker oxides, because for thin oxide the underlying conducting substrate disturbs the electric field on the surface. As such, the mechanism is not restricted to carbon nanotubes and should work equally well with nanowires or any polarizable quasi-one-dimensional object. Moreover, alternative wiring schemes besides capacitive coupling—e. g. direct contact to both electrodes—can also involve this self-limiting deposition.

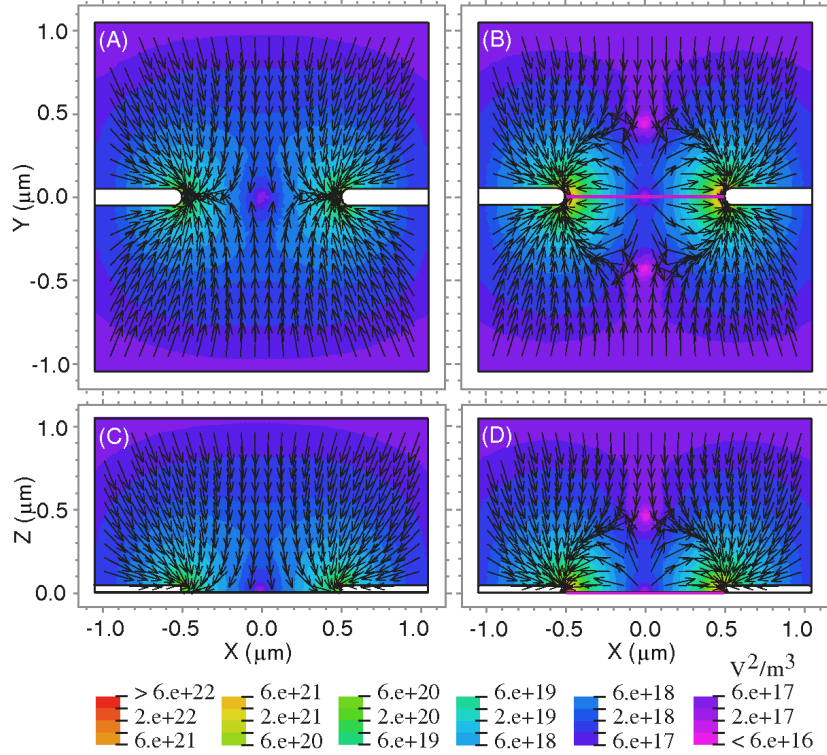


**Figure 4.7:** Simulation of dielectrophoretic force fields near the electrodes. (a & b)  $\nabla E^2$  at the surface of the substrate ( $x$ - $y$  plane at  $z = 0$ ); (c & d)  $\nabla E^2$  perpendicular to the substrate ( $x$ - $z$  plane at  $y = 0$ ). The arrows indicate the direction of the force acting on a dispersed nanotube, while the background color is the magnitude of  $\nabla E^2$ . The dielectrophoretic force is attractive in all regions in the absence of deposited nanotubes (a & c), but it becomes repulsive between the electrodes, once a nanotube (magenta line) has been deposited (b & d). Taken from Ref. [24].

### 4.3. Influence of structural and dielectric anisotropy on the dielectrophoresis of single-walled carbon nanotubes

#### Motivation

According to the advanced model of nanotube dielectrophoresis discussed in Section 3.2, within a certain frequency range,  $f_1^{\text{TO}} \dots f_{c,\perp}$ , a deposition of semiconducting nanotubes can occur due to their perpendicular polarizability, but should only be observable in experiments at very large electric fields. In earlier experiments under moderate fields ( $E_{\text{pp}} = 20 \text{ V}/20 \mu\text{m}$ ) semiconducting SWNTs were not deposited above the critical frequency  $f_c \sim 3 \text{ MHz}$  [11, 25]. In a recent experiment at larger fields ( $10 \text{ V}/2 \mu\text{m}$ ) a cross over frequency of  $f_c \sim 30 \text{ MHz}$  was observed [26]. Finally, the work presented in Chapter 3 shows that at very

large electric fields ( $40 \text{ V}/2 \mu\text{m}$ )  $f_c > 80 \text{ MHz}$  (see Figures B.4 – B.7). This agrees with the model that at moderate fields the probed critical frequency is due to the parallel polarizability  $\alpha_{\parallel}$ , whereas at larger fields and frequencies it is the orthogonal polarizability  $\alpha_{\perp}$  that progressively dominates the dielectrophoresis. In the following this situation will be visualized by the use of numerical field simulations.

### Details of the simulation

The array of interdigitated electrodes used in the experiments consists of 140 electrode fingers with a length of  $\sim 360 \mu\text{m}$  and a width of  $1.8 \mu\text{m}$  each, separated by  $1.8 \mu\text{m}$  wide gaps. The thickness of the Al layer is  $145 \text{ nm}$  and that of the quartz glass is  $0.5 \text{ mm}$ . As in the case of the type *A* structures of Section 4.2, the three-dimensional problem can be reduced to a two-dimensional one which is defined in the  $x$ - $z$  plane.

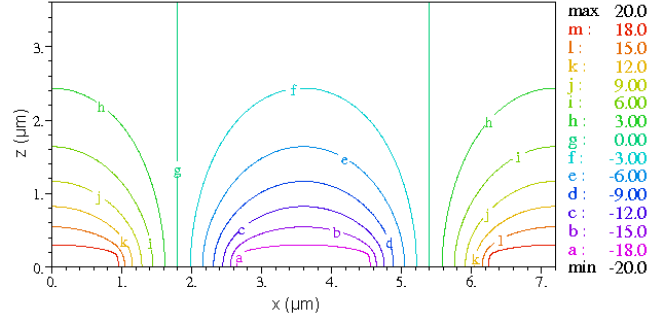


**Figure 4.8:** Potential distribution in the unit cell representing the interdigitated electrode array

For the simulation a representative section was chosen extending from the center of a positively charged electrode to the center of the next positively charged electrode. This ‘unit cell’ then contains two electrodes and two gaps situated above a  $50 \mu\text{m}$  thick quartz substrate with permittivity  $\varepsilon = 5\varepsilon_0$  and underneath a  $50 \mu\text{m}$  thick aqueous layer with  $\varepsilon = 85\varepsilon_0$ . The potential of the electrodes is defined by a Dirichlet condition to  $\Phi = \pm V_{\text{pp}}/2 = \pm 20 \text{ V}$  and to the sidewalls Neumann boundary conditions  $\partial\Phi/\partial n = 0$  are assigned. Figure 4.8 shows the resulting potential distribution in the unit cell obtained by solving the Laplace equation (2.34).

By expansion of Equation (2.17) using Equation (3.2) for rod-shaped particles the dielectrophoretic force within the particle’s coordinate system is derived as

$$\vec{F}_{\text{DEP}} = \frac{1}{2} \nabla \left( \alpha_{\parallel} \vec{E}_{\parallel}^2 + \alpha_{\perp} \vec{E}_{\perp}^2 \right). \quad (4.1)$$

As a means of simplification a fixed orientation of the nanotubes with respect to the global coordinate system is assumed. It is then easy to transform Equation

(4.1) from the particle's coordinate system into the global coordinate system: for horizontally aligned nanotubes  $\vec{F}_{\text{DEP}} = \frac{1}{2}\nabla(\alpha_{\parallel}E_x^2 + \alpha_{\perp}E_z^2)$  is derived and for vertically aligned nanotubes  $\vec{F}_{\text{DEP}} = \frac{1}{2}\nabla(\alpha_{\parallel}E_z^2 + \alpha_{\perp}E_x^2)$ . The calculations are based on the structural and dielectric properties of single-walled carbon nanotubes as specified in Chapter 3.

## Results and discussion

Figure 4.9 shows the simulated dielectric force fields acting on metallic (a & b) and semiconducting nanotubes (c & d) assuming horizontal or vertical alignment of the nanotubes as indicated. A representative frequency of 50 MHz was chosen such that  $\alpha_{\parallel}^{\text{met}}, \alpha_{\perp}^{\text{met}} > 0$  and  $\alpha_{\parallel}^{\text{semi}} < 0$ .

Note that under the experimental conditions metallic nanotubes are well aligned along the electric field lines, as shown in Figure 3.10(a). Since the electric field lines are horizontal above the gap, Figure 4.9(a) applies to metallic nanotubes in this region, whereas Figure 4.9(b) applies to metallic nanotubes above the electrode, where the field lines are vertical. Therefore metallic nanotubes always experience an attractive force towards the substrate.

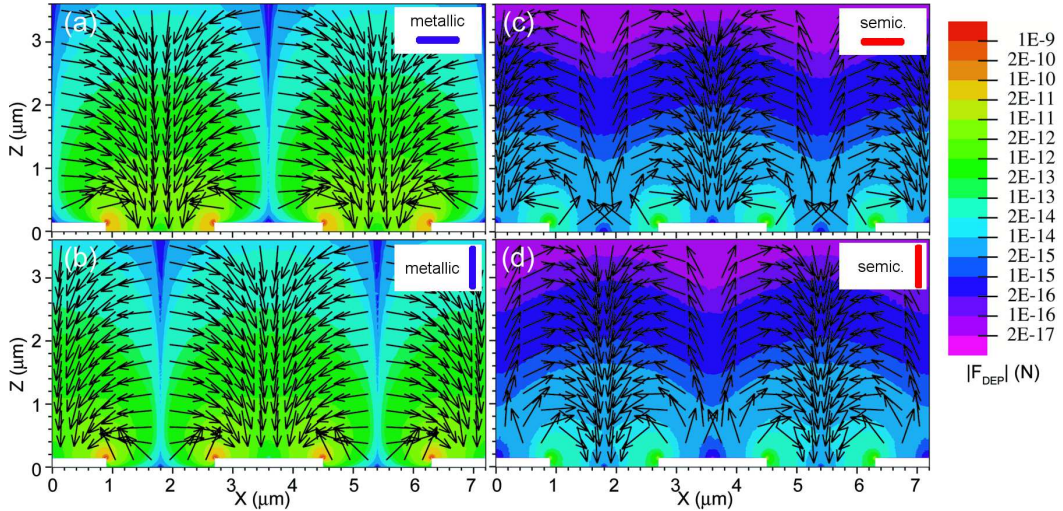


**Figure 4.9:** Simulation of the dielectrophoretic force fields. (a & b)  $\vec{F}_{\text{DEP}}$  for metallic nanotubes and (c & d)  $\vec{F}_{\text{DEP}}$  for semiconducting nanotubes, assuming the nanotubes to be horizontally aligned or vertically aligned as indicated. While metallic nanotubes are attracted towards the substrate surface, semiconducting nanotubes experience either attractive or repulsive forces depending on their orientation with respect to the electric field.

The orientation of semiconducting nanotubes on the other hand is random under the chosen conditions (see Figure 3.10(b)). Comparing the two representative situations of horizontal and vertical alignment, a significant change in the force

fields is observable. A closer look at Figure 4.9(c) reveals that the forces are repulsive in regions where the nanotubes are parallel to the electric field (above the gaps), while they are attractive when the nanotubes are orthogonal to the electric field (above the electrodes). The same, of course, holds true for Figure 4.9(d).

These simulations clearly show that semiconducting nanotubes can be attracted to the substrate surface due to their orthogonal polarizability, albeit the magnitude of the force is smaller than in the case of the metallic nanotubes. With respect to the measured random orientation of semiconducting nanotubes in the gap (see Figure 3.8), it is apparent that the dielectrophoretic force field simulations predict repulsion only for semiconducting nanotubes which are oriented along the  $x$ -axis. Nanotubes oriented along the  $y$ -axis and  $z$ -axis are attracted, which should result in a depletion of semiconducting nanotubes close to  $\gamma = 0$ . However, considering the drag coefficient of nanotubes, which depends on the angle between the nanotube axis and the direction of motion [95], the highest deposition rate is expected for vertically oriented semiconducting nanotubes, which upon touching the surface flip over without preferential direction.

#### 4.4. Electrostatic modeling of nanotube devices with floating electrodes for voltage-contrast SEM

As stated before, single-walled carbon nanotubes have tremendous potential as interconnects and field-effect transistors (FETs) in nano-electronics. Besides the need for precise assembly and contacting of nanotubes, an increasing demand for rapid, non-invasive electrical characterization techniques of nanotube devices becomes apparent. The techniques currently available—like direct electron transport measurements and indirect characterization such as Raman spectroscopy [54], near-field optical microscopy [96], scanning tunneling spectroscopy [97] and microscopy [40] and electron diffraction [98]—are slow and sequential and possess only limited applicability to the process flow for nanotube device fabrication and integration. Recently, voltage-contrast scanning electron microscopy (VC-SEM) was proposed as an effective metrology tool for the rapid characterization of the electronic nature of SWNTs and other molecular nanostructures in functional device geometries [99]. It involves tuning the electronic band structure and imaging the potential profiles along the length of the nanotube. The results can be explained by finite element simulations of device electrostatics, taking into account the change in dielectric properties of the nanotube under the influence of a gate electric field.

## Motivation

High-density arrays of single nanotube devices consisting of one independent floating electrode (source), one common electrode (drain) and the highly-doped Si/SiO<sub>2</sub> substrate as a common back-gate (as illustrated in Figure 4.3) were characterized by VC-SEM. Figure 4.10 shows VC-SEM images of a representative region of the electrode array, imaged at two illustrative gate voltages ( $V_G = +20$  V and  $-10$  V). The devices were maintained at equilibrium condition with the drain grounded ( $V_D = 0$ ) and source unconnected ( $V_S$  floating), while  $V_G$  was swept between 0 and  $\pm 20$  V. The source electrodes in devices 2, 4, 7 and 8 show identical contrast to the drain for all gate voltages, indicating that potential between the source and drain equilibrates instantaneously through the bridging nanotube. These nanotube devices are metallic. While at low  $V_G$  the contrast of source electrodes of devices 1, 3, 6 and 9 lags significantly to the drain contrast, implying that the potential does not equilibrate between the source and drain via the bridging nanotube, the devices behave similar to metallic devices at high  $V_G$ . These are semiconducting nanotube devices (FETs). Devices 5 and 10, whose source electrodes do not change their contrast with applied bias, reveal defective contacts under closer observation. Measurements of the electron transport characteristics of the three-terminal devices confirm that the contrast of the floating electrode, which can be rapidly imaged at low resolution, correlates with the electronic property of the corresponding nanotube device.

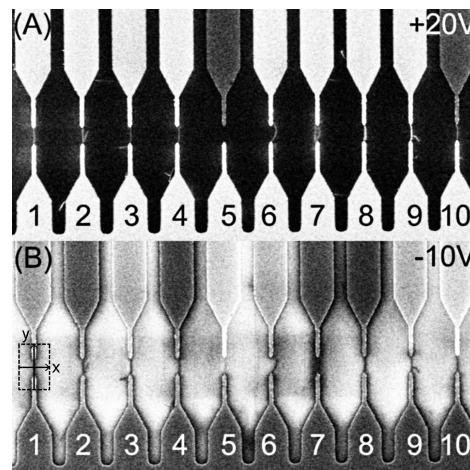


**Figure 4.10:** VC-SEM images of 10 adjacent SWNT devices at a back-gate bias  $V_G$ . (a)  $V_G = +20$  V. Bright contrast indicates enhanced SE emission. (b)  $V_G = -10$  V. Dark contrast indicates suppressed SE emission. The common drain (bottom electrode) is grounded and the independent sources (top electrodes) are floating. Devices 2, 4, 7, 8 are metallic; devices 1, 3, 6 and 9 are semiconducting. The extension of the unit cell used for the simulation and the orientation of the  $x$ - and  $y$ -axes is indicated in (b); the  $z$ -axis points out of the drawing plane. Modified from Ref. [99].

SEM is based on the detection of secondary electrons (SEs) generated when primary or backscattered electrons interact with the sample [100]. SEs have low energy ( $\leq 50$  eV) compared to the incident beam (1–30 keV) and only those originating in a few nanometer depth from the surface can escape and be detected. When the surface has a negative potential (negative  $V_G$ ), the SE emission yield is enhanced while a positive potential (positive  $V_G$ ) effectively retains the SEs and reduces their yield [101]. Any potential on a SWNT will influence SE image contrast both due to changes in the SE yield and the deflection of SEs emitted from the substrate in the nanotube's vicinity [100, 102]. Therefore a qualitative understanding of the SE contrast can be obtained from the surface potential and electric field distribution around the nanotube and associated electrodes.

### Details of the simulation

In a first step, the electric potential near a floating or grounded electrode in the absence of a nanotube is calculated in a three dimensional simulation to explain the contrast evolution of the electrodes. The modeled volume consists of an individual metal electrode ( $\varepsilon = 10^8 \varepsilon_0$ ) with a length of  $1 \mu\text{m}$ , a width of  $200 \text{ nm}$  and a height of  $50 \text{ nm}$ . The electrode is situated in the center of the  $x$ - $y$ -plane of  $20 \times 4 \mu\text{m}^2$  size. In the  $z$  direction the electrode is separated from the gate electrode at the bottom by an  $800 \text{ nm}$  thick oxide layer ( $\varepsilon = 3.9 \varepsilon_0$ ) and from the top electrode by  $10 \mu\text{m}$  of air ( $\varepsilon = \varepsilon_0$ ). A schematic of the simulation model is shown in Figure 4.11(a). The potential  $\Phi$  on the bottom and top surface were set to  $V_G$  and  $0 \text{ V}$  respectively (Dirichlet condition). Neumann boundary conditions,  $\partial\Phi/\partial n = 0$ , were assigned to the sidewalls of the simulation space as well as to internal material interfaces. To model the situation for a grounded electrode, the potential of the electrode was also fixed by a Dirichlet condition to  $0 \text{ V}$ . In the case of the floating electrode, no potential is specified. Due to the large dielectric constant of the metal, the potential of the electrode then adjusts to a constant value within the electrode [103].

In the next step the transition of a semiconducting nanotube from the OFF into the ON state and its influence on the VC-SEM image will be discussed. After depositing a nanotube between a biased electrode and an electrically floating counter electrode, this constitutes a three-terminal device with the biased electrode acting as drain, the floating electrode forming the source and the underlying silicon substrate the gate. Application of a potential difference between gate and drain then leads to an asymmetric potential profile along the nanotube which affects the local charge distribution on the nanotube which in turn alters the local potential. The final potential distribution is electronic type specific and results in the distinct contrast profile monitored by VC-SEM.

The central element of the three dimensional SWNT device model, illustrated in Figure 4.11(b), is a carbon nanotube with a length of  $1 \mu\text{m}$  and a radius of

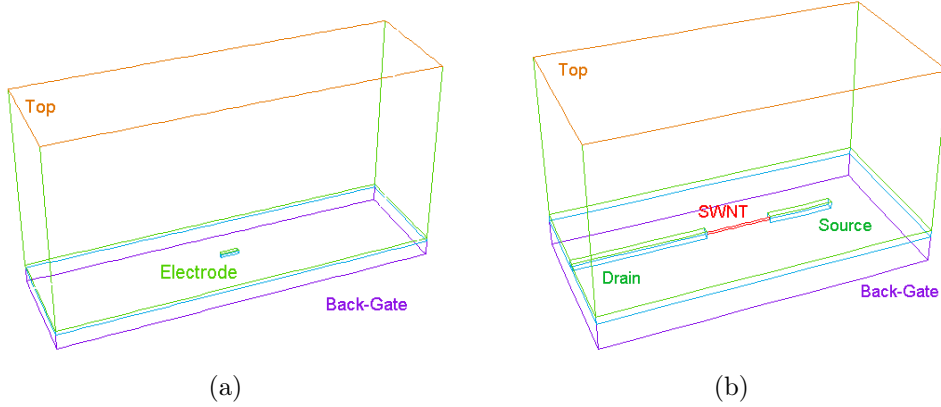


**Figure 4.11:** Model for the floating vs. grounded electrode simulation (a) and for the SWNT device simulation (b). The dimensions are not to scale.

0.63 nm centered between two metal electrodes. Both electrodes have a width of 200 nm and a height of 50 nm. The first electrode is  $2 \mu\text{m}$  long and its potential is set to 0 V (grounded electrode). The other electrode is  $1 \mu\text{m}$  long and electrically floating. The full extension of the  $x$ - $y$ -plane is  $5 \cdot 2 \mu\text{m}^2$ . As before, the electrodes are situated on the substrate surface which is separated from the gate electrode ( $\Phi = V_G$ ) by an 800 nm thick oxide and from the top electrode ( $\Phi = 0 \text{ V}$ ) by  $5 \mu\text{m}$  of air. The dielectric constants used in this model are  $\varepsilon = 10^8 \varepsilon_0$  for the metal electrodes,  $\varepsilon = 3.9 \varepsilon_0$  for the oxide and  $\varepsilon = \varepsilon_0$  for air.

Due to the presence of a electrostatic potential, charge carriers are induced on the semiconducting nanotube. A self-consistent simulation based on the Poisson equation,  $\nabla(\varepsilon \nabla \Phi) = \rho$ , accounts for the influence of the local charge carrier density on the potential distribution in the vicinity of the nanotube [104]. Here  $\rho$  is the density of free charge carriers. This approach does not reproduce the evolution of the floating electrode potential, in particular the equilibration of the floating source and grounded drain electrode potentials at high  $V_G$  as observed in the experiment.

Agreement with experimental observations is only obtained when a variation in the permittivity of a semiconducting SWNT under the influence of gate bias is considered. While this approach has not been used in any previous experimental or theoretical work, the assumption of such a dependence is reasonable since the permittivity  $\varepsilon$  of a semiconducting nanotube depends on its band-gap  $\Delta E$  ( $\varepsilon \propto \Delta E^{-2}$ ) and diverges for metallic nanotubes ( $\Delta E = 0$ ) (see Section 2.1.2 and References [42, 43]). As the semiconducting nanotube switches to metallic behavior under the influence of  $V_G$ , its  $\varepsilon$  should also increase and diverge. This is accounted for by solving the Laplace equation (2.34) with  $\varepsilon$  ranging from  $30 \varepsilon_0$  for a semiconducting nanotube at  $V_G = 0$  to  $10^8 \varepsilon_0$  for a semiconducting nanotube at high  $V_G$  or a metallic nanotube [43]. Intermediate values of  $\varepsilon$  represent qual-

itatively the transition of a semiconducting nanotube from the OFF to the ON state.

## Results and discussion

First the results of the potential distribution for an individual electrode which is either grounded or electrically floating are reviewed. Figure 4.12 shows a cross section perpendicular to the substrate surface. Plotted are the equipotential lines and electric field distribution around the surface electrodes for  $V_G = \pm 5$  V obtained by solving the Laplace equation (2.34). The two graphs at the top illustrate the results for a floating electrode arrangement, while those at the bottom show the situation for a grounded electrode.

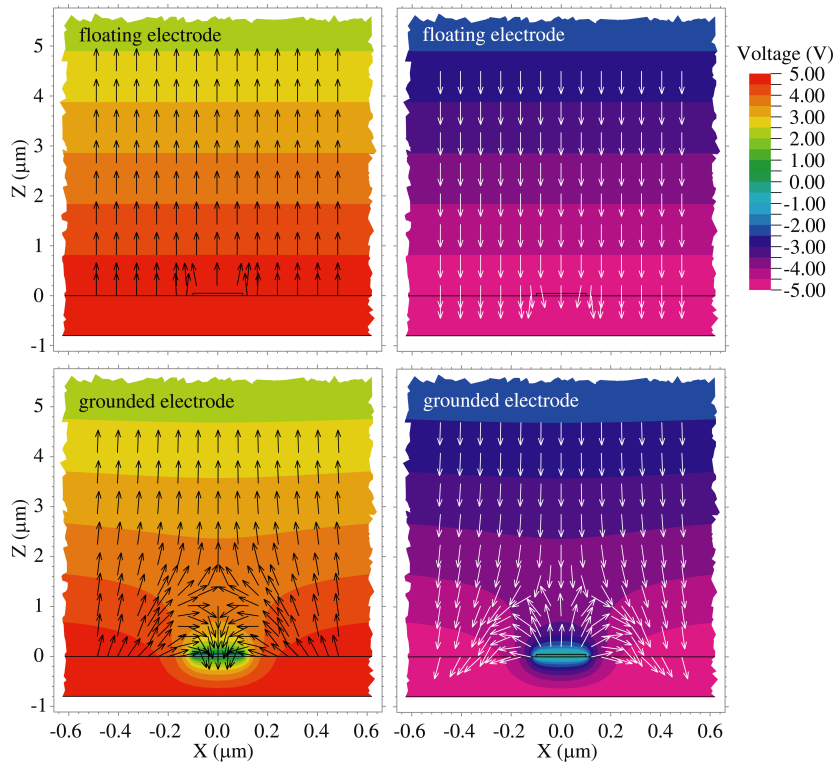


**Figure 4.12:** Potential  $\Phi$  (background color) and electric field  $\vec{E}$  (arrows) distribution near floating and grounded surface electrodes (seen in cross section). Floating electrodes acquire a potential similar to that of the substrate and do not significantly distort the electric field distribution. Grounded electrodes are at a different potential compared to the substrate and cause large distortion in the electric field distribution. A region around the electrodes is also affected due to the field distortion. From Ref. [99].

Floating electrodes acquire a potential similar to that of the substrate and do not significantly distort the electric field distribution. Grounded electrodes are at a different potential compared to the substrate and cause large distortion in the

electric field distribution. A floating electrode therefore shows a contrast similar to that of the substrate surface, while the grounded electrode appears brighter or darker than the substrate surface depending on the polarity  $V_G$ . The drain is always grounded, so sources that are connected to the drain by a conducting nanotube are also grounded and show similar contrast to the drain, while sources that are connected by poorly conducting nanotubes are floating and show contrast similar to the surface.

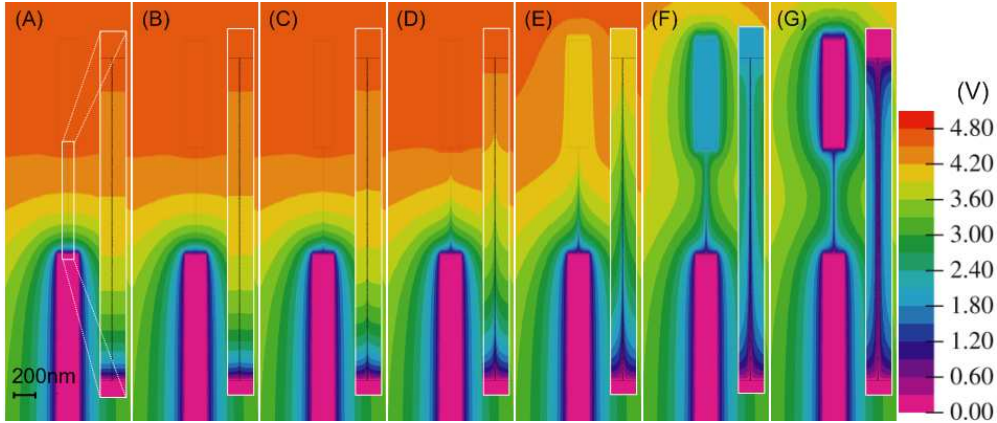


**Figure 4.13:** Evolution of the electrostatic potential  $\Phi$  as a function of the dielectric constant  $\varepsilon$  of the bridging nanotube. (a – g)  $\varepsilon = 30, 10^3, 10^4, 10^5, 10^6, 10^7, 10^8\varepsilon_0$ . Insets show the magnified region around the nanotube and the potential profile along the nanotube. The simulations were performed at  $V_G = 5\text{ V}$ ,  $V_D = 0\text{ V}$ ,  $V_S$  is floating. (a) ( $\varepsilon = 30\varepsilon_0$ ) corresponds to a semiconducting nanotube at low gate bias, completely in its OFF state.  $V_S$  is determined by the electrostatic coupling to the gate. (g) ( $\varepsilon = 10^8\varepsilon_0$ ) corresponds to either a semiconducting nanotube at high gate bias (ON-state) or a metallic nanotube (which has a diverging  $\varepsilon$ ).  $V_S$  is determined by  $V_D$ . (b – f) Intermediate values of  $\varepsilon$  represent the transition from OFF to ON state of the semiconducting nanotube under increasing gate bias. From Ref. [99].

Now the results obtained for the SWNT device are discussed. Figure 4.13 shows the calculated potential distribution in the vicinity of the nanotube and surface electrodes for different nanotube permittivity. While the simulations were performed at  $V_G = 5\text{ V}$ , the potential distributions scale proportionally for other values of  $V_G$ . When a semiconducting SWNT is insulating, the potential of the floating electrode is determined by its electrostatic coupling to the gate. In this case, the contrast of the floating electrode is similar to the substrate. As the nanotube becomes more polarizable, it exerts an increasing influence on the potential of the floating electrode and its contrast starts to increasingly deviate from the substrate. When a semiconducting nanotube is in its ON state, or for a metallic nanotube, the potential of the floating electrode is almost entirely coupled to that of the drain electrode (ground) through the highly polarizable SWNT, and its contrast is similar to that of the drain and distinct from the substrate. The nanotube too, has the same potential as the electrodes (and hence uniform con-

trast) along its length. For intermediate nanotube permittivity, the potential and contrast along the nanotube decrease from the drain to the source.

A comparison of the contrast profiles observed in the experiment and simulated potential profiles shows a good qualitative agreement [99]. Quantitative differences can be explained by the fact that the permittivity  $\varepsilon$  is assumed to be constant along the length of the nanotube in the simulations. In reality  $\varepsilon$  varies with the local potential and could significantly deviate close to the contacts, where the local potential changes rapidly [104]. However, until a quantitative relationship between  $\varepsilon$  and  $V_G$  is established, the approach described above yields the best simulation of the experimental situation.

## 5. Field-dependent absorption spectra of dispersed single-walled carbon nanotubes

According to the advanced model for nanotube dielectrophoresis introduced in Section 3.2, the alignment of dispersed metallic and semiconducting nanotubes under the influence of external electric fields differs significantly. Monitoring the degree of alignment under variation of the field strength  $E_{pp}$  and the frequency  $f$  allows to determine the dielectric properties of the single-walled carbon nanotubes under examination. The knowledge of the dielectric properties and derivated parameters—like the critical frequency and critical field strength for various surfactants—would significantly facilitate the optimization of further experiments regarding the dielectrophoresis of carbon nanotubes.

One method to analyze the alignment is to measure in situ the optical absorbance of a nanotube suspension subjected to an electric field. The relative change in the absorbance features originating from the two nanotube species with the external field parameters would be a measure for the electronic-type-specific nanotube alignment, which is predicted in Figure 3.10. A similar experiment was reported in Reference [105]. There, linear polarized laser light passed through a cuvette which contains SWNTs suspended in ethanol. An AC electric field of frequency  $f = 4$  kHz and oriented perpendicular to the light path was applied to the suspension. An analyzer, which is rotated  $90^\circ$  with respect to the polarizer, allows to detect small changes in the polarization state of the laser beam which results in an increased signal detected at the photodiode. The authors report a field-dependent increase of the signal, which saturates for electric fields of the order of  $10^5$  V/m. According to their interpretation the observed effect is due to an alignment of the dispersed carbon nanotubes. However, since the experimental setup allows only to detect wavelength-independent changes of the initial polarization it cannot be ruled out that the optical anisotropy is caused by other particles present in the solution, in particular since ethanol is not suitable to produce stable suspensions of individual carbon nanotubes. In the following an experimental setup and first results are presented of an investigation of the electronic-type-specific alignment of surfactant-stabilized carbon nanotubes exposed to AC electric fields.

## 5.1. Experimental setup

The setup used in this experiment is illustrated in Figure 5.1. The light source is a Micropack DH-2000-BAL Balanced Deuterium Tungsten Halogen Light Source, which emits in the spectral range from 250 nm to 1200 nm, i. e. covering the M1 and the S2 peaks. As detector an Ocean Optics HR4000 High-resolution Spectrometer is used. Unlike in Reference [105], the experiment is carried out with non-polarized light and the external electric field is in parallel with the light path. In the case of random nanotube orientation this results in a maximum value of absorption, which decreases with an increasing alignment of the nanotubes.

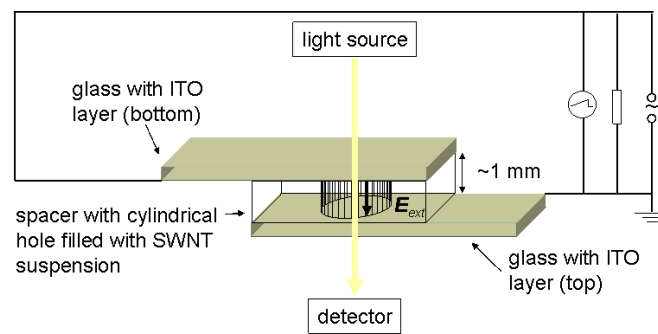


**Figure 5.1:** Schematic of the experimental setup to measure the alignment of dispersed SWNTs in electric fields. Transparent ITO/glass electrodes connected to a voltage source are used to generate the external electric field. Non-polarized light traverses the nanotube suspension parallel to the electric field. Nanotubes that are aligned parallel to the field do not contribute to the total absorbance.

To create the electric field, two glass slides—each of them covered on one side with transparent and conductive indium tin oxide (ITO) layers and an optional protective coating made of polymethylmethacrylate (PMMA)<sup>1</sup>—are connected to a voltage source with a  $50\ \Omega$  resistor in parallel. As in the experiment described in Section 3.1, two Agilent 33250A Function/Arbitrary Waveform Generator and an Empower RF Systems High Power RF Amplifier are used to generate a pulsed AC signal.

The ITO/glass electrodes are separated from each other by an insulating spacer made of poly(dimethylsiloxane), PDMS<sup>2</sup> containing a cylindrical hole, into which the nanotube suspension is filled. According to Figure 3.10, large field strength

<sup>1</sup>In some cases an increased surface roughness was observed after the experiment, which was interpreted as a degradation of the ITO layer. To prevent this, the ITO was coated with PMMA. The results of the absorbance measurements do not depend on the presence of the PMMA coating.

<sup>2</sup>The use of PDMS as spacer allows to make use of the adhesion forces between the PDMS and the ITO/glass slides to seal the test volume [106].

are necessary to induce a significant degree of alignment of the nanotubes. Consequently the distance between the electrodes should be as small as possible. Due to practical reasons, a distance of  $\sim 1$  mm was chosen here. Since the absorbance  $Abs$  follows the Lambert-Beer law

$$Abs = \epsilon \cdot c \cdot l, \quad (5.1)$$

where  $\epsilon$  is the extinction coefficient,  $c$  is the concentration and  $l$  is the path length, this implies the need for highly concentrated nanotube suspensions.<sup>3</sup> Therefore a suspension prepared using density gradient centrifugation was used in this experiment (Suspension #6, see Figure A.3).

The experiments are conducted in the following way: First, the test volume is filled with pure surfactant solution and the absorbance is measured as reference spectrum. Next, the nanotube suspension is inserted and the impedance spectrum is measured with an Agilent 4294A Precision Impedance Analyzer. A typical spectrum is presented in Figure 5.2. For low frequencies the capacitance emerging from the boundary between the electrodes and the liquid is the dominant contribution to the total impedance. If the ITO/glass electrodes are covered with an additional PMMA coating of  $\sim 180$  nm thickness, this capacitance decreases by two orders of magnitude: Without the PMMA coating, the extension of the double layer, characterized by the Debye length  $\kappa^{-1}$  (see Section E), defines the capacitance. The Debye length is of the order a few nm for aqueous solutions [71], i. e. it is two orders of magnitude smaller than the PMMA thickness. When the two capacitances are connected in series, the contribution of the PMMA layer determines the total impedance, which in effect increases by two orders of magnitude. In the mid-frequency range the ohmic conduction prevails and for high frequencies the capacitance of the wiring dominates. If, during the filling procedure, air bubbles are embedded into the test volume this prohibits an ohmic contact between the liquid and the ITO/glass electrodes. In this case the plateau with  $\theta \approx 0^\circ$  is absent in the measurement and the test volume is refilled to ensure the reproducibility of the experiment.

Now the test volume is inserted in the light path and connected to the voltage source. A pulsed AC voltage with a typical pulse duration  $t_{ON} = 1$  ms and period  $\tau = 10$  ms is applied for  $t = 1$  min. The frequency  $f$  and the voltage  $V_{pp}$  are varied in each experiment; typical ranges are  $f = 1$ –80 MHz and  $V_{pp} = 10$ –250 V. The absorbance  $Abs(V_{pp})$  is measured immediately before the voltage is turned off. The system is then allowed to relax for  $t = 1$  min, before the voltage is turned back on. Again, an absorbance spectrum  $Abs(0)$  is measured at the very end of the relaxation time to verify the recovery of the initial state. The experiment is disregarded when irreversible changes in the absorbance are observed.

---

<sup>3</sup>Typical absorbance spectra as presented in Figure 2.13 were obtained using an optical path length of 1 cm.

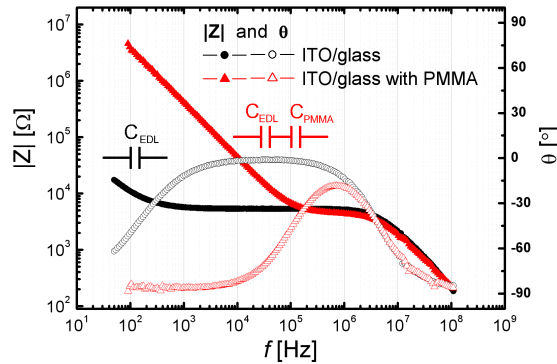


**Figure 5.2:** Impedance spectrum of the test volume filled with nanotube suspension (Suspension #6). The plateau with  $\theta \approx 0^\circ$  is indicative of an ohmic conduction through the suspension. In the presence of a PMMA coating of the ITO/glass electrodes, the total capacitance due to the liquid–electrode boundary, which dominates in the low-frequency regime and contains contributions of the electronic double layer and the PMMA, decreases by two orders of magnitude.

## 5.2. Results and discussion

The experiment described above was repeated several times under similar conditions. In each individual experiment the AC voltage  $V_{pp}$ —measured with an oscilloscope at the test volume—was varied while keeping the frequency  $f$  fixed or vice versa, to map the entire parameter space that is accessible with the chosen setup. The maximum frequency was set to  $f = 80$  MHz due to the specifications of the frequency generator. The maximum voltage is defined by the performance of the amplifier, which has a maximum power of 100 W. Due to probably imperfect impedance matching in the experimental setup<sup>4</sup>, the maximum voltage depends on the frequency and varies between 200 V and 350 V. The application of high voltages can lead to an irreversible change in the absorbance spectrum (see Figure D.1). To avoid these irreversibilities the applied voltage was generally not increased above 250 V.

When a voltage  $V_{pp}$  is applied to the test volume containing dispersed nanotubes, the absorbance decreases as compared to the spectrum measured with  $V_{pp} = 0$ . This is illustrated in Figure 5.3, where absorbance spectra with and without electric field are presented. A closer look at Figure 5.3(a) reveals that the absorbance due to single-walled carbon nanotubes decreases with increasing voltage. This indicates an increasing alignment of the nanotubes, which agrees with the predicted behavior. However, a difference in the alignment of metallic and semiconducting is not apparent in these measurements.

To allow for a quantitative analysis of the data, the change of the absorbance as a function of applied voltage and frequency needs to be extracted from the raw

<sup>4</sup>The wiring is made of unshielded Cu cables instead of BNC cables.

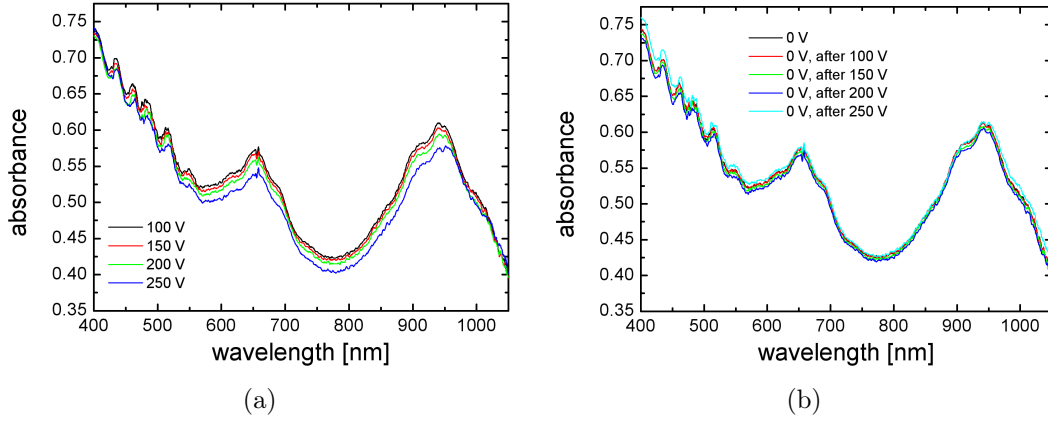


**Figure 5.3:** Absorbance spectra of dispersed nanotubes after application of an AC voltage  $V_{pp}$  according to the key with a frequency  $f = 70$  MHz for  $t = 1$  min (a) and after a relaxation with  $V_{pp} = 0$  for  $t = 1$  min (b). In the presence of the electric field the absorbance decreases; this decrease appears to be most pronounced near the maxima of the M1 and S2 bands. After turning off the voltage, the system relaxes into its original state.

data. For this purpose the ‘relative absorbance’ is defined as  $Abs(V_{pp})/Abs(0)$ .<sup>5</sup> Figure 5.4 shows this value for the same experiment already presented in Figure 5.3. Both the wavelength dependence of the relative absorbance and the increase of its magnitude with the applied AC voltage are clearly observable. In particular, the absorbance changes most significantly at the M1 and S2 bands, but a difference between the two electronic types is not noticeable in this representation.

Using Equations (3.7) and (3.10) it can be shown (see Appendix D) that for small  $|U_0|/k_B T$  the relative absorbance depends on the applied voltage as

$$\frac{Abs(V_{pp})}{Abs(0)} = \frac{1 + \frac{c_1}{5} V_{pp}^2}{1 + \frac{c_1}{2} V_{pp}^2}, \quad (5.2)$$

with constant  $c_1 > 0$ . In Figure 5.3  $Abs(V_{pp})/Abs(0)|_\lambda$  is displayed for two frequencies  $\lambda = 650$  nm (center of the M1 band) and  $\lambda = 950$  nm (center of the S2 band). The results of a fit according to Equation (5.2) are shown in Table 5.1.

This analysis clearly confirms that the absorbance and therefore the alignment of the dispersed single-walled carbon nanotubes changes as a function of the applied electric field and the frequency. As expected, the absorbance decreases with increasing  $V_{pp}$ . A fit according to Equation (5.2) shows good agreement with the measured data (see Figures D.2–D.5). However, the values obtained for  $c_1$  are very small and do not reveal any systematics.

<sup>5</sup>Since  $Abs(0)$  is measured before each voltage step, the most recently measured value is always used as reference.

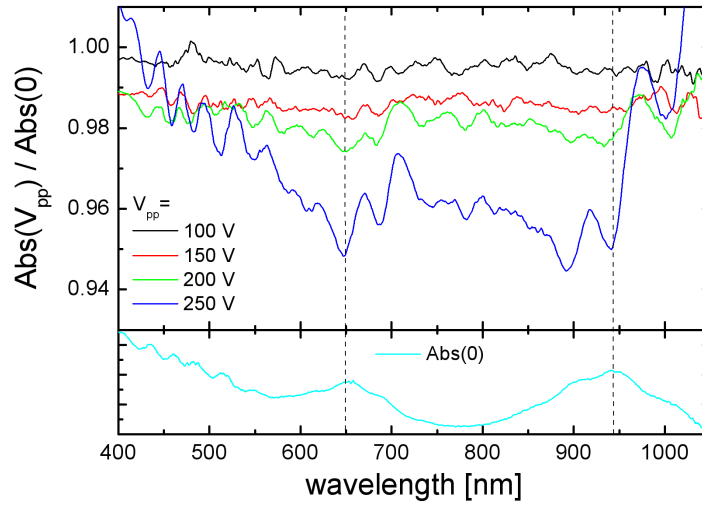


**Figure 5.4:** Field-dependent changes of the nanotube absorbance. The relative absorbance  $Abs(V_{pp})/Abs(0)$  for a frequency  $f = 70$  MHz is presented in the top graph, while the lower graph shows the absorbance spectrum in the absence of an electric field for comparison. The absorbance decreases in the presence of an electric field, resulting in a relative absorbance  $< 1$ . The magnitude of the relative absorbance increases with increasing AC voltage  $V_{pp}$  and exhibits a clear wavelength dependence—the absorbance reduces mainly at the M1 and S2 bands. This indicates an increasing alignment of both semiconducting and metallic nanotubes.

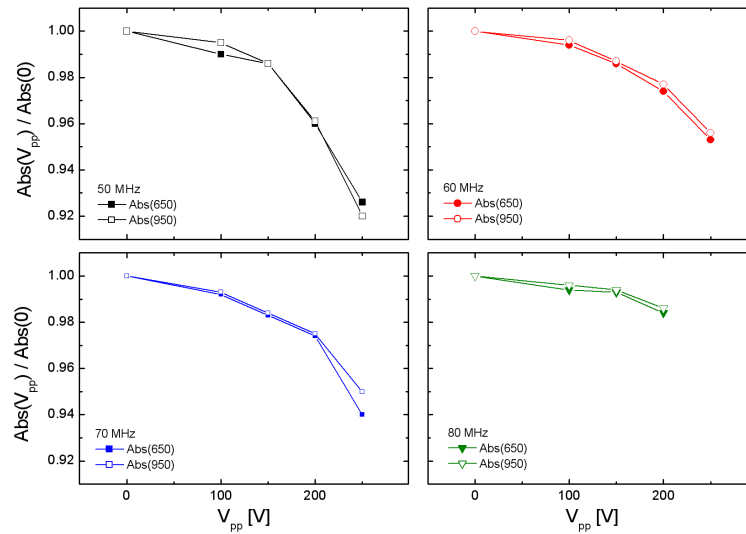


**Figure 5.5:** Evolution of the relative absorbance with applied voltage for a series of frequencies  $f = 50$ – $80$  MHz. Plotted is  $Abs(V_{pp})/Abs(0)|_{\lambda}$  for  $\lambda = 650$  nm (full symbols, representing metallic nanotubes) and  $\lambda = 950$  nm (open symbols, representing semiconducting nanotubes). A similar dependency of the applied voltage is observed for both types of single-walled carbon nanotubes.

| $f$ [MHz] | $\lambda$ [nm] | $c_1[V^{-2}]$                     |
|-----------|----------------|-----------------------------------|
| 50        | 650            | $(3.959 \pm 0.381) \cdot 10^{-6}$ |
| 50        | 950            | $(4.130 \pm 0.513) \cdot 10^{-6}$ |
| 60        | 650            | $(2.522 \pm 0.125) \cdot 10^{-6}$ |
| 60        | 950            | $(2.305 \pm 0.148) \cdot 10^{-6}$ |
| 70        | 650            | $(2.646 \pm 0.296) \cdot 10^{-6}$ |
| 70        | 950            | $(3.074 \pm 0.166) \cdot 10^{-6}$ |
| 80        | 650            | $(1.325 \pm 0.119) \cdot 10^{-6}$ |
| 80        | 950            | $(1.132 \pm 0.077) \cdot 10^{-6}$ |

**Table 5.1:** Results of a fit according to Equation (5.2) of the relative absorbance versus applied voltage as displayed in Figure 5.5.

According to Equation (D.8),

$$c_1 V_{\text{pp}}^2 = \frac{U_0}{k_B T}. \quad (5.3)$$

In the analysis of the polarization dependent absorption spectra, values of  $U_0/k_B T = 2.3$  for metallic and  $U_0/k_B T = 0$  for semiconducting single-walled carbon nanotubes were determined. Here,  $c_1 V_{\text{pp}}^2$  is of the order of  $10^{-6} \text{ V}^{-2} \cdot 10^4 \text{ V}^2 = 10^{-2}$  for both electronic types. This is in agreement with the expected behavior in the case of semiconducting nanotubes, but not for the metallic nanotubes—in fact, those behave like semiconducting SWNTs in this experiment.

In experiments that are carried out at the INT and focused on the dielectrophoretic deposition of surfactant-stabilized single-walled carbon nanotubes a similar effect is observed: occasionally, metallic nanotubes can not be deposited in the high-frequency range, even though they should experience an attractive force. This indicates that their polarizability is disturbed. This occurs only when aged nanotube suspensions are used. While neither the underlying mechanism nor the characteristic time scale have been identified so far, a degradation of the electronic system apparently takes place, caused e. g. by a protonation [107]. A conclusive interpretation will only be possible after the experiment will have been repeated using freshly prepared nanotube suspension; the suspension used in this study was prepared six month prior to the experiment.

Repeating the experiment with single-walled carbon nanotubes dispersed in non-ionic solvents might give further insights. Non-ionic solvents have a much lower conductivity  $\sigma_l$  than the surfactants used in this study. As a result of this, the Clausius-Mossotti function changes significantly for non-ionic solvents, which might cause the dielectrophoretic torque to dominate the alignment of the nanotubes at lower electric field strengths. However an alternative process to solubilize and stabilize the nanotubes is required in non-ionic solvents. In a recent

work it was shown that stable suspensions of individual single-walled carbon nanotubes can be produced by the use of aromatic polymers in organic solutions [108]. Additionally the non-zero conductivity of semiconducting nanotubes observed in ionic surfactants—which is understood to be due to a finite surface conductivity caused by diffusive ions [25]—should be absent in non-ionic solvents such as toluene [108, 109]. This will severely change the behavior of semiconducting nanotubes under DC and AC dielectrophoresis.

### Summary

The alignment of single-walled carbon nanotubes under the influence of external electric fields depends on the dielectric properties of the nanotubes and is therefore expected to differ significantly for the two electronic types. An analysis of the degree of alignment as a function of the external electric field should allow to determine the electronic properties of the nanotubes under examination. With the experimental setup introduced above, the absorbance of dispersed carbon nanotubes can be measured under variation of the electric field strength and frequency. Since nanotubes predominantly absorb light which is polarized parallel to their axis, the average orientation of a nanotube sample can be deduced from the measured absorbance.

The results of a measurement on surfactant-stabilized carbon nanotubes demonstrated a dependency of the average alignment on the applied electric field and qualitatively confirmed the expected behavior. However, the effect was small and not electronic-type-specific. The analysis revealed that the observed behavior of metallic nanotubes resembles the expected—and observed—behavior of semiconducting nanotubes. This might be explained by a degradation of the electronic system of the metallic single-walled carbon nanotubes; however, the underlying mechanism remains obscure. For a conclusive interpretation of the data, the experiment has to be repeated with freshly prepared nanotube suspension.

A similar experiment on single-walled carbon nanotubes dispersed in non-ionic solvents is considered very promising, as it might reveal new insights. The dielectric properties of non-ionic solvents differ greatly from those of aqueous systems. In particular the conductivity is significantly reduced, which should also diminish the surface conductivity of semiconducting nanotubes. This will change the overall behavior of single-walled carbon nanotubes under dielectrophoresis with respect to the so far studied systems. In particular, the dielectrophoretic torque might dominate at smaller field strengths.

## 6. Transport of single-walled carbon nanotubes through nanopores

As discussed in the previous chapters, dielectrophoresis allows for the separation of metallic and semiconducting nanotubes on interdigitated electrode arrays. In this setup, the electric potential and thereby also the electric field strength decays exponentially in the direction normal to the sample surface according to  $\Phi(z) \propto \exp(-2\pi z/\lambda)$  [110]. Here,  $\lambda$  is the period of the interdigitated electrodes, which—for the generation of electric fields of  $\sim 10^7$  V/m or more—needs to be of the order of no more than a few  $\mu\text{m}$ . Consequently, the range in which the directed motion generated by the dielectrophoretic force exceeds the random Brownian motion is restricted to a few micrometer above the electrode array. Dielectrophoresis on interdigitated electrodes and other planar electrode structures therefore has a two-dimensional character and is efficient only for small volumes of nanotube suspensions ( $\sim \mu\text{l}$ ).

There were some proposals how to overcome this limitation. In a first approach a dielectrophoretic deposition on  $\text{cm}^2$  sized electrode structures was repeated several times using the same suspension volume [28]. It could be shown that the suspension became gradually enriched in semiconducting nanotubes (from 65 % to 94 %). However, this technique uses planar electrode structures to generate the electric fields and is therefore not scalable to high solution throughput either. Another method employs a continuous-flow microfluidic system with isolated electrodes [29]. Compared to the static dielectrophoresis, the separation efficiency of the microfluidic approach is reduced, possibly due to residual nanotube bundles and a very short period during which the nanotubes are exposed to the AC voltage. The authors claim that future improvements of the microfluidic separation cell might enable efficient bulk separation; however, this is yet to be verified experimentally.

The ultimate approach towards a truly scalable dielectrophoretic separation consists of a setup where the electric fields act throughout a suspension volume of several ml and which as result yields two volume fraction, one containing the metallic, the other the semiconducting SWNTs. For this, the so-called electrodeless dielectrophoresis is a promising candidate.

### Principle of electrodeless dielectrophoresis

Electrodeless dielectrophoresis was introduced for the dielectrophoretic trapping of molecules, e. g. as part of a micro total analysis system [111,112]. In an electrodeless dielectrophoresis setup, a homogeneous electric field is generated inside a conducting liquid by two parallel macroscopic electrodes. The liquid volume is subdivided in two ‘half cells’ by an insulating membrane positioned centrally between and in parallel with the electrodes, which exhibits one or many holes. These holes act as constriction for the liquid and the electric fields and thus constitute regions of high electric field inhomogeneity.

The potential distribution at the constriction and in particular the region of field inhomogeneity is defined mainly by the shape of the hole. In a double-conical hole, as used in References [111,112], the electric field is strongly focused at the constriction. In a cylindrical hole on the other hand, the field is homogeneously enhanced within the whole pore and the field inhomogeneity is limited to the region just outside the hole. Figures 6.1(a) and (b) show the electric field distribution for these two configurations; the electric field strength is specified by the color code and the white lines represent the field lines. These two examples demonstrate that, again, the dielectrophoretic forces are restricted to a small volume fraction, namely the region close to the holes. Therefore a driving force is required to translate the nanotubes contained in the bulk volume into the vicinity of the membrane. This driving force, which might be established by a DC bias between the electrode or a difference in the hydrostatic pressure between the two half cells, will also break the otherwise symmetric force field.<sup>1</sup>

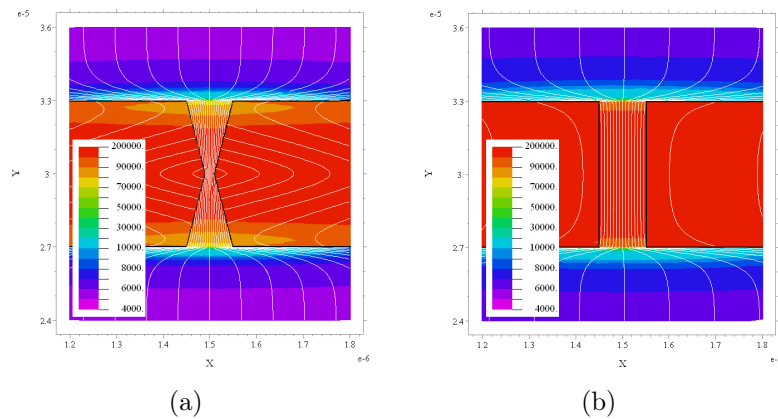


**Figure 6.1:** Electric field distribution in a double-conical constriction (a) and in a cylindrical hole (b). The colors represent the electric field strength in V/m according to the color keys and the field lines are illustrated in white.

<sup>1</sup>Due to the symmetry of the setup, the dielectrophoretic force is equal on either side of the membrane.

Regarding the use of electrodeless dielectrophoresis to separate metallic and semi-conducting nanotubes, it is crucial to optimize all parameters such that the semi-conducting nanotubes are repelled from the pore regions while the metallic nanotubes are attracted into the pores by the dielectrophoretic force and transported through them by the above mentioned driving force, e. g. an electrophoretic force. Starting with a suspension containing individually dispersed nanotubes on the one side of the membrane and pure surfactant suspension on the other side, this setup then allows to separate the two nanotube species into two volume fractions.

## Elektrokinetics

The translation of a colloidal particle with non-zero net charge and suspended in a liquid medium under the influence of an external electric field is called electrophoresis [71]. Unlike dielectrophoresis, which requires an inhomogeneous field, electrophoresis occurs in electric fields which are constant in time and space. The net charge  $Q$  of the particle is defined through its surface charge  $\sigma_p$ ,  $Q = \int \sigma_q dS$ , and the electrophoretic force due to Coulomb interaction is given by  $\vec{F}_{ep} = Q\vec{E}$ . The friction between the particle and the viscous liquid leads to a constant velocity  $\vec{v}$ . The electrophoretic mobility  $\mu_e$  is defined as

$$\mu_e = \frac{|\vec{v}|}{|\vec{E}|} = \frac{v}{E}. \quad (6.1)$$

When immersed in an electrolyte, particles are surrounded by an electrical double layer (EDL) formed by the ions in suspension. The charges in the double layer screen the surface charge of the particle such that it appears electrically neutral. Still, in the presence of an electric field the particle moves. It turns out that actually the counter ions in the EDL move and drag the fluid with them, an effect called electroosmosis. However, due to its viscosity, the fluid remains immobile and instead the particle is pushed in the direction opposite to the fluid flow. Thus the particle appears to be moving as if the field was acting on its surface charge. The reason for this lies in the properties of the EDL.

The electrostatic interaction between the non-zero surface charge of the particle and the ions in suspension effectuates the attraction of ions with opposing charge (counter ions) and the repulsion of ions with like charge (co-ions). As illustrated in Figure 6.2, the resulting charge distribution around the particle can be separated into several regions: Closest to the particle lies the Stern layer, which consists of ions adsorbed to the surface (also called ‘inner Helmholtz layer’) and bound hydrated ions (called ‘outer Helmholtz layer’). Within the Stern layer, the potential drops linearly from the surface potential to the potential at the outer Helmholtz layer. The adjacent region, which contains a high density of counter ions and a low density of co-ions, forms the diffusive layer. Here, the potential

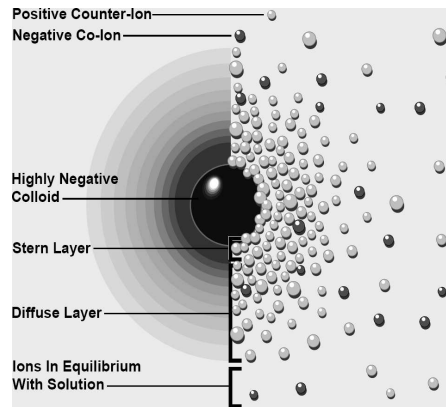


**Figure 6.2:** Schematic of the electrical double layer. The left representation depicts the change in the charge density and the right model shows the distribution of positive and negative ions surrounding a charged colloid. The layer of bound or tightly adsorbed ions is called Stern layer and the adjacent region containing a high density of counter ions and a low density of co-ions forms the diffusive layer. From Ref. [113].

decays exponentially with a characteristic decay length equal to the Debye length  $\kappa^{-1}$ .

According to the nature of this classification, the contact region between the outer Helmholtz layer and the diffusive layer defines the slip plane, i. e. the region at which the fluid starts to move with respect to the particle's surface. The potential at this slip plane is commonly called  $\zeta$ - (zeta-)potential.<sup>2</sup>

The total charge of the particle and the surrounding electronic double layer is zero and, consequently, this entity does not experience a Coulomb force. However, the ions in the diffusive layer have the same mobility as the bulk solution, and the ions in the Stern layer are bound but also have non-zero mobility. They move under the influence of the electric field and thus give rise to a fluid motion around the particle (electroosmosis). Due to the excess of counter ions in the EDL, the fluid motion is directed opposite to the motion the unscreened particle would acquire. Since this ionic movement occurs in the regime of low Reynolds number (the fluid is viscous and the particles are very small), the bulk liquid remains stationary and the moving ions instead push the particle in the opposite direction. Again, this picture is only a simplification: The electric field additionally invokes a charge separation in the EDL, with the co-ions moving ahead of the particle and the counter ions moving in the opposite direction, which results in a polarization of the EDL. The polarization field can go with or against the external electric field, thereby either increasing or decreasing the electrophoretic velocity of the particle.

<sup>2</sup>Note that this model is a simplification of the realistic situation and that the precise form of the EDL and the position and extension of the slip plane are still under debate. A more detailed picture as well as further references can be found in Reference [114].

Clearly, the functional dependence of the electrophoretic velocity on the parameters of the EDL is generally quite complex. However, in practice the EDL is characterized by its extension  $\kappa^{-1}$  with respect to the particle radius  $a$  and two limiting cases are considered: In the ‘thin double layer approximation’ with  $\kappa a \gg 1$ , which is satisfied by many aqueous dispersions,

$$\mu_e = \frac{\varepsilon\zeta}{\eta} \quad (\text{Helmholtz-Smoluchowski limit}), \quad (6.2)$$

where  $\eta$  and  $\varepsilon$  denote the viscosity and the permittivity of the liquid. For ‘thick double layers’ with  $\kappa a \ll 1$ , as satisfied for very small particles and very low ionic strength of the electrolyte,

$$\mu_e = \frac{2\varepsilon\zeta}{3\eta} \quad (\text{Hückel-Onsager limit}). \quad (6.3)$$

In a more general approach, the mobility is written as

$$\mu_e = \frac{\varepsilon\zeta}{\eta} f(\kappa a) \quad (\text{Henry}). \quad (6.4)$$

The above relations are based on the—very restrictive—assumption that the structure of the EDL is not distorted by the applied electric field and they neglect the effect of surface conduction.

## 6.1. Experimental

### 6.1.1. Experimental setup

To investigate the electrodeless dielectrophoresis of single-walled carbon nanotubes, a cell was designed that permits to monitor the content of nanotubes in both half cells by *in situ* measurements of the absorption. This ‘DEP cell’, a photograph of which is presented in Figure 6.3, has a cylindrical geometry. It consists of two identical half cells with a length of 10 mm and radius of 5 mm, which are separated by a 6  $\mu\text{m}$  thick polycarbonate membrane<sup>3</sup> with cylindrical pores of 10–100 nm diameter and a density of  $n = 6 \cdot 10^{12} \text{ m}^{-2}$ .<sup>4</sup> The electrodes are made of glassy carbon<sup>5</sup> and are located at the two faces of the cylinder. The electric field is therefore oriented parallel to the cylinder axis.

To measure the absorbance, two holes were drilled into the sidewalls of each half cell into which collimators are screwed. Optical fibers can be attached to and

---

<sup>3</sup>The membranes were purchased from Pieper Filter GmbH [115].

<sup>4</sup>For the plots shown in Figure 6.1(b) and (c) a diameter of  $r = 100 \text{ nm}$  was assumed.

<sup>5</sup>Purchased from HTM Hochtemperatur-Werkstoffe GmbH [116].

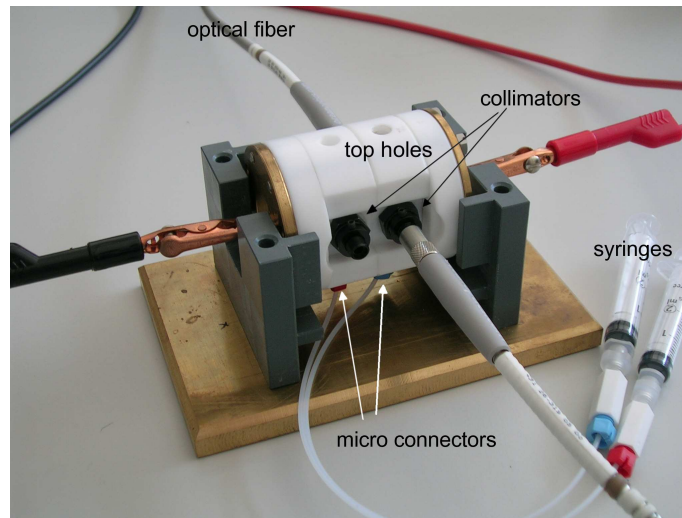


**Figure 6.3:** Photograph of the DEP cell. The individual components are referred to in the text.

detached from the collimators without disturbing the experiment. The collimators are situated such that the path of light inside the DEP cell is perpendicular to the cylinder axis. As light source and detector a Micropack DH-200-BAL Balanced Deuterium Tungsten Halogen Light Source and an Ocean Optics HR4000 High-resolution Spectrometer are used as in the experiment described in Chapter 5.

To fill (drain) the suspension into (from) the DEP cell, a small hole is positioned at the bottom of both half cells. Each is equipped with a micro connector that allows to connect syringes containing the suspension. Since the whole setup is designed to be water-tight, another small hole is necessary at the top of each half cell to enable air exchange during the filling and unfilling process. During the experiment this hole can be easily sealed with scotch tape.

In a typical experiment the two half cells are filled simultaneously (to avoid pressure differences on the two sides of the membrane), one with nanotubes dispersed in surfactant solution and the other with pure surfactant solution. The two filled half cells will be called ‘CNT side’ and ‘soap side’ in the following. Before starting the experiment, the absorbance on the soap side is measured as reference. Then a spectrum of the CNT side is taken. While the experiment runs, the development of the absorbance of the soap side is monitored—the appearance of nanotubes in this half cell leads to significant changes in the spectrum. At the end of the experiment, the contents of each side are removed from the DEP cell and the absorbance spectra are measured with a Varian Cary 500 UV-Vis-NIR spectrophotometer. This spectrometer covers a wider wavelength-range (200–1800 nm) than the spectrometer used for the *in situ* measurements (200–1100 nm) and therefore allows to probe the S1 band in addition to the M1 and S2 bands.

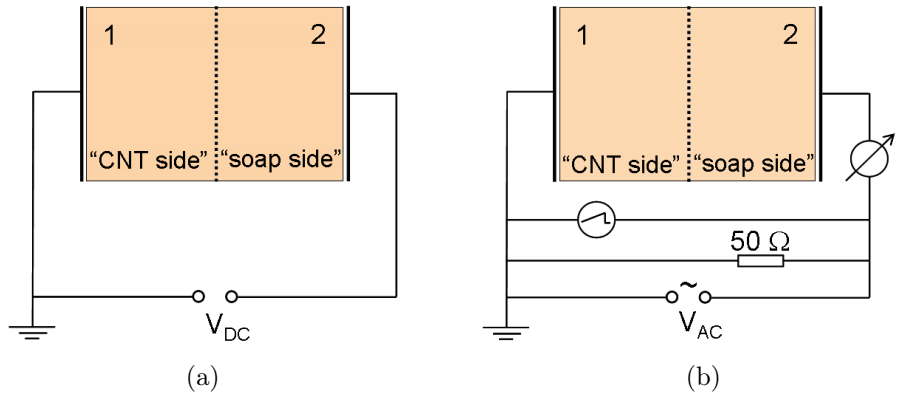


**Figure 6.4:** Circuit diagram of the experimental setup to measure transport of single-walled carbon nanotubes through nanopores in a DC (a) and AC (b) experiment. The DEP cell is highlighted in orange; the two half cells denoted ‘CNT side’ and ‘soap side’ are filled with nanotubes dispersed in surfactant solution and pure surfactant solution, respectively, at the beginning of the experiment.

Figure 6.4 shows the circuit diagram of the experimental setup to measure transport of single-walled carbon nanotubes through nanopores. In a DC experiment (Figure 6.4(a)), a Keithley 6430 Sub-Femtoamp Remote SourceMeter is used as voltage source. For an AC experiment (Figure 6.4(b)), the signal is generated with an Agilent 33250A Function/Arbitrary Waveform Generator and an Empower RF Systems High Power RF Amplifier. The AC voltage signal is monitored with an oscilloscope and the AC current is measured with a Keithley 2000 Multimeter.

Due to experimental observations discussed later (see Section 6.2.1), the setup described so far was optionally extended with a ‘Genie’ Programmable Syringe Pump (Kent Scientific Corporation). The pump was connected to the soap side via the micro connector at its bottom hole. By withdrawing the liquid from the otherwise sealed soap side, a hydrostatic pressure is built inside the DEP cell that enforces a liquid motion through the membrane from the CNT side into the soap side.

### 6.1.2. Impedance spectroscopy of the DEP cell

To identify the dominant contributions to the impedance of the experimental setup, the impedance spectrum of the DEP cell filled with various types of suspensions (distilled water and  $D_2O$  with different concentrations of SDBS) was measured in the frequency range  $f = 50\text{--}10^6$  Hz with an Agilent 4284A Precision LCR Meter. Two membranes with differing pore sizes (10 nm and 50 nm) were examined. The results are illustrated in Figure 6.5.

The measurements clearly indicate that the ohmic conduction ( $\Theta = 0^\circ$ ) prevails

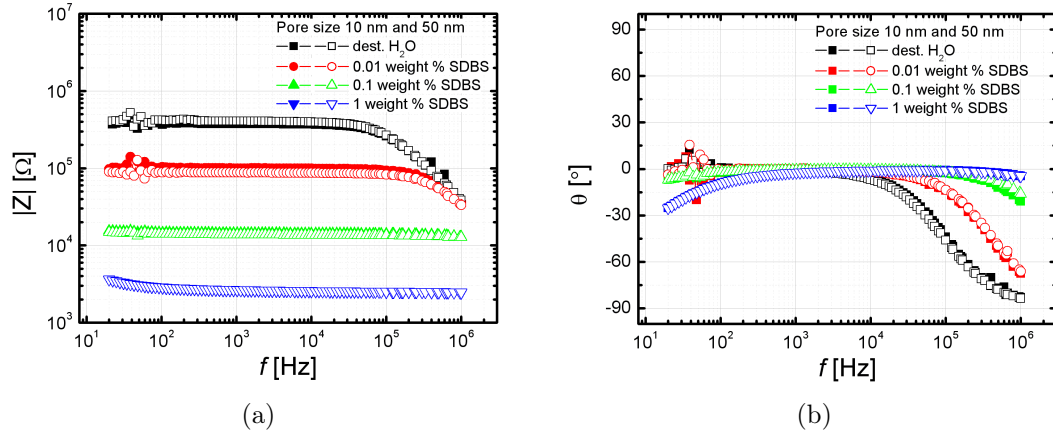


**Figure 6.5:** Impedance spectra of the DEP cell filled with various types of suspensions. Plotted are in (a) the absolute value  $|Z|$  and in (b) the phase  $\Theta$  versus excitation frequency for pore sizes of 10 nm and 50 nm (closed and open symbols, respectively). The ohmic conduction ( $\Theta = 0^\circ$ ) dominates in a wide frequency range. The resistance decreases with increasing solution conductivity and is virtually independent of the pore size.

the total impedance in a wide frequency range. The resistance diminishes with increasing SDBS content due to the growing number of surfactant ions. In particular, for a SDBS content of 1 weight %, as used in most of the experiments, the resistance is in the range of a few  $k\Omega$ .

There are two contributions to the ohmic resistance of the liquid: one is the resistance of the liquid volume contained in the two half cells,  $R_1$ , and the other is the resistance caused by the sum of constrictions in the pores,  $R_2 = 1/N \cdot R_3$ , where  $R_3$  is the resistance of a single pore and  $N$  is the number of pores<sup>6</sup>.  $R_1$  and  $R_3$  can be easily calculated from the characteristic dimensions (length  $L$  and area  $A$ ) according to  $R = 1/\sigma \cdot L/A$ . It follows  $R_1 \approx 1 k\Omega$  (in good agreement with the impedance measurements),  $R_3 \approx 10^{10} \Omega$  and  $R_2 \approx 30 \Omega$ . Obviously, the resistance of a single pore exceeds  $R_1$  by several orders of magnitude, but due to the high number of pores in the membrane, the resistance  $R_2$  is two orders of magnitude smaller than  $R_1$ .<sup>7</sup> As a consequence, the voltage drop at the membrane  $V_{\text{membrane}}$  is only a small fraction ( $R_2/R_1$ ) of the voltage applied at the electrodes. However, since this voltage drop occurs over a length which is defined by the membrane

<sup>6</sup> $N = n \cdot A_{\text{membrane}}$  with pore density  $n = 6 \cdot 10^{12} \text{ m}^{-2}$  and membrane surface  $A_{\text{membrane}} = \pi \cdot (5 \text{ mm})^2$ .

<sup>7</sup>Since  $R_1 \gg R_2$  for all pore radii used in this study, the impedance spectra are virtually independent of the pore radius, as apparent from Figure 6.5.

The large number of pores also inhibits to detect the transport of nanotubes through the pores by measuring the current noise in the setup [117]. In the case of single pores this technique allows not only to detect the translocation of a molecule, but also to determine its length by measuring the dwell time [118].

thickness of  $6\ \mu\text{m}$ , the electric field is still significantly enhanced inside the pores as compared to the two half cells (with a length of 10 mm each).

## 6.2. Results and discussion

To determine the performance of the experimental setup and identify the existing forces, first experiments were conducted using large nanopores (50–100 nm) and short single-walled carbon nanotubes (dispersed in SDBS or NaCh solution), to facilitate the movement of the nanotubes through the pores. In the following, first experiments with both DC and AC voltages and their results are presented and the implications of the observations are discussed.

### 6.2.1. Experiments with DC voltage

According to the results of the measurements described Appendix E, to translocate single-walled carbon nanotubes from the CNT side to the soap side, a positive DC bias  $V_{\text{DC}}$  has to be applied to the soap side. A number of experiments was conducted with  $V_{\text{DC}} = 0\text{--}5\ \text{V}$  and a pore size of 50 nm. No appearance of nanotubes in the soap side was observed. Instead, a liquid flow from the soap side to the CNT side became apparent: the fluid level of the soap side, which can be monitored by eye through the top hole of this half cell, increased visibly within an observation time of several minutes.

This is again a consequence of the ionic surfactant, which forms an electronic double layer not only around the nanotubes but also at other material surfaces, e. g. at the membrane and in particular inside the nanopores. As described above, the ions in the EDL are accelerated by the applied electric field, giving rise to a fluid flow called electroosmosis. While in the case of a small particle inside a bulk liquid this effect leads to a particle motion in the opposite direction, in the case of the liquid inside the capillary with immobile walls the EDL actually starts to move and drags along the liquid it encloses. An illustration of this effect is shown in Figure 6.6.<sup>8</sup> Due to adsorbed surfactant molecules, the surface charge of polycarbonate is negative and positive counter ions prevail in the EDL, causing a fluid movement in the direction of the electric field.

Apparently the electroosmotic fluid flow prevents the electrophoretic motion of single-walled carbon nanotubes through the nanopores. To compensate for the effect of electroosmosis, two approaches were pursued: (1) A syringe pump was connected to the soap side and set to a constant rate of withdrawal ( $\sim 10\ \mu\text{l}/\text{min}$ ).

---

<sup>8</sup>Under the assumption of a thin double layer it can be shown that the liquid acquires a velocity distribution that is nearly uniform throughout the channel [119], unlike the common parabolic velocity profile inside a fluid channel.

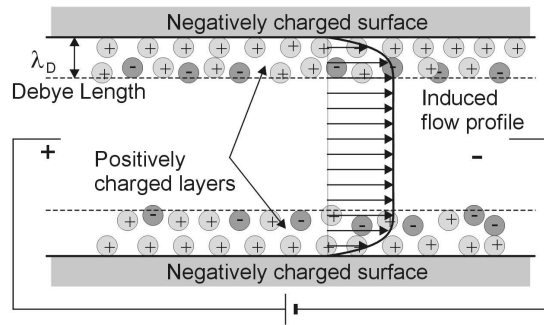


**Figure 6.6:** Schematic of electroosmosis in a micro channel. In the electronic double layer formed at a negatively charged surface, positive charge carriers dominate. Under application of an external DC voltage, the movement of the positive charges gives rise to a fluid movement directed towards the negative electrode. From Ref. [120].

(2) A thin metal layer (Ti/Pd) was sputtered onto both sides of the membrane. The electroosmotic flow from the soap side to the CNT side leads to a depletion of positive ions on the soap side and an excess on the CNT side. If the charges were trapped on the metal coating, this would result in a local electric field which might eventually cancel the opposed global field.

In the experiment the latter approach did not show any effect—the electroosmotic flow still prevails and the carbon nanotubes do not pass through the membrane. The application of a hydrostatic pressure, on the other hand, efficiently enforces both liquid and nanotube motion from the CNT side into the soap side. However, it is most likely that in this case the nanotubes are merely dragged along by the liquid and that the influence of electrophoresis is negligible.

Only in one experiment did the absorbance spectrum on the soap side display a distinct shape as compared to the original SWNT spectrum. In this experiment a metal coated membrane as well as the syringe pump were used and both the applied voltage and the pump rate were varied repeatedly during the experiment. Figure 6.7 shows the data measured on the content of the soap side after the experiment (red curve in the upper graph) and, for comparison, the starting suspension (black curve in the lower graph).

A comparison between the two curves shows clearly that the shape of the M1 band after the experiment differs strongly from the original shape—the ‘fine structure’ indicates a reduction of large diameter tubes and an enhancement of small diameter tubes (for comparison, see also Figure 2.13). Also, the M1 band is significantly pronounced with respect to the S2 band.

The S1 band is suppressed to a large extent. This is indicative of a decreased pH value [107] and indeed, a pH value of 2–3 was measured. The pH change is caused by the application of a DC voltage larger than the dissociation energy of water (+1.23 V). Comparative experiments with either pure D<sub>2</sub>O or nanotube

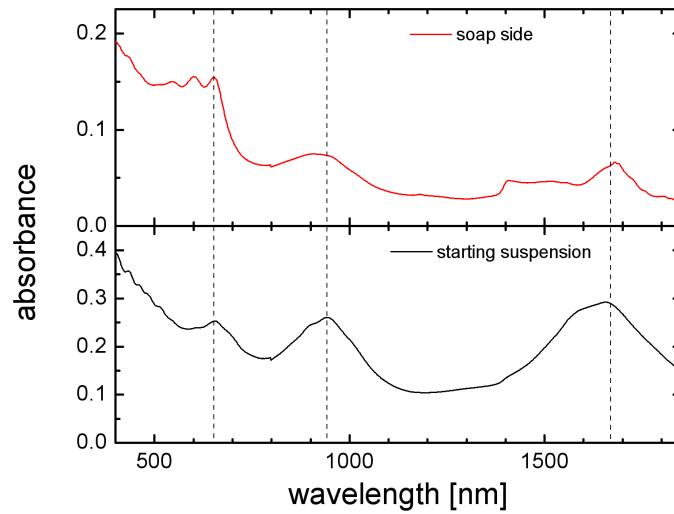


**Figure 6.7:** Absorbance spectrum measured after a DC experiment with a metal coated membrane and a variable pump rate. The red curve in the top graph shows the absorbance of the content of the soap side and the black curve in the bottom graph represents the starting solution; the dashed lines mark the centers of the M1, S2 and S1 band. The red curve displays two distinctive features: (1) The M1 band is strongly pronounced especially for small diameter nanotubes with respect to the S2 band. (2) The S1 band is severely suppressed and also distorted, indicating a contamination of the  $D_2O$  with atmospheric  $H_2O$ .

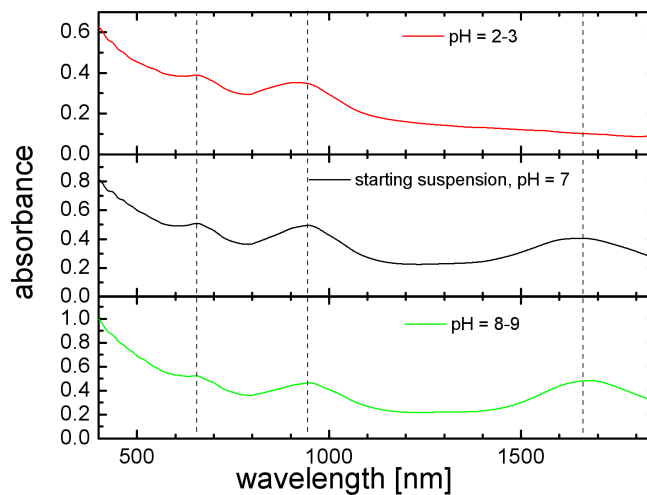


**Figure 6.8:** Absorbance spectrum measured after a comparative DC experiment. The pH values are indicated in the graphs; the dashed lines mark the centers of the M1, S2 and S1 peak. The height of the S1 band depends strongly in the pH value, but the M1 and S2 bands are mostly unperturbed.

suspension in both half cells verify a pH value of 2–3 at the cathode side and a value of 8–9 at the anode side after application of +5 V. Figure 6.8 shows the corresponding absorbance spectra; the influence of a small pH value on the S1 band is very strong, however no change in the intensities of the M1 and S2 bands are observed. The ratio of the M1 and S2 band intensities is therefore a pH-independent measure of the sample composition.

From this analysis it can be deduced that more metallic than semiconducting single-walled carbon nanotubes were translocated, as intended by the experimental design. Unfortunately it was not possible to reproduce these experimental results.

### 6.2.2. Experiments with AC voltage

According to the results of the experiments with DC voltage, the application of a DC voltage does not yield the anticipated electrophoretic motion of single-walled carbon nanotubes from the CNT side to the soap side. Instead, the effect of electroosmosis is dominant and causes a liquid movement in the opposite direction and, additionally, the pH value of the liquid changes for voltages above the dissociation energy of water: electrophoresis is obviously not a suitable driving force in this system. In the next step, the effect of AC voltages with and without the pumping option was investigated. Provided the experimental parameters are chosen properly, the application of hydrostatic pressure (by withdrawing the liquid from the soap side) and an AC voltage  $V_{pp}$  should result in a translocation of preferentially metallic carbon nanotubes.

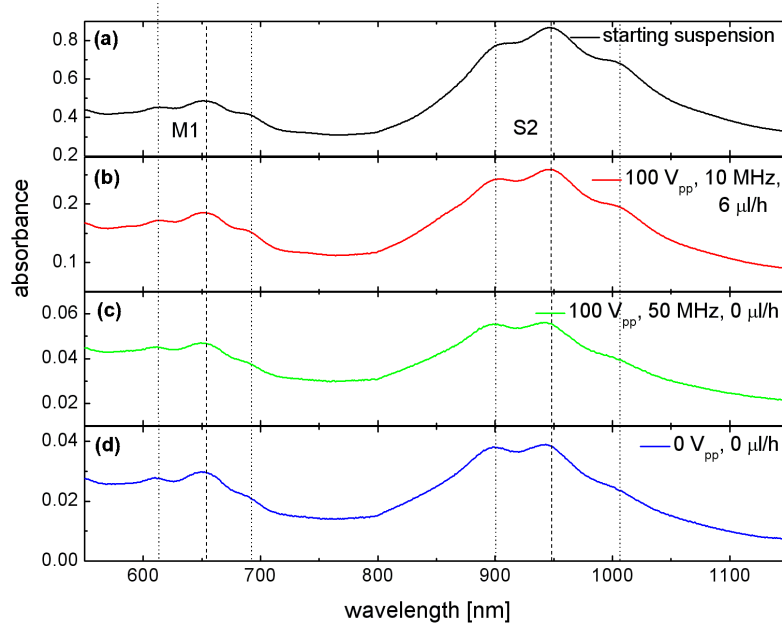
In the series of experiments described in the following, the pumping rate was either set to  $6 \mu\text{l/hr}$ <sup>9</sup>, which is the minimum rate accessible with the syringe pump, or the pump was switched off. In the latter case the driving force is entirely due to diffusion. Either a pulsed AC voltage<sup>10</sup> of  $V_{pp} = 100 \text{ V}$  and  $f = 10\text{--}50 \text{ MHz}$  was applied or the AC signal was turned off as well. Short nanotubes dispersed in  $\text{D}_2\text{O}$  with 1 weight % NaCh and Iodixanol and membranes with a pore size of 100 nm were used.

Figure 6.9 shows the absorption spectra obtained in this series of experiments. The black curve in Figure 6.9(a) illustrates the absorbance of the starting suspension. The M1 and S2 bands are marked and the dashed and dotted lines emphasize the central peak (at 650 nm and 950 nm) and the subpeaks caused by nanotubes with relatively small and large diameter (subpeaks to the left and right of the central peak, respectively).

The red curve in Figure 6.9(b) was measured on the content of the soap side after

<sup>9</sup>Due to this low pumping rate, the run time of the experiments was four days. Comparative experiments without pumping lasted as long.

<sup>10</sup>A pulsed signal with  $t_{ON} = 50 \mu\text{s}$  and  $\tau = 1 \text{ ms}$  was used instead of a continuous voltage to reduce the amount of power dissipated in the DEP cell.



**Figure 6.9:** Absorbance spectra measured after AC experiments. An analysis of the observed features is given in the text. Note the different scales of the ordinate in the subfigures.

an experiment with AC voltage of  $V_{pp} = 100$  V and  $f = 10$  MHz and a pumping rate of  $6 \mu\text{l/hr}$ . The absorbance largely resembles that of the original suspension, with the signal being reduced by approximately a factor of 3 due to dilution. Comparing the heights of the M1 and S2 band (central peak), an increase of the metallic band becomes apparent. Also, the left subpeak of the S2 band (caused by nanotubes with comparatively small diameter) is slightly enhanced with respect to the central peak. This becomes more obvious in Figure 6.10, where the absorbance spectra normalized with respect to the central S2 peak at 950 nm is plotted for the same series of experiments.

After an experiment with zero pumping rate,  $V_{pp} = 100$  V and  $f = 50$  MHz, the green curve in Figure 6.9(c) was obtained. The signal intensity is much lower (less than one-tenth of the original suspension), since the translocation of single-walled carbon nanotubes is not very efficient when the process is purely diffusive. However, the trends discussed for the red curve are still valid and have even intensified (see Figure 6.10): The height of the M1 band has further increased with respect to the S2 band. The change in the relative heights of the subpeaks of the S2 band is also more pronounced; the subpeak caused by large diameter nanotubes has almost disappeared and the central peak and the left subpeak are at the same level.

Apparently, the observed translocation of single-walled carbon nanotubes through nanopores is, to a certain extent, both diameter selective—a closer look

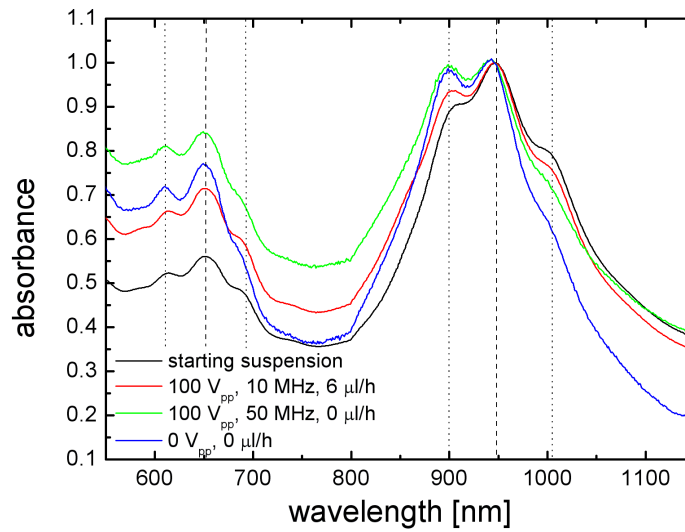


**Figure 6.10:** Normalized absorbance spectra of the same set of data presented in Figure 6.9. This illustration emphasizes the relative changes in the heights of the M1 and S2 bands as discussed in the text.

into the evolution of the M1 band reveals a similar although somewhat reduced enhancement of small diameter nanotubes—and electronic type selective. The diameter selectivity might be caused by a preferred transport of small nanotubes through the constrictions. In this case, a reduction of the pore size should further decrease the probability of a passage of large and eventually also small nanotubes, while an increase above a critical value should cease the diameter selectivity.

To validate whether the favored translocation of metallic nanotubes through the membrane is caused by the dielectrophoretic forces, the experiment is repeated without applied voltage. The resulting absorbance on the soap side is represented by the blue curve of Figure 6.9(d). Except for a further decrease of the signal, the absorbance changes slightly with respect to the green curve. Obviously the observed effects are mostly independent of external fields and therefore caused by dielectrophoresis.

The experiment was repeated again with smaller nanopores (10 and 30 nm), with or without an applied voltage ( $V_{pp} = 100$  V and  $f = 50$  MHz) and in the absence of pumping. In neither case was the presence of carbon nanotubes detectable in the content of the soap side. This indicates that the pores are too small to allow for a translocation driven by the diffusion.

## Summary

The influence of DC and AC electric fields and hydrostatic pressure on the translocation of single-walled carbon nanotubes through nanopores was studied in a

test cell. Measurements of the electrophoretic mobility of carbon nanotubes established a negative surface charge of carbon nanotubes, which therefore under electrophoresis move in the direction opposite to the external field. However, when a DC voltage is applied to the test cell, electroosmosis inside the nanopores leads to a strong liquid motion opposed to the anticipated nanotube movement, thereby inhibiting the translocation of carbon nanotubes due to electrophoresis. Additionally the pH value in the two compartments of the cell changes if the applied voltage exceeds the dissociation energy of water. In one experiment, the combination of a DC voltage and a counteractive hydrostatic pressure resulted in a strong enhancement of the M1 peak in the absorbance spectrum; this could unfortunately not be reproduced in further experiments.

A series of experiments under variation of the applied AC voltage and the pumping rate revealed a preferential translocation of small diameter nanotubes through the membrane. The process also proved to be electronic type specific to a small extent. However, both effects turned out to be independent of the AC field. While the reason for the reduction of the semiconducting nanotubes could not be identified, the diameter selectivity is apparently intrinsic to a diffusive transport of single-walled carbon nanotubes through the constrictions. These results indicate that the chosen experimental setup might be suited for an upscaling of the separation of surfactant-stabilized carbon nanotubes by means of electrodeless dielectrophoresis, however the process parameters need to be further explored. As in the previous chapter, the use of single-walled carbon nanotubes dispersed in non-ionic solvents might give further insights. For example the effect of electroosmosis should be absent in such systems.



## 7. Summary and outlook

This work was focused on the behavior of single-walled carbon nanotubes under the influence of dielectrophoretic forces. In particular, it aimed at an profound understanding of the fundamental processes in dielectrophoretic separation and assembly experiments.

In the first part, the dielectrophoretic deposition of single-walled carbon nanotubes onto interdigitated electrode arrays was studied. The use of an electrode material with an insulating oxide layer (Al/Al<sub>2</sub>O<sub>3</sub>) allows to produce continuous films of carbon nanotubes with this method. It was shown that the application of high electric fields leads to a deposition of semiconducting nanotubes even for frequencies above the cross-over frequencies observed before. Additionally, polarization dependent absorption spectroscopy of the nanotube film revealed that metallic and semiconducting nanotubes possess a significantly different degree of alignment with respect to the electric field during deposition: metallic nanotubes are well aligned parallel to the electric field, while semiconducting nanotubes are randomly oriented on the sample. Two important conclusions were drawn from this observation: the nanotubes are deposited individually and, although both electronic types experience a positive dielectrophoresis, their response to the electric field is incisively different. To explain the experimental observations, the theoretical framework which is generally used in the context of nanotube dielectrophoresis was revised. The formalism for the dielectrophoresis of rod-like particles is derived under the assumption of a specific and constant orientation of the particle with respect to the electric field. The advanced model that was introduced in this work allows for an arbitrary orientation which is determined by the relation between the the dielectrophoretic torque and the thermal energy. Furthermore, the basic model considers only the dielectric properties along the long axis of the particle. However, single-walled carbon nanotubes exhibit a large anisotropy both in their geometric as well as their dielectric properties. This is explicitly incorporated into the advanced model. The new formalism was used to predict the average alignment of metallic and semiconducting nanotubes as a function of the electric field strength and frequency. At low frequencies both nanotube type show a similar behavior, however at high frequencies, their alignment differs significantly: In the case of metallic nanotubes, moderate deposition parameters suffice to obtain a highly ordered phase. Semiconducting nanotubes, on the other hand, preserve the isotropic phase up to much higher field strength, and transitions from one stable position into another in the ordered phase are predicted. A fit of the ex-

perimental data using the advanced model showed a good agreement between the calculations and the experiment. The topic of the deposition of semiconducting nanotubes at high frequencies was addressed in a simulation based on the finite element method. The results gave evidence that within a certain frequency range, which is determined by the dielectric properties of the nanotubes, semiconducting nanotubes experience a positive dielectrophoresis solely due to their orthogonal polarizability, which was neglected in previous calculations.

Further finite element simulation were carried out to explain experimental results obtained at the INT, e. g. on the deposition of short metallic single-walled carbon nanotubes onto gold electrodes, structured either on insulating quartz glass or on oxidized conducting silicon substrate. A simulation of the dielectrophoretic force fields in both structures showed that the presence of the conducting substrate leads to a repulsion of the nanotubes in the central region of the electrode gap, while the dielectrophoretic forces are attractive throughout the gap in the case of the isolating substrate. The results are consistent with the experimental observation of a substrate-specific deposition pattern.

The self-limiting behavior observed during the dielectrophoretic assembly of single-walled carbon nanotubes to form single-nanotube devices was initially explained by a short-circuiting of the electrodes by the nanotube. However, by means of impedance spectroscopy carried out at the INT this explanation was suggested to be invalid and an alternative mechanism was proposed, which involves a redistribution of the electric field. The potential distribution and the dielectrophoretic force in the electrode gap calculated in a finite element simulation support the latter explanation: In the absence of a nanotube, the dielectrophoretic force is attractive within the electrode gap. After the deposition of a nanotube, strong repulsive forces develop in the region around the nanotube, preventing further nanotube deposition. This change of the dielectrophoretic force fields is due to the high permittivity of the nanotube-surfactant hybrid as compared to the aqueous media.

A further simulation treated the examination of single-nanotube devices in the SEM and the prospect of using voltage-contrast SEM to characterize the electronic properties of the nanotubes: an electronic-type-specific evolution of the contrast displayed by single-walled carbon nanotubes under variation of the back-gate voltage was observed at the INT. First, the contrast difference between an electrically floating and a grounded electrode was explained by modeling the potential and electric field distribution in both cases. The simulations showed that floating electrodes acquire a potential similar to the substrate and therefore do not distort the electric field distribution. Grounded electrodes on the other hand cause large distortions of the surrounding electric field. As a consequence, floating electrodes display a contrast similar to the substrate and grounded electrodes appear brighter or darker, depending on the polarity of the back-gate voltage. In the next step, the contrast evolution of a nanotube deposited between a grounded and an otherwise

---

floating electrode was modeled. The simulation is based on the assumption that the permittivity of the semiconducting nanotube varies under the influence of the gate bias: For low nanotube permittivity, the influence of the nanotube on the potential of the floating electrode is negligible. As the nanotube becomes more polarizable, the influence increases until finally, for a semiconducting nanotube in its ON state or a metallic nanotube, the floating electrode is entirely coupled to the grounded drain electrode via the nanotube. The calculated potential distributions showed good agreement with the experimental observations.

Due to a strong depolarization effect perpendicular to their axis, single-walled carbon nanotubes predominantly absorb light polarized parallel to the axis. In an adequate experimental setup, the absorbance spectrum of a nanotube sample changes as a function of the average orientation of the nanotubes. According to the advanced model for dielectrophoresis established in this work, the alignment of metallic and semiconducting nanotubes in external electric fields differs significantly. As the alignment uniquely depends on the dielectric properties of the nanotubes, those can be determined by monitoring the alignment as a function of the electric field strength and frequency. An experiment was designed to measure the absorbance—and thereby the degree of alignment—of both electronic types under variation of the applied electric field. First results obtained for surfactant stabilized single-walled carbon nanotube suspensions revealed a change of the absorbance when an electric field is applied. When compared to the absorbance in the absence of the electric field, the relative absorbance—and thus the average alignment—qualitatively features the expected dependency. However, the dependence is weak and equal for both nanotube species. Based on experimental results regarding the dielectrophoretic deposition, it appears that the electronic properties of the metallic carbon nanotubes are disturbed, causing the metallic nanotubes to behave similar to the semiconducting ones. Further experiments are necessary to allow for a conclusive interpretation of the observations and to determine the influence of aging of the nanotube suspensions. Additionally, the use of single-walled carbon nanotubes dispersed in non-ionic solvents is very promising. Both the conductivity of the liquid and the surface conductivity of the nanotubes are expected to be drastically reduced for non-ionic solvents. This will significantly change the overall behavior under dielectrophoresis and might also cause the dielectrophoretic torque to dominate the average alignment at lower electric field strength, thereby facilitating this experiment.

It was suggested to apply the principle of electrodeless dielectrophoresis to the separation of single-walled carbon nanotubes. In an electrodeless dielectrophoresis setup two liquid volumes are separated by a insulating membrane, which contains one or many holes. When a homogeneous electric field is applied to the bulk liquid with the field vector directed perpendicular to the membrane, the field is “squeezed” through the constrictions. This results in strong field inhomogeneities inside and near the holes. Since the corresponding dielectrophoretic forces are re-

stricted to the vicinity of the membrane, an additional driving force is required to move the particles from the bulk liquid to the membrane. A test cell was designed to investigate the applicability of the principle of electrodeless dielectrophoresis for the separation of single-walled carbon nanotubes. In particular, the effect of DC electric fields or hydrostatic pressure as driving force was determined. One compartment of the cell was filled with carbon nanotubes in surfactant solution and the other was filled with plain surfactant solution. By an *in situ* measurement of the absorbance spectrum the translocation of nanotubes through the membrane could be detected. It was demonstrated (by measuring the electrophoretic mobility) that surfactant-stabilized carbon nanotubes move in the direction opposite to the applied DC field, i. e. their electrophoretic mobility and their surface charge is negative. To generate a driving force based on electrophoresis towards the membrane, an electric field pointing from the compartment containing pure surfactant into the nanotube's compartment was applied. It turned out that electroosmosis inside the nanopores leads to a prevailing liquid motion in the direction opposite to the anticipated nanotube movement. Within the experimentally accessible ranges, the application of a hydrostatic pressure led to an efficient translocation of metallic and semiconducting carbon nanotubes through the nanopores irrespective of the applied AC voltage. Experiments in which the driving force was merely due to diffusion revealed a preferential transport of small diameter nanotubes and electronic type selectivity. Both effects were reproduced in the absence of an AC field and are therefore not entirely due to dielectrophoresis. The diameter selectivity seems to be an intrinsic feature of a diffusion driven transport of single-walled carbon nanotubes through nanopores. The reason for the weakly preferred translocation of metallic needs to be further explored. According to these results, after an optimization of the process parameters, electrodeless dielectrophoresis might be suited for an upscaling of the separation of surfactant stabilized single-walled carbon nanotubes. It remains to be investigated whether the use of single-walled carbon nanotubes dispersed in non-ionic solvents will facilitate this approach.

# A. Characterization of the nanotube suspensions

Representative for the nanotube suspensions used in this work, the characterization of a few samples is presented in the following.

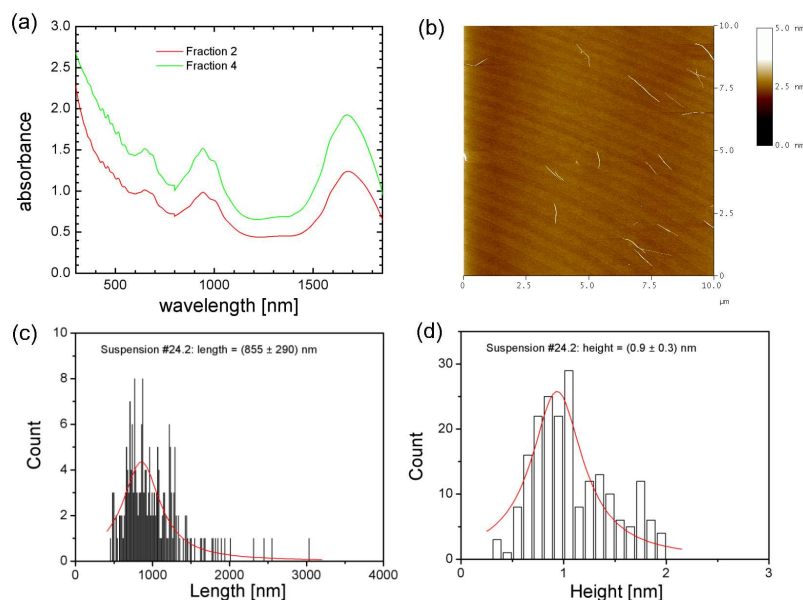


**Figure A.1:** Characterization of Suspension #24.2 and 24.4 (NiCo SWNTs in D<sub>2</sub>O with 1 weight %): (a) Absorbance spectrum of Fraction 2 and 4, (b) AFM image of nanotubes (Fraction 2) spin coated onto silicon, (c & d) length and height distribution. The mean length and height of Fraction 2 were determined to  $(855 \pm 290)$  nm and  $(0.9 \pm 0.3)$  nm.

Suspension 24 are NiCo nanotubes dispersed in D<sub>2</sub>O with 1 weight % NaCh as surfactant. The surfactant stabilized SWNTs were subject to size-exclusion chromatography. Fractions 2 and 4 were used in the experiments. The mean length and height of the nanotubes in Fraction 2 is  $(855 \pm 290)$  nm and  $(0.9 \pm 0.3)$  nm and the concentration of the suspensions is  $c_{\text{Fraction 2}} \approx 110 \mu\text{g/ml}$  and  $c_{\text{Fraction 4}} \approx 170 \mu\text{g/ml}$ . Figure A.1 shows the absorbance spectra of both fractions and the AFM image, length and height distribution of Suspension #24.2.

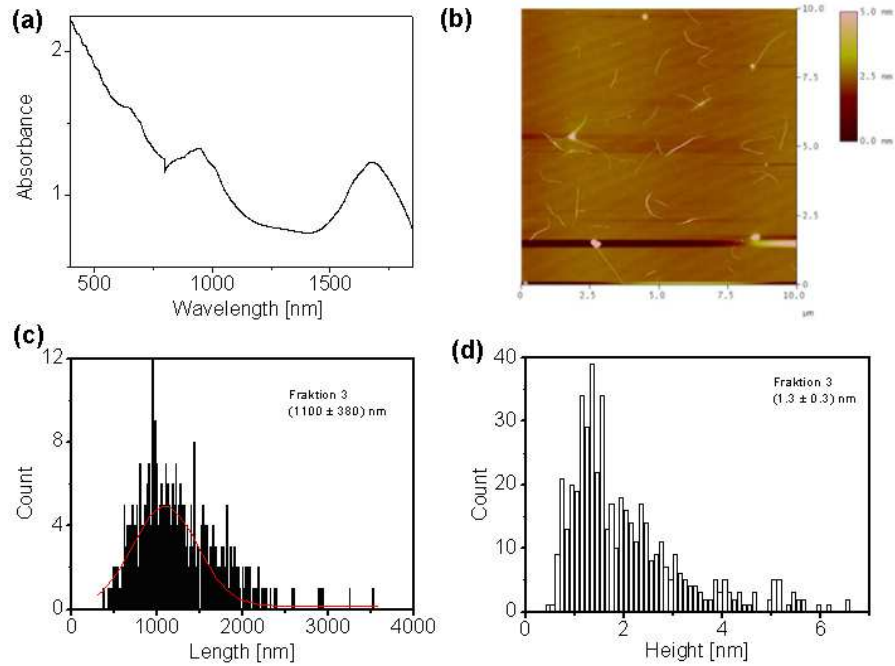


**Figure A.2:** Characterization of Suspension #26.3 (NiCo SWNTs in D<sub>2</sub>O with 1 weight % TrisCh): (a) Absorbance spectrum, (b) AFM image of nanotubes spin coated onto silicon, (c & d) length and height distribution. The mean length and height were determined to  $(1100 \pm 380)$  nm and  $(1.3 \pm 0.3)$  nm.

Suspension 26 are NiCo nanotubes dispersed in D<sub>2</sub>O with 1 weight % TrisCh as surfactant. After size-exclusion chromatography Fraction 3 was used in the experiment. The fraction contains long individual SWNTs with a mean length and height of  $(1100 \pm 380)$  nm and  $(1.3 \pm 0.3)$  nm and a concentration of  $c \approx 70 \mu\text{g/ml}$ . Figure A.2 shows the absorbance spectra, AFM image and length and height distribution of Suspension #26.3.

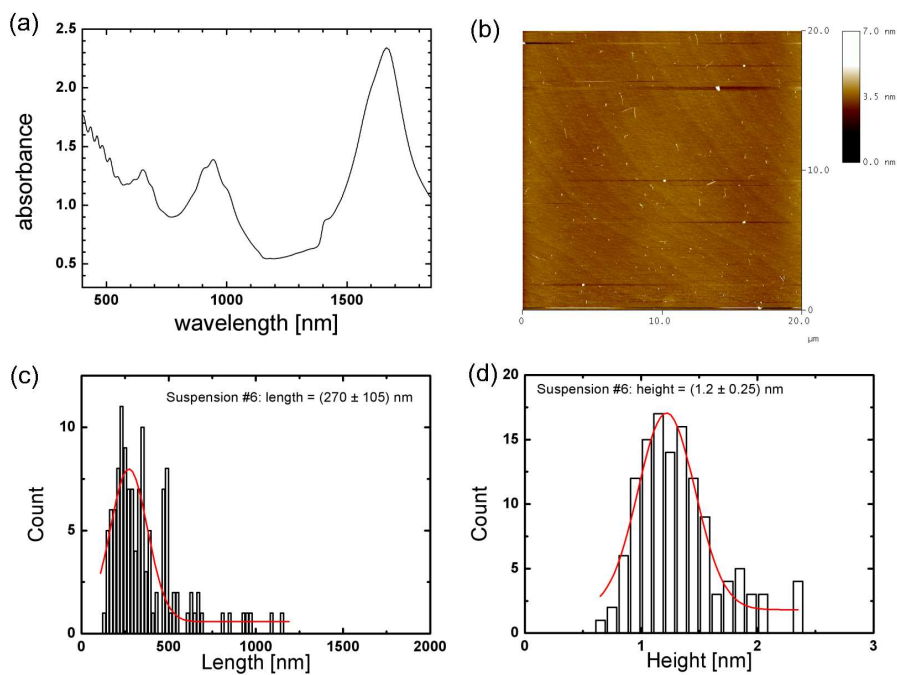


**Figure A.3:** Characterization of Suspension #6 (NiCo SWNTs in D<sub>2</sub>O with 1 weight % NaCh and Iodixanol): (a) Absorbance spectrum, (b) AFM image of nanotubes spin coated onto silicon, (c & d) length and height distribution. The mean length and height were determined to  $(270 \pm 105)$  nm and  $(1.2 \pm 0.25)$  nm.

Suspension #6 are NiCo nanotubes dispersed in D<sub>2</sub>O with 1 weight % NaCh and Iodixanol. The suspension was prepared with density gradient centrifugation. It has a very high concentration ( $c \approx 1040 \mu\text{g/ml}$ ) of short individual nanotubes with a mean length of  $(270 \pm 105)$  nm and a mean height of  $(1.2 \pm 0.25)$  nm. Figure A.3 shows the absorbance spectra, AFM image and length and height distribution of Suspension #6.



## B. Additional information on films of single-walled carbon nanotubes

### Morphology

SEM images of the samples 024B, 025A, 029B and 051A, whose impedance spectra were discussed in Section 3.1, are presented in the following.

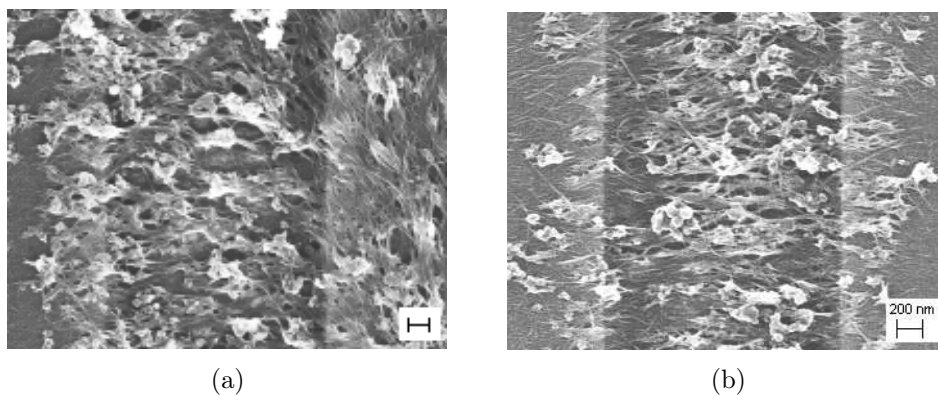


**Figure B.1:** SEM images of samples 024B (a) and 025A (b). Both samples were prepared from suspension # 26.3 (TrisCh) using the standard deposition parameters  $V_{pp} = 40$  V,  $t = 10$  min,  $t_{ON} = 10$  ms,  $\tau = 80$  ms and  $f = 10$  MHz. Scale bar is 200 nm in both pictures.

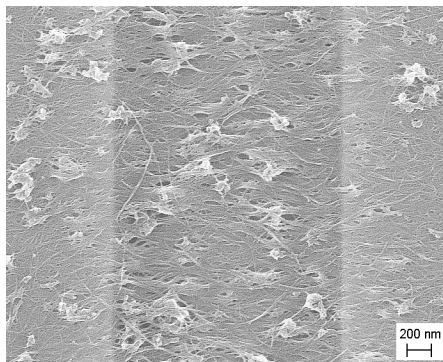


**Figure B.2:** SEM image of sample 029B. The sample was prepared using standard deposition parameters (see above) from suspension # 26.3 after additional centrifugation to remove agglomerated surfactant particles.

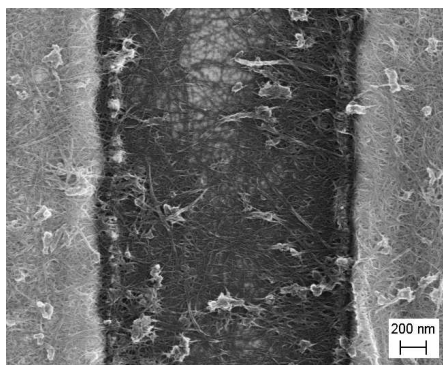


**Figure B.3:** SEM image of sample 051A. The sample was prepared from suspension # 26.3 (after additional centrifugation) with  $V_{pp} = 40$  V,  $f = 300$  kHz,  $t_{ON} = 0.5$  ms and  $\tau = 4$  ms. After only  $t \approx 5$  s, the deposition was stopped due to severe heat dissipation.

## Polarization dependent absorption and Raman spectra

The polarization dependent absorption measurements were repeated for samples prepared with SWNTs diluted in D<sub>2</sub>O with 1 weight % SDBS. Figures B.4 – B.7 show the spectra of length separated or centrifuged nanotubes, deposited with frequencies  $f = 10\text{--}80$  MHz and voltages  $V_{pp} = 40\text{--}80$  V.

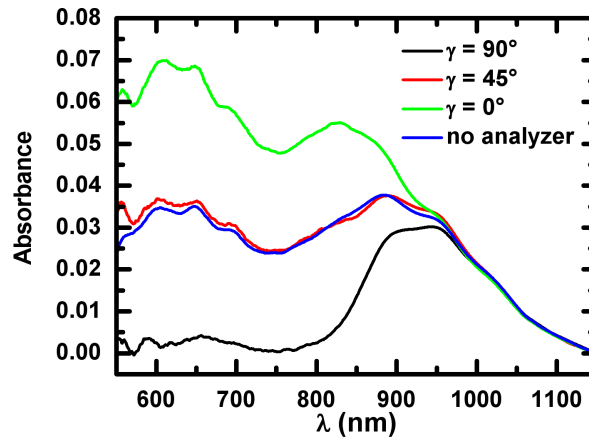


**Figure B.4:** Polarization dependent absorption spectra of length separated SWNTs in 1 weight % SDBS, deposited with  $f = 10$  MHz and  $V_{pp} = 40$  V. The raw data was smoothed and a linear background was subtracted. Metallic and small diameter semiconducting nanotubes are well aligned parallel to the electric field, while semiconducting nanotubes are randomly orientated. Taken from Ref. [84].

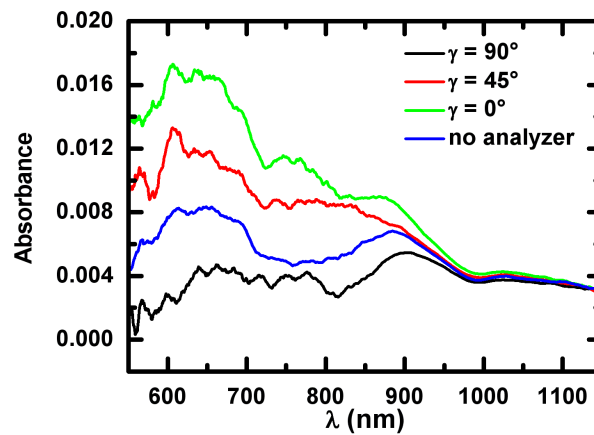


**Figure B.5:** Polarization dependent absorption spectra of length separated SWNTs in 1 weight % SDBS, deposited with  $f = 80$  MHz and  $V_{pp} = 40$  V. The raw data was smoothed and offset for better comparison. As reported earlier, the amount of deposited nanotubes reduces significantly high frequencies, resulting in a very low signal intensity and a relatively big measurement error. Taken from Ref. [84].

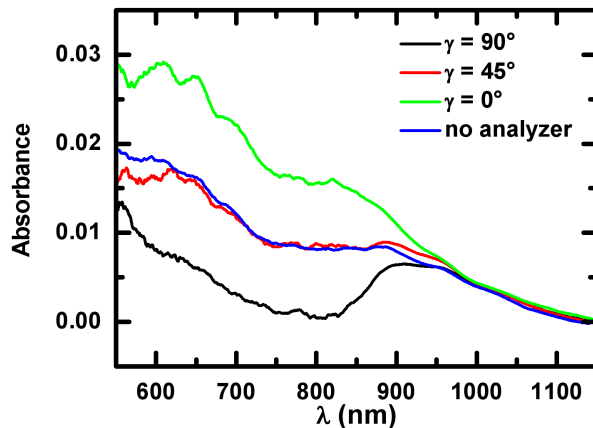


**Figure B.6:** Polarization dependent absorption spectra of length separated SWNTs in 1 weight % SDBS, deposited with  $f = 80$  MHz and  $V_{pp} = 80$  V. The raw data was smoothed and offset for better comparison. Taken from Ref. [84].

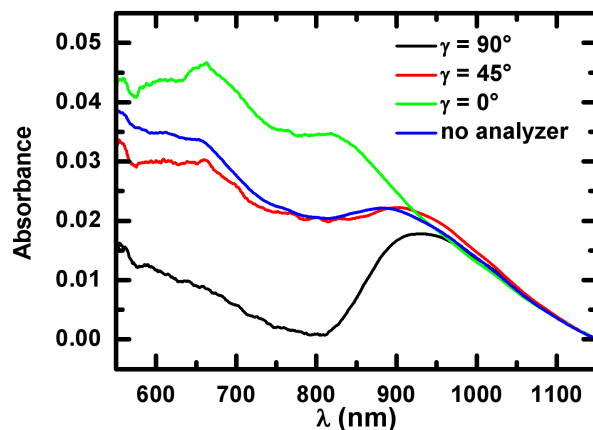


**Figure B.7:** Polarization dependent absorption spectra of centrifuged SWNTs in 1 weight % SDBS, deposited with  $f = 80$  MHz and  $V_{pp} = 80$  V. The raw data was smoothed and offset for better comparison. Taken from Ref. [84].

Additionally, Raman spectroscopy was done with a Dilor XY triple monochromator and an Ar-Kr laser for excitation. The spectra were recorded for two excitation laser lines, 514.5 nm and 647.1 nm. To study the polarization dependence, a  $\lambda/2$ -plate was used to rotate the polarization of the incident light with respect to the fixed orientation of the sample. The measurements were repeated for different spots on the sample.

A comparison of the Raman spectra measured between the electrodes for the two laser energies shows that the degree of alignment is much higher in the case of metallic nanotubes than for semiconducting nanotubes (Figures B.9 and B.8). The

axis of preferential orientation is parallel to the electric field during deposition. The spectra measured above the electrodes show equal intensity for parallel and perpendicular polarization.

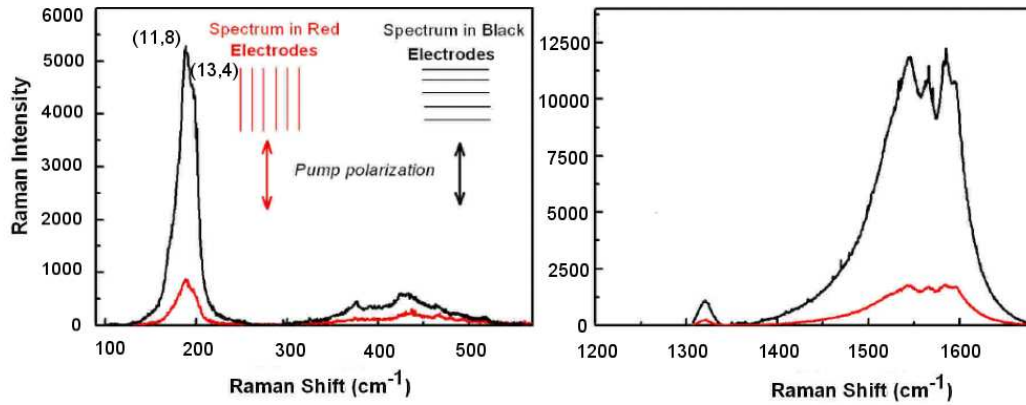


**Figure B.8:** Raman spectra measured with the 647.1 nm excitation line between the electrodes. At this wavelength primarily metallic SWNTs are excited. The intensity of the broad G mode (right plot) and the radial breathing mode (left plot) both decrease significantly, as the polarization of the incident light is changed from parallel to the electric field (black curves) to orthogonal to the electric field (red curves). This data is in agreement with the absorption measurements and shows that metallic SWNTs are well aligned in the samples. Taken from Ref. [84].

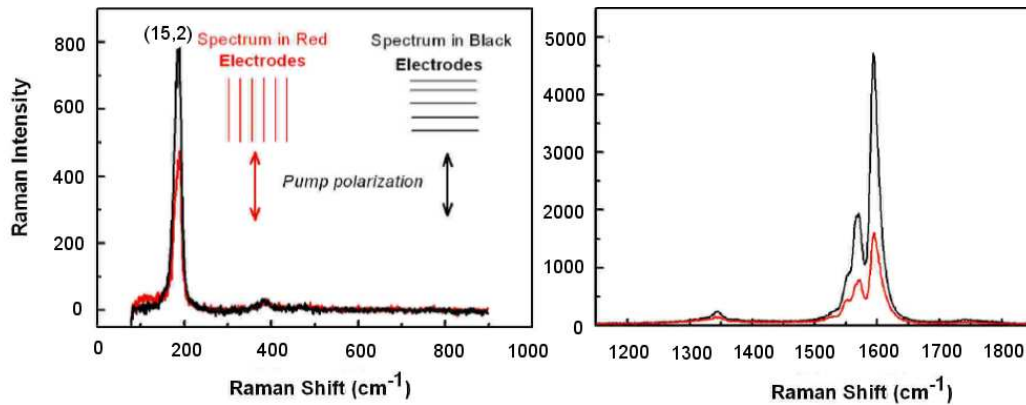


**Figure B.9:** Raman spectra measured with the 514.5 nm excitation line between the electrodes. With this wavelength primarily semiconducting SWNTs with a diameter of  $\sim 1.2$  nm are excited, which in the absorption spectrum in Figure 3.8 contribute to the absorbance around 880 nm. These semiconducting SWNTs show a weak alignment, which also manifests here in the polarization dependence of the intensities of the sharp  $G^+$  mode (right plot) and the radial breathing mode (left plot). However, the decrease in intensity is far less pronounced than in Figure B.8. Taken from Ref. [84].



## C. The effective dipole moment in a global coordinate system

Equation (3.3) states the expression of the effective dipole moment of an ellipsoidal particle in a global coordinate system. This expression will be derived in the following.

As shown in Section 2.2.1, the effective dipole moment of an ellipsoidal particle in the particle's coordinate system is given by

$$\vec{p}_{\text{eff,particle}} = \begin{pmatrix} \alpha_{\parallel} & 0 & 0 \\ 0 & \alpha_{\perp} & 0 \\ 0 & 0 & \alpha_{\perp} \end{pmatrix} \begin{pmatrix} E_{0,1} \\ E_{0,2} \\ E_{0,3} \end{pmatrix} \quad (\text{C.1})$$

with  $\alpha_{ii} = \frac{4\pi abc}{3} \varepsilon_{\ell} \Re \left( \frac{\varepsilon_{\text{p}}^* - \varepsilon_{\ell}^*}{\varepsilon_{\ell}^* + (\varepsilon_{\text{p}}^* - \varepsilon_{\ell}) L_i} \right)$

To transfer this into a global coordinate system a coordinate transformation of the form

$$\vec{p}_{\text{eff,global}} = R^T \vec{p}_{\text{eff,particle}} R \quad (\text{C.2})$$

with rotation matrix  $R$  is necessary. With Equation (C.1) it follows

$$\begin{pmatrix} \alpha_{xx} & \alpha_{xy} & \alpha_{xz} \\ \alpha_{yx} & \alpha_{yy} & \alpha_{yz} \\ \alpha_{zx} & \alpha_{zy} & \alpha_{zz} \end{pmatrix} = R^T \begin{pmatrix} \alpha_{\parallel} & 0 & 0 \\ 0 & \alpha_{\perp} & 0 \\ 0 & 0 & \alpha_{\perp} \end{pmatrix} R. \quad (\text{C.3})$$

Assuming an ellipsoidal particle ( $a \gg b = c$ ) with arbitrary orientation with respect to the fixed reference frame ( $x, y, z$ -coordinates), the particle's coordinate system with axes 1, 2, 3 is chosen such that the 1-axis is parallel to the long axis of the rod-like particle. Without loss of generality, the origin of both coordinate systems are assumed to coincide as depicted in Figure 3.9. Let  $\varphi$  denote the angle between the global  $x$ -axis and the projection of the 1-axis onto the  $x$ - $y$ -plane and  $\theta$  be the angle between the  $z$ -axis and the 1-axis. This choice then corresponds to the common spherical coordinate system with  $0 \leq \varphi < 2\pi$  as azimuthal angle and  $0 \leq \theta < \pi$  as polar angle. The rotational matrix transforming from the cartesian to the spherical coordinate system is defined as

$$R = \begin{pmatrix} \cos \varphi \sin \theta & \sin \varphi \sin \theta & \cos \theta \\ \cos \varphi \cos \theta & \sin \varphi \cos \theta & -\sin \theta \\ -\sin \varphi & \cos \varphi & 0 \end{pmatrix}. \quad (\text{C.4})$$

With the definition of  $s_\varphi \equiv \sin \varphi$ ,  $c_\varphi \equiv \cos \varphi$ ,  $s_\theta \equiv \sin \theta$ ,  $c_\theta \equiv \cos \theta$  and  $\Delta_\alpha \equiv \alpha_{\parallel} - \alpha_{\perp}$ , it follows

$$\begin{aligned} & \begin{pmatrix} \alpha_{xx} & \alpha_{xy} & \alpha_{xz} \\ \alpha_{yx} & \alpha_{yy} & \alpha_{yz} \\ \alpha_{zx} & \alpha_{zy} & \alpha_{zz} \end{pmatrix} \\ &= \begin{pmatrix} c_\varphi s_\theta & c_\varphi c_\theta & -s_\varphi \\ s_\varphi s_\theta & s_\varphi c_\theta & c_\varphi \\ c_\theta & -s_\theta & 0 \end{pmatrix} \cdot \begin{pmatrix} \alpha_{\parallel} & 0 & 0 \\ 0 & \alpha_{\perp} & 0 \\ 0 & 0 & \alpha_{\perp} \end{pmatrix} \cdot \begin{pmatrix} c_\varphi s_\theta & s_\varphi s_\theta & c_\theta \\ c_\varphi c_\theta & s_\varphi c_\theta & -s_\theta \\ -s_\varphi & c_\varphi & 0 \end{pmatrix} \\ &= \begin{pmatrix} c_\varphi s_\theta & c_\varphi c_\theta & -s_\varphi \\ s_\varphi s_\theta & s_\varphi c_\theta & c_\varphi \\ c_\theta & -s_\theta & 0 \end{pmatrix} \cdot \begin{pmatrix} \alpha_{\parallel} c_\varphi s_\theta & \alpha_{\parallel} s_\varphi s_\theta & \alpha_{\parallel} c_\theta \\ \alpha_{\perp} c_\varphi c_\theta & \alpha_{\perp} s_\varphi c_\theta & -\alpha_{\perp} s_\theta \\ -\alpha_{\perp} s_\varphi & \alpha_{\perp} c_\varphi & 0 \end{pmatrix} \\ &= \begin{pmatrix} \alpha_{\perp} s_\varphi^2 + c_\varphi^2 (\alpha_{\parallel} - c_\theta^2 \Delta_\alpha) & \Delta_\alpha s_\varphi c_\varphi s_\theta^2 & \Delta_\alpha c_\varphi c_\theta s_\theta \\ \Delta_\alpha s_\varphi c_\varphi s^2 \theta & \alpha_{\perp} s_\varphi^2 + c_\varphi^2 (\alpha_{\parallel} - c_\theta^2 \Delta_\alpha) & \Delta_\alpha s_\varphi c_\theta s_\theta \\ \Delta_\alpha c_\varphi c_\theta s_\theta & \Delta_\alpha s_\varphi c_\theta s_\theta & \alpha_{\parallel} c_\theta^2 + \alpha_{\perp} s_\theta^2 \end{pmatrix}. \end{aligned}$$

The effective dipole moment in the global coordinate system is then given by

$$\vec{p}_{\text{eff,global}} = \begin{pmatrix} \alpha_{xx} & \alpha_{xy} & \alpha_{xz} \\ \alpha_{yx} & \alpha_{yy} & \alpha_{yz} \\ \alpha_{zx} & \alpha_{zy} & \alpha_{zz} \end{pmatrix} \cdot \begin{pmatrix} E_{0,x} \\ E_{0,y} \\ E_{0,z} \end{pmatrix}. \quad (\text{C.5})$$

## D. Additional information on the field-dependent absorption spectra

### Irreversible changes of the field-dependent absorption spectra

In the experiments described in Chapter 5 the full relaxation of the system after turning off the AC voltage was required. Figure D.1 shows an example case in which the application of a high voltage caused an irreversible change in the absorbance which led to the abortion of this particular experiment.

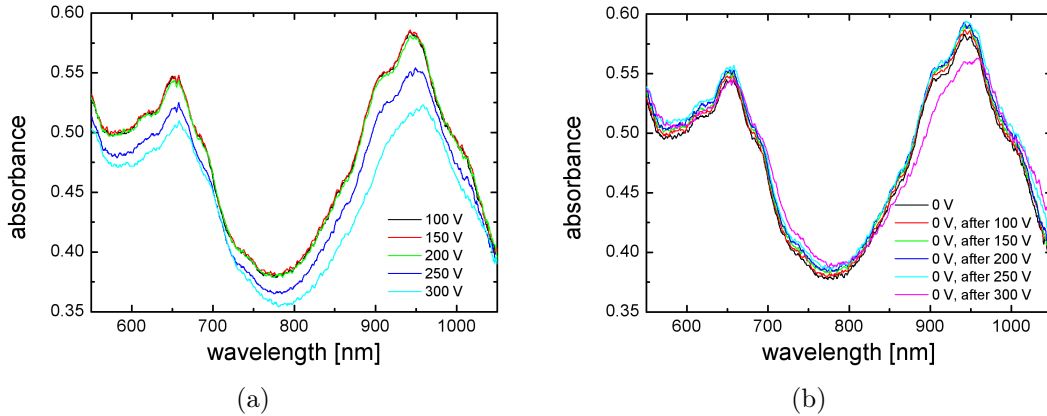


**Figure D.1:** Absorbance spectra of dispersed nanotubes after application of an AC voltage  $V_{pp}$  with a frequency  $f = 70$  MHz for  $t = 1$  min (a) and after a relaxation with  $V_{pp} = 0$  for  $t = 1$  min (b). The application of  $V_{pp} = 250$  V causes a strong downshift of the absorbance; however, the system relaxes into the original state when the voltage is switched off. Further increase of the voltage to  $V_{pp} = 300$  V results in an even more pronounced downshift and a smearing of the M1 and S2 bands. As these are irreversible changes, the experiment was aborted thereafter.

### Derivation of the relation between the relative absorbance and the applied voltage as given by Equation (5.2)

In the discussion of the polarization dependent absorption spectra (see Section 3.2), the alignment of carbon nanotubes deposited on a sample surface was analyzed. In this case it was sufficient to restrict the angles which characterize the

orientation of the nanotube and the electric field to the surface plane, in which also the orientation of the analyzer is defined. In the case of the alignment of dispersed nanotubes, this is not possible.

The orientation of a nanotube in the global coordinate system is described by its azimuthal angle  $\varphi$  and polar angle  $\theta$ :

$$\vec{r}_{\text{CNT}} = \begin{pmatrix} \cos \varphi \sin \theta \\ \sin \varphi \sin \theta \\ \cos \theta \end{pmatrix}, \quad (\text{D.1})$$

as illustrated in Figure 3.9. The vector of the electric field,  $\vec{r}_{\text{E}}$ , and the incident light,  $\vec{r}_{\text{light}}$ , are given by

$$\vec{r}_{\text{E}} = \begin{pmatrix} 0 \\ 0 \\ 1 \end{pmatrix} \quad \text{and} \quad \vec{r}_{\text{light}} = \begin{pmatrix} \cos \varphi' \\ \sin \varphi' \\ 0 \end{pmatrix}. \quad (\text{D.2})$$

with  $0 \leq \varphi' \leq 2\pi$ . Note, that these are unit vectors.

Let  $\beta$  denote the angle between the carbon nanotube and the incident light;  $\beta$  then determines the absorbance. It can be calculated from the scalar product of  $\vec{r}_{\text{CNT}}$  and  $\vec{r}_{\text{light}}$  as

$$\begin{aligned} \cos \beta &= \vec{r}_{\text{CNT}} \cdot \vec{r}_{\text{light}} \\ &= (\cos \varphi' \cos \varphi + \sin \varphi' \sin \varphi) \sin \theta \\ &= \cos(\varphi' - \varphi) \sin \theta. \end{aligned} \quad (\text{D.3})$$

Using Equations (3.7) and (3.10), the absorbance  $Abs(V_{\text{pp}})$  is given by

$$\begin{aligned} Abs(V_{\text{pp}}) &= \int_0^\pi \sin \theta \, d\theta \int_0^{2\pi} d\varphi' \int_0^{2\pi} d\varphi A_0 f(\theta, U_0) \cos^2 \beta \\ &= A_0 \int_0^{2\pi} d\varphi \int_0^{2\pi} d\varphi' \cos^2(\varphi' - \varphi) \int_0^\pi d\theta f(\theta, U_0) \sin^3 \theta. \end{aligned} \quad (\text{D.4})$$

Here,  $A_0$  is a constant which will be specified later. Integration over  $\varphi$  and  $\varphi'$  yields a factor  $2\pi^2$ . To calculate the integral over  $\theta$ , the exp-function in  $f(\theta, U_0)$  is expanded in a Taylor series, of which only the first and second terms are used. Then

$$\begin{aligned} Abs(V_{\text{pp}}) &= 2\pi^2 A_0 \frac{\int_0^\pi d\theta \left[ \sin^3 \theta + \frac{|U_0|}{k_B T} \cos^2 \theta \sin^3 \theta \right]}{\int_0^\pi d\theta \left[ 1 + \frac{|U_0|}{k_B T} \cos^2 \theta \right]} \\ &= \frac{8}{3} \pi^2 A_0 \frac{1 + \frac{|U_0|}{k_B T} \frac{1}{5}}{1 + \frac{|U_0|}{k_B T} \frac{1}{2}}. \end{aligned} \quad (\text{D.5})$$

In the case of zero applied voltage, the exp-function reduces to 1 and it follows

$$Abs(0\text{ V}) = 2\pi^2 A_0 \frac{\int_0^\pi d\theta \sin^3 \theta}{\int_0^\pi d\theta} = \frac{8}{3}\pi A_0. \quad (\text{D.6})$$

Hereby,  $A_0$  is determined. The relative absorbance can now be calculated as

$$\frac{Abs(V_{pp})}{Abs(0\text{ V})} = \frac{1 + \frac{|U_0|}{k_B T} \frac{1}{5}}{1 + \frac{|U_0|}{k_B T} \frac{1}{2}}. \quad (\text{D.7})$$

Comparison with Equation (5.2) shows, that

$$c_1 = \frac{|U_0|}{k_B T} \frac{1}{V_{pp}^2} = \frac{1}{4d^2} (\alpha_{||} - \alpha_{\perp}) \frac{1}{k_B T}, \quad (\text{D.8})$$

where  $d$  corresponds to the distance between the electrodes.

### Results of the fit

In the following the plots of Figure 5.3 are presented individually and together with their fits (dotted lines) according to Equation (5.2).

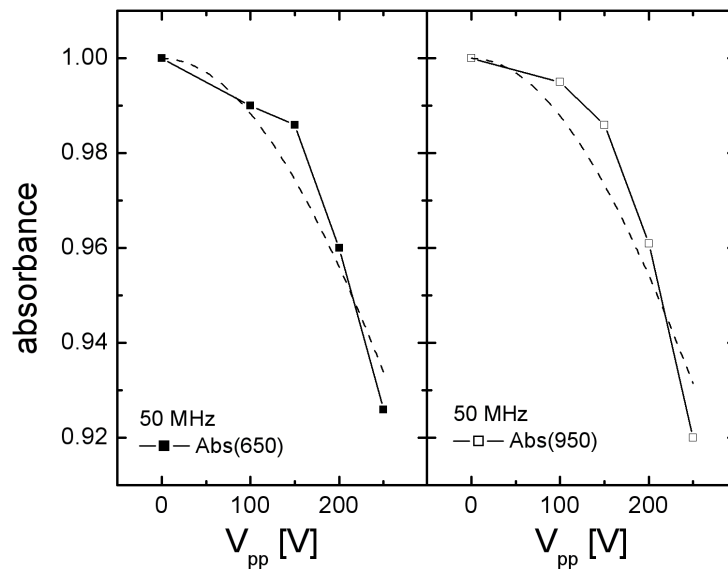


**Figure D.2:** Evolution of the relative absorbance with applied voltage for  $f = 50$  MHz.

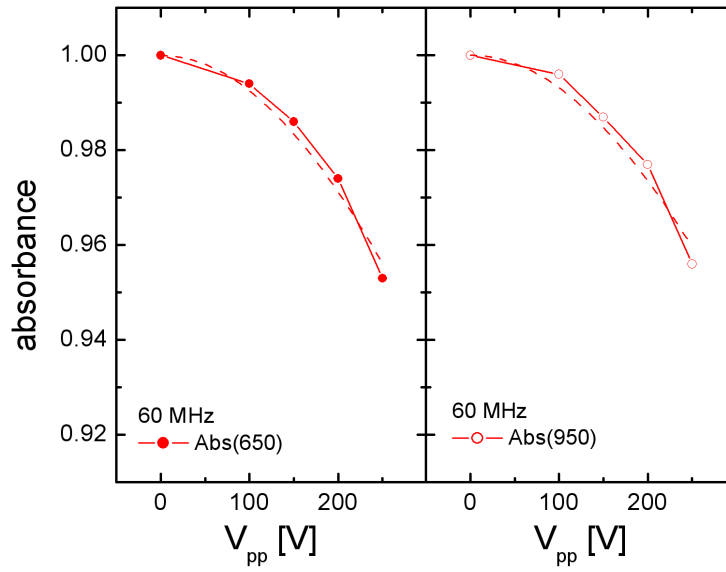


**Figure D.3:** Evolution of the relative absorbance with applied voltage for  $f = 60$  MHz.

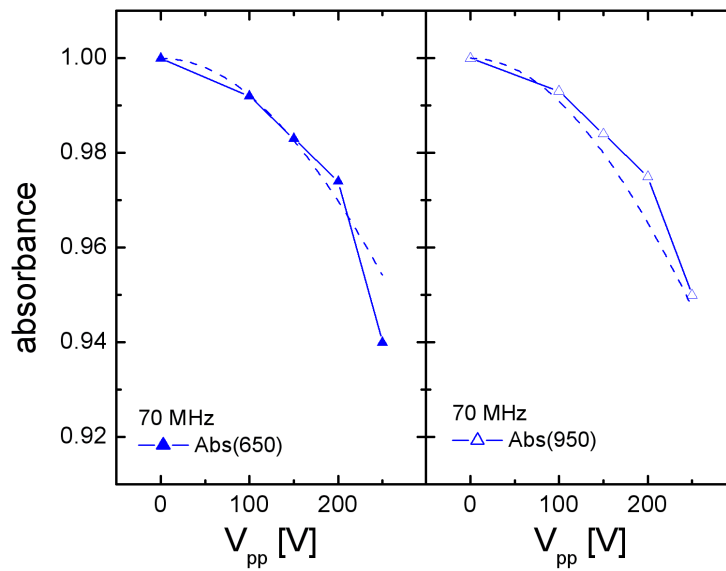


**Figure D.4:** Evolution of the relative absorbance with applied voltage for  $f = 70$  MHz.

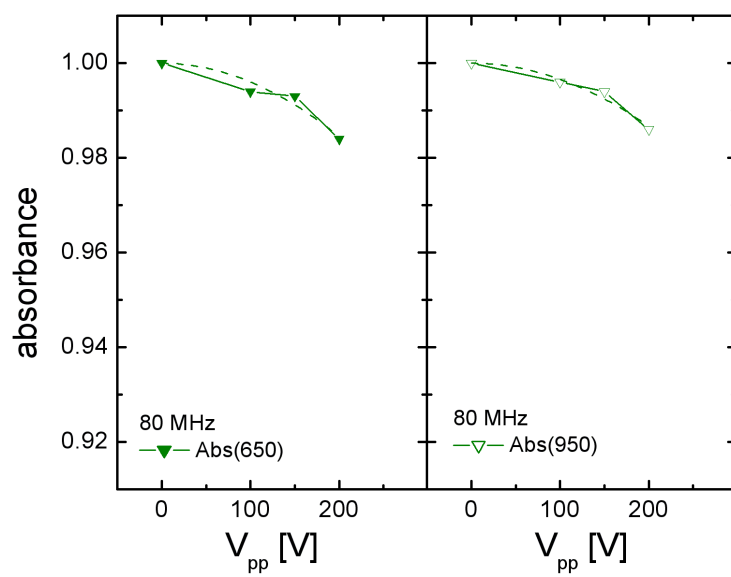


**Figure D.5:** Evolution of the relative absorbance with applied voltage for  $f = 80$  MHz.



## E. Electrophoretic mobility of SWNTs

As stated in the introductory part of Chapter 6, a dielectrophoretic separation of metallic and semiconducting nanotubes in an electrodeless dielectrophoresis setup is expected to succeed only if the dielectrophoretic and the driving force are superimposed and adjusted precisely. When using an electrophoretic force, the polarity of the DC voltage has to be chosen such that the electrophoresis produces a nanotube movement from the CNT side into the soap side. In the following, the electrophoretic mobility of single-walled carbon nanotubes and its dependency on the solution parameters (surfactant type and concentration and nanotube concentration) is examined.

The electrophoretic mobility of single-walled carbon nanotubes was measured using Phase Analysis Light Scattering (PALS) with a Brookhaven ZetaPALS. The method is based on the detection of light scattered by particles which move under an applied electric field. A detailed description of this measurement method is given in Reference [121].

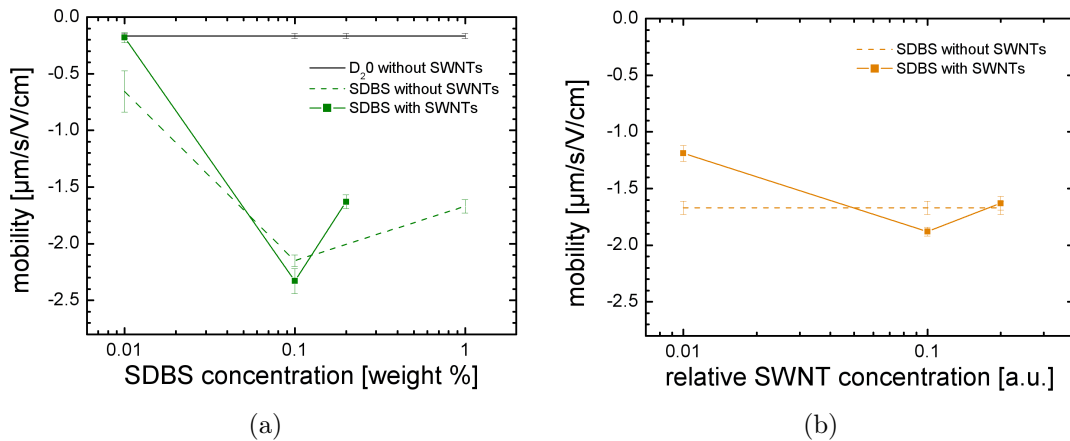


**Figure E.1:** Electrophoretic mobility of SWNTs dispersed in D<sub>2</sub>O and SDBS. In (a) the starting solution is gradually diluted with D<sub>2</sub>O, i. e. the SDBS content as well as the nanotube concentration decreases, and in (b) the nanotube concentration changes due to the addition of pure SDBS solution (1 weight %). In both experiments the electrophoretic mobility does not depend significantly on the presence (or the concentration) of nanotubes in the suspension, but varies strongly with the SDBS content.

Figure E.1 shows the results of measurements on short single-walled carbon nanotubes dispersed in  $D_2O$  with 1 weight % SBDS. In Figure E.1(a) the starting suspensions was gradually diluted by the addition of  $D_2O$  (full green curve), i. e. both the SBDS content and the nanotube concentration decrease successively. The comparison with the measurements on pure  $D_2O$  (black curve, revealing a systematic offset) as well as  $D_2O$  with the according concentration of SBDS (dashed green curve) show no significant change between the mobility with nanotubes compared to the case of pure SBDS. Irrespective of the presence of nanotubes in the suspension, the mobility clearly depends on the SBDS content and features a maximum at 0.1 weight %. These observations can be explained by the fact that SBDS efficiently builds micelles above the critical micelle concentration (CMC), which is  $\approx 0.1$  weight%. These large micelles with an aggregation number—mean number of molecules in the micelle—of 61 [122] dominate the measurement.

In Figure E.1(b), the starting suspensions is diluted by adding  $D_2O$  with 1 weight % SBDS (full orange curve). As expected according to the above discussion, the mobility does not depend significantly on the nanotube concentration and is comparable to the results obtained for pure SBDS suspension (dashed orange curve).

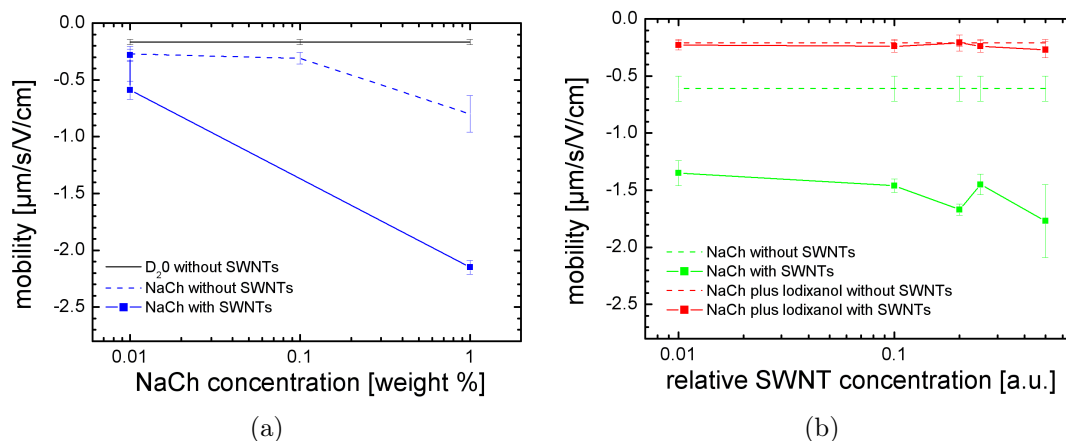


**Figure E.2:** Electrophoretic mobility of SWNTs dispersed in  $D_2O$  and NaCh. A comparison between the mobility measured for pure NaCh and for nanotubes dispersed in NaCh solution shows a significant increase in the latter case. According to the data presented in (a), the mobility also increases with the NaCh concentration, but shows only a weak dependence on the nanotube concentration (b). The higher viscosity of the Iodixanol sample leads to a suppression of the electrophoretic mobility.

In Figure E.2 the results of an equivalent study on short single-walled carbon nanotubes dispersed in  $D_2O$  with 1 weight % NaCh are displayed. A comparison between the pure NaCh solution (dashed blue curve in Figure E.2(a)) and the starting suspension (full blue curve), both gradually diluted with  $D_2O$ , shows a distinct increase of the measured electrophoretic mobility in the presence of

---

nanotubes. Additionally, the data for pure NaCh solution reveal a dependence on the stage of dilution. These observations can again be explained by the properties of the surfactant micelles. Unlike in the case of SDBS, NaCh does not form large micelles in the absence of nanotubes; the aggregation number of 2–3 [123] indicates very small micelles in pure NaCh solution. For small NaCh concentration ( $\leq 0.1$  weight %), the measured mobility is close to that of pure D<sub>2</sub>O (black curve); for large concentration, an increased mobility is detected, but the error is relatively large, indicating a low signal. In the presence of carbon nanotubes, the size of the micelles changes significantly and the micelles surrounding the nanotubes dominate the measurement. The mobility which is measured under these conditions truly represents the mobility of the nanotube-micelle compound.

Under variation of the SWNT concentration in Figure E.2(b), a similar increase is observed when comparing the mobility with and without nanotubes in suspension (full and dashed light-green curves, respectively). The data also shows a certain dependence on the nanotube concentration, but the variation is within the error range and therefore not significant, consistent with the expectations. An additional measurement on nanotubes dispersed in D<sub>2</sub>O with NaCh and Iodixanol—such suspensions are used for the density gradient centrifugation—reveals a severe suppression of the electrophoretic mobility, probably due to the increased viscosity of the suspension. In this case the change of the mobility due to the presence of nanotubes (full versus dotted red curve) is smaller than the accuracy of the measurement

The most important conclusion from these measurements is the negative surface charge of single-walled carbon nanotubes surrounded by NaCh micelles. Under electrophoresis the nanotube/micelle structures will consequently move in the direction opposite to the external field. The different trends observed in the case of SDBS and NaCh, namely the negligible change in the electrophoretic mobility in the presence of SWNTs as compared to pure SDBS solution and the enhancement of the mobility due to the presence of nanotubes in NaCh, are based upon the different sizes of the surfactant molecules and differences in the process of micelle-formation with or without nanotube for the two surfactant types. The increased viscosity in the presence of Iodixanol suppresses the mobility of the nanotube/micelle compound to a large extent.



# List of Figures

|       |  |    |
|-------|--|----|
| 2.1.  | The unit cell and the Brillouin zone of 2d graphene . . . . .  | 7  |
| 2.2.  | Geometrical construction of a SWNT from graphene . . . . .   | 9  |
| 2.3.  | Brillouin zone of SWNTs . . . . .  | 10 |
| 2.4.  | Energy dispersion of graphene . . . . .  | 11 |
| 2.5.  | Zone-folding approximation . . . . .   | 11 |
| 2.6.  | Primary and secondary gaps in carbon nanotubes . . . . .   | 13 |
| 2.7.  | Kataura plot . . . . .   | 15 |
| 2.8.  | Photoluminescence in single-walled carbon nanotubes . . . . .  | 17 |
| 2.9.  | Resonant Raman spectra of individual SWNTs . . . . .   | 19 |
| 2.10. | Setup for PLV preparation of SWNTs . . . . .   | 20 |
| 2.11. | Chemical structures of surfactants . . . . .   | 21 |
| 2.12. | Formation of surfactant micelles around SWNTs . . . . .  | 22 |
| 2.13. | Typical absorbance spectrum of PLV-SWNTs dispersed in NaCh .   | 23 |
| 2.14. | SWNT assembly by dielectrophoresis . . . . .   | 26 |
| 2.15. | Electronic type specific separation of SWNTs . . . . .   | 27 |
| 2.16. | Thin films of SWNTs and their optical absorbance spectra . . . .   | 29 |
| 2.17. | finite element discretization in 2d . . . . .  | 31 |
| 2.18. | Creating a three-dimensional domain in FlexPDE . . . . .   | 34 |
|       |  |    |
| 3.1.  | Schematic of the interdigitated electrode structure . . . . .  | 38 |
| 3.2.  | Morphology of nanotubes deposited on Al and Au electrodes . . .  | 40 |
| 3.3.  | Impedance spectra of Al and Au electrode structures . . . . .  | 41 |
| 3.4.  | Impedance spectra in the high-frequency range . . . . .  | 42 |
| 3.5.  | Equivalent circuit for interdigitated electrode structures . . . . .                                     | 43 |
| 3.6.  | SEM and AFM images of a SWNT film on interdigitated electrodes   | 44 |
| 3.7.  | Setup for polarization dependent absorption measurements . . . .   | 45 |
| 3.8.  | Absorbance spectra for three settings of the analyzer . . . . .  | 46 |
| 3.9.  | Cartesian and spherical coordinates . . . . .  | 48 |
| 3.10. | Nematic order parameter $S$ for nanotubes in AC electric fields . .                                      | 52 |
|       |  |    |
| 4.1.  | Dielectrophoretic force fields for a type $A$ structure on insulating quartz substrate . . . . .         | 56 |
| 4.2.  | Dielectrophoretic force fields for a type $B$ structure on conducting p-type silicon substrate . . . . . | 57 |

|       |   |     |
|-------|---|-----|
| 4.3.  | Schematic of the high-density array of single-tube devices . . . . .      | 60  |
| 4.4.  | SEM and AFM image of the array of single tube devices . . . . .           | 61  |
| 4.5.  | Impedance spectroscopy measurements of single tube devices . . .          | 61  |
| 4.6.  | Potential distribution near the electrodes of single tube devices . .     | 64  |
| 4.7.  | Dielectrophoretic force fields near the electrodes of single tube devices | 65  |
| 4.8.  | Potential distribution in an interdigitated electrode array . . . . .     | 66  |
| 4.9.  | Dielectrophoretic force fields in an interdigitated electrode array .     | 67  |
| 4.10. | Voltage Contrast-SEM images of SWNT devices . . . . .                     | 69  |
| 4.11. | Model for the SWNT device simulation . . . . .                            | 71  |
| 4.12. | Potential and electric field near floating and grounded electrodes .      | 72  |
| 4.13. | Evolution of the potential distribution in a SWNT device . . . . .        | 73  |
|       |   |     |
| 5.1.  | Experimental setup to measure the alignment of dispersed SWNTs            | 76  |
| 5.2.  | Impedance spectrum of the test volume . . . . .                           | 78  |
| 5.3.  | Field-dependent absorbance spectra of dispersed nanotubes . . . .         | 79  |
| 5.4.  | Field-dependent changes of the nanotube absorbance . . . . .              | 80  |
| 5.5.  | Evolution of the relative absorbance with the applied voltage . . .       | 80  |
|       |   |     |
| 6.1.  | Electric field distribution in different pore geometries . . . . .        | 84  |
| 6.2.  | Schematic of the electrical double layer . . . . .                        | 86  |
| 6.3.  | Photograph of the DEP cell . . . . .                                      | 88  |
| 6.4.  | Circuit diagram for transport of SWNTs through nanopores . . .            | 89  |
| 6.5.  | Impedance spectra of the DEP cell filled with various suspensions         | 90  |
| 6.6.  | Schematic of electroosmosis in a micro channel . . . . .                  | 92  |
| 6.7.  | Absorbance spectrum measured after a DC experiment . . . . .              | 93  |
| 6.8.  | Absorbance spectrum measured after a comparative DC experiment            | 93  |
| 6.9.  | Absorbance spectra measured after AC experiments . . . . .                | 95  |
| 6.10. | Normalized absorbance spectra measured after AC experiments .             | 96  |
|       |   |     |
| A.1.  | Characterization of Suspension #24.2 and 24.4 . . . . .                   | 103 |
| A.2.  | Characterization of Suspension #26.3 . . . . .                            | 104 |
| A.3.  | Characterization of Suspension #6 . . . . .                               | 105 |
|       |   |     |
| B.1.  | SEM images of samples 024B and 025A . . . . .                             | 107 |
| B.2.  | SEM image of sample 029B . . . . .  | 108 |
| B.3.  | SEM image of sample 051A . . . . .  | 108 |
| B.4.  | Polarization dependent absorption spectra . . . . .                       | 109 |
| B.5.  | Polarization dependent absorption spectra . . . . .                       | 109 |
| B.6.  | Polarization dependent absorption spectra . . . . .                       | 110 |
| B.7.  | Polarization dependent absorption spectra . . . . .                       | 110 |
| B.8.  | Raman spectra measured with the 647.1 nm excitation line . . . .          | 111 |
| B.9.  | Raman spectra measured with the 514.5 nm excitation line . . . .          | 111 |
|       |   |     |
| D.1.  | Irreversible changes of the field-dependent absorbance . . . . .          | 115 |

---

|   |     |
|---|-----|
| D.2. Evolution of the relative absorbance for $f = 50$ MHz . . . . .            | 117 |
| D.3. Evolution of the relative absorbance for $f = 60$ MHz . . . . .            | 118 |
| D.4. Evolution of the relative absorbance for $f = 70$ MHz . . . . .            | 118 |
| D.5. Evolution of the relative absorbance for $f = 80$ MHz . . . . .            | 119 |
| E.1. Electrophoretic mobility of SWNTs dispersed in D <sub>2</sub> O and SDBS . | 121 |
| E.2. Electrophoretic mobility of SWNTs dispersed in D <sub>2</sub> O and NaCh . | 122 |



# Bibliography

- [1] G. Binnig, H. Rohrer, C. Gerber, and E. Weibel, Tunneling through a controllable vacuum gap, *Applied Physical Letters* **40**, 178–180 (1982).
- [2] G. Binnig, C. F. Quate, and C. Gerber, Atomic Force Microscope, *Physical Review Letters* **56**, 930–933 (1986).
- [3] H. W. Kroto, J. R. Heath, S. C. O’Brien, R. F. Curl, and R. E. Smalley, C60: Buckminsterfullerene, *Nature* **318**, 162–163 (1985).
- [4] S. Iijima, Helical microtubules of graphitic carbon, *Nature* **354**, 56–58 (1991).
- [5] S. Iijima and T. Ichihashi, Single-shell carbon nanotubes of 1-nm diameter, *Nature* **363**, 603–605 (1993).
- [6] A. Jorio, M. S. Dresselhaus, and G. Dresselhaus, editors, *Carbon Nanotubes: Advanced Topics in the Synthesis, Structure, Properties and Applications*, Topics in Applied Physics, Springer, 2008.
- [7] S. Reich, C. Thomsen, and J. Maultzsch, *Carbon Nanotubes, Basic Concepts and Physical Properties*, Wiley-VCH Verlag GmbH, Weinheim, 2004.
- [8] P. L. McEuen, Single-wall carbon nanotube, *Physics World* **13**, 31–36 (2000).
- [9] W. A. de Heer, A. Chatelain, and D. Ugarte, A carbon nanotube field-emission electron source, *Science* **270**, 1179–1180 (1995).
- [10] R. H. Baughman, A. A. Zakhidov, and W. A. de Heer, Carbon nanotubes – the route towards applications, *Science* **297**, 787–792 (2002).
- [11] R. Krupke, F. Hennrich, H. v. Löhneysen, and M. M. Kappes, Separation of metallic from semiconducting single-walled carbon nanotubes, *Science* **301**, 344–347 (2003).
- [12] R. Krupke, F. Hennrich, H. B. Weber, M. M. Kappes, and H. v. Löhneysen, Simultaneous deposition of metallic bundles of single-walled carbon nanotubes using AC-dielectrophoresis, *Nano Letters* **3**, 1019–1023 (2003).

- 
- [13] H. A. Pohl, *Dielectrophoresis*, Cambridge University Press, Cambridge, UK, 1978.
- [14] H. A. Pohl and I. Hawk, Separation of living and dead cells by dielectrophoresis, *Science* **162**, 647–649 (1966).
- [15] M. Washizu and O. Kurosawa, Electrostatic manipulation of DNA in microfabricated structures, *IEEE Transactions on Industry Applications* **26**, 1165–1172 (1990).
- [16] M. Washizu, S. Suzuki, O. Kurosawa, T. Nishizaka, and T. Shinohara, Molecular dielectrophoresis of biopolymers, *IEEE Transactions on Industry Applications* **30**, 835–842 (1994).
- [17] T. Müller, A. Gerardino, T. Schnelle, S. G. Shirley, F. Bordoni, G. DeGasperis, R. Leoni, and G. Fuhr, Trapping of micrometre and sub-micrometre particles by high-frequency electric fields and hydrodynamic forces, *Journal of Physics D: Applied Physics* **29**, 340–349 (1996).
- [18] M. P. Hughes and H. Morgan, Dielectrophoretic manipulation of single sub-micron scale bioparticle, *Journal of Physics D: Applied Physics* **31**, 2205–2210 (1998).
- [19] H. Morgan, M. P. Hughes, and N. G. Green, Separation of sub-micron particles by dielectrophoresis, *Biophysical Journal* **77**, 516–525 (1999).
- [20] N. G. Green and H. Morgan, Dielectrophoretic separation of nano-particles, *Journal of Physics D: Applied Physics* **30**, L41–44 (1997).
- [21] M. P. Hughes, AC electrokinetics: applications for nanotechnology, *Nanotechnology* **11**, 124–132 (2000).
- [22] R. Krupke, F. Hennrich, H. B. Weber, D. Beckmann, O. Hampe, S. Malik, M. M. Kappes, and H. v. Löhneysen, Contacting single bundles of carbon nanotubes with alternating electric fields, *Applied Physics A* **76**, 397–400 (2003).
- [23] J. Chung, K.-H. Lee, J. Lee, and R. S. Ruoff, Toward large-scale integration of carbon nanotubes, *Langmuir* **20**, 3011–3017 (2004).
- [24] A. Vijayaraghavan, S. Blatt, D. Weissenberger, M. Oron-Carl, F. Hennrich, D. Gerthsen, H. Hahn, and R. Krupke, Ultra-large-scale directed assembly of single-walled carbon nanotube devices, *Nano Letters* **7**, 1556–1560 (2007).
- [25] R. Krupke, F. Hennrich, M. M. Kappes, and H. v. Löhneysen, Surface conductance induced dielectrophoresis of semiconducting single-walled carbon nanotubes, *Nano Letters* **4**, 1395–1399 (2004).

- [26] R. Krupke, S. Linden, M. Rapp, and F. Hennrich, Thin films of metallic carbon nanotubes prepared by dielectrophoresis, *Advanced Materials* **18**, 1468–1470 (2006).
- [27] T. Lutz and K. J. Donovan, Macroscopic scale separation of metallic and semiconducting nanotubes by dielectrophoresis, *Carbon* **43**, 2508–2513 (2005).
- [28] D. S. Lee, D. W. Kim, H. S. Kim, S. W. Lee, S. H. Jhang, Y. W. Park, and E. E. B. Campbell, Extraction of semiconducting CNTs by repeated dielectrophoretic filtering, *Applied Physics A* **80**, 5–8 (2005).
- [29] M. Mattsson, A. Gromov, S. Dittmer, E. Eriksson, O. A. Nerushev, and E. E. B. Campbell, Dielectrophoresis-induced separation of metallic and semiconducting single-wall carbon nanotubes in a continuous flow microfluidic system, *Journal of Nanoscience and Nanotechnology* **7**, 3431–3435 (2007).
- [30] H. Peng, N. T. Alvarez, C. Kittrell, R. H. Hauge, and H. K. Schmidt, Dielectrophoresis field flow fractionation of single-walled carbon nanotubes, *Journal of the American Chemical Society* **128**, 8396–8397 (2007).
- [31] M. S. Dresselhaus, G. Dresselhaus, R. Saito, and A. Jorio, Raman spectroscopy of carbon nanotubes, *Physics Reports* **409**, 47–99 (2005).
- [32] <http://www.photon.t.u-tokyo.ac.jp/~maruyama/kataura/kataura.html>.
- [33] J.-C. Charlier, X. Blase, and S. Roche, Electronic and transport properties of nanotubes, *Reviews of Modern Physics* **79**, 677–732 (2007).
- [34] C. L. Kane and E. J. Mele, Size, shape, and low energy electronic structure of carbon nanotubes, *Physical Review Letters* **78**, 1932–1935 (1997).
- [35] J. W. Mintmire, B. I. Dunlap, and C. T. White, Are fullerene tubulus metallic?, *Physical Review Letters* **68**, 631–634 (1992).
- [36] N. Hamada, S. Sawada, and A. Oshiyama, New one-dimensional conductors: Graphitic microtubules, *Physical Review Letters* **68**, 1579–1581 (1992).
- [37] N. Wang, Z. K. Tang, G. D. Li, and J. S. Chen, Materials science: Single-walled 4 Å carbon nanotube arrays, *Nature* **408**, 50–51 (2000).
- [38] J. W. Mintmire and C. T. White, Universal density of states for carbon nanotubes, *Physical Review Letters* **81**, 2506–2509 (1998).

- [39] M. J. O'Connell, S. M. Bachilo, C. B. Huffman, V. C. Moore, M. S. Strano, E. H. Haroz, K. L. Rialon, P. J. Boul, W. H. Noon, C. Kittrell, J. Ma, R. H. Hauge, R. B. Weisman, and R. E. Smalley, Band gap fluorescence from individual single-walled carbon nanotubes, *Science* **297**, 593–596 (2002).
- [40] J. W. G. Wildöer, L. C. Venema, A. G. Rinzler, R. E. Smalley, and C. Dekker, Electronic structure of atomically resolved carbon nanotubes, *Nature* **391**, 59–62 (1998).
- [41] A. Jorio, A. G. S. Filho, G. Dresselhaus, M. S. Dresselhaus, R. Saito, J. H. Hafner, C. M. Lieber, F. M. Matinaga, M. S. S. Dantas, and M. A. Pimenta, Joint density of electronic states for one isolated single-wall carbon nanotube studied by resonant Raman scattering, *Physical Review B* **63**, 245416 (2001).
- [42] L. X. Benedict, S. G. Louie, and M. L. Cohen, Static polarizabilities of single-wall carbon nanotubes, *Physical Review B* **52**, 8541–8549 (1995).
- [43] B. Kozinsky and N. Marzari, Static dielectric properties of carbon nanotubes from first principles, *Physical Review Letters* **96**, 166801 (2006).
- [44] A. Jorio, R. Saito, T. Hertel, R. B. Weisman, G. Dresselhaus, and M. S. Dresselhaus, Carbon nanotube photophysics, *MRS Bulletin*, 276–280 (2004).
- [45] H. Ajiki and T. Ando, Aharonov-Bohm effect in carbon nanotubes, *Physica B* **201**, 349–352 (1994).
- [46] C. Fantini, A. Jorio, A. P. Santos, V. S. T. Peressinotto, and M. A. Pimenta, Characterization of DNA-wrapped carbon nanotubes by resonance Raman and optical absorption spectroscopies, *Chemical Physics Letter* **439**, 138–142 (2007).
- [47] J. Lefebvre, J. M. Fraser, P. Finnie, and Y. Homma, Photoluminescence from an individual single-walled carbon nanotube, *Physical Review B* **69**, 075403 (2004).
- [48] S. Lebedkin, K. Arnold, F. Hennrich, R. Krupke, B. Renker, and M. M. Kappes, FTIR-luminescence mapping of dispersed single-walled carbon nanotubes, *New Journal of Physics* **5**, 140 (2003).
- [49] S. M. Bachilo, M. S. Strano, C. Kittrell, R. H. Hauge, R. E. Smalley, and R. B. Weisman, Structure-assigned optical spectra of single-walled carbon nanotubes, *Science* **298**, 2361–2366 (2002).
- [50] F. Wang, G. Dukovic, L. E. Brus, and T. F. Heinz, The optical resonances in carbon nanotubes arise from excitons, *Science* **308**, 838–841 (2005).

- [51] F. Wang, D. J. Cho, B. Kessler, J. Deslippe, P. J. Schuck, S. G. Louie, A. Zettl, T. F. Heinz, and Y. R. Shen, Observation of excitons in one-dimensional metallic single-walled carbon nanotubes, *Physical Review Letters* **99**, 227401 (2007).
- [52] J. Deslippe, C. D. Spataru, D. Prendergast, and S. G. Louie, Bound excitons in metallic single-walled carbon nanotubes, *Nano Letters* **7**, 1626–1630 (2007).
- [53] C. V. Raman and K. S. Krishnan, A new type of secondary radiation, *Nature* **121**, 501–502 (1928).
- [54] M. Oron-Carl, F. Hennrich, M. M. Kappes, H. v. Löhneysen, and R. Krupke, On the electron-phonon coupling of individual single-walled carbon nanotubes, *Nano Letters* **5**, 1761–1767 (2005).
- [55] J. C. Meyer, M. Paillet, T. Michel, A. Moréac, A. Neumann, G. S. Duesberg, S. Roth, and J.-L. Sauvajol, Raman modes of index-identified freestanding single-walled carbon nanotubes, *Physical Review Letters* **95**, 217401 (2005).
- [56] A. Jorio, R. Saito, J. H. Hafner, C. M. Lieber, M. Hunter, T. McClure, G. Dresselhaus, and M. S. Dresselhaus, Structural (n,m) determination of isolated single-wall carbon nanotubes by resonant Raman scattering, *Physical Review Letters* **86**, 1118–1121 (2001).
- [57] S. D. M. Brown, A. Jorio, P. Corio, M. S. Dresselhaus, G. Dresselhaus, R. Saito, and K. Kneipp, Origin of the Breit-Wigner-Fano lineshape of the tangential G-band feature of metallic carbon nanotubes, *Physical Review B* **63**, 155414 (2001).
- [58] M. A. Pimenta and A. Marucci, Raman modes of metallic carbon nanotubes, *Physical Review B Rapid* **58**, R16016 (1998).
- [59] D. S. Bethune, C. H. Kiang, M. S. DeVries, G. Gorman, R. Savo, and R. Beyers, Cobalt-catalysed growth of carbon nanotubes with single-atomic-layer walls, *Nature* **363**, 605–607 (1993).
- [60] A. Thess, R. Lee, P. Nikolaev, H. Dai, P. Petit, J. Robert, C. Xu, Y. H. Lee, S. G. Kim, A. G. Rinzler, D. T. Colbert, G. E. Scuseria, D. Tománek, J. E. Fischer, and R. E. Smalley, Crystalline ropes of metallic carbon nanotubes, *Science* **273**, 483–487 (1996).
- [61] J. Kong, A. M. Cassell, and H. Dai, Chemical vapor deposition of methane for single-walled carbon nanotubes, *Chemical Physics Letters* **292**, 567–574 (1998).

- [62] K. Hata, D. N. Futaba, K. Mizuno, T. Namai, M. Yumura, and S. Iijima, Water-assisted highly efficient synthesis of impurity-free single-walled carbon nanotubes, *Science* **306**, 1362–1364 (2004).
- [63] T. Guo, P. Nikolaev, A. Thess, D. T. Colbert, and R. E. Smalley, Catalytic growth of single-walled nanotubes by laser vaporization, *Chemical Physics Letters* **243**, 49–54 (1995).
- [64] S. Lebedkin, P. Schweiss, B. Renker, S. Malik, F. Hennrich, M. Neumaier, C. Stoermer, and M. M. Kappes, Single-wall carbon nanotubes with diameters approaching 6 nm obtained by laser vaporization, *Carbon* **40**, 417–423 (2002).
- [65] F. Hennrich, R. Krupke, K. Arnold, J. A. R. Stütz, S. Lebedkin, T. Koch, T. Schimmel, and M. M. Kappes, The mechanism of cavitation-induced scission of single-walled carbon nanotubes, *Journal of Physical Chemistry B* **111**, 1932–1937 (2007).
- [66] S. Mukhopadhyay and U. Maitra, Chemistry and biology of bile acids, *Current Science* **87**, 1666–1683 (2004).
- [67] A. Quintilla, *Investigation of nanoscale structure formation and function using molecular dynamics simulations*, PhD thesis, Fakultät Physik der Technischen Universität Dortmund, 2007.
- [68] M. S. Arnold, A. A. Green, J. F. Hulvat, S. I. Stupp, and M. C. Hersham, Sorting carbon nanotubes by electronic structure using density differentiation, *Nature Nanotechnology* **1**, 60–65 (2006).
- [69] T. B. Jones, *Electromechanics of Particles*, Cambridge University Press, New York, 1995.
- [70] T. B. Jones, Basic theory of dielectrophoresis and electrorotation, *IEEE Engineering in Medicine and Biology Magazine* , 33–42 (2003).
- [71] H. Morgan and N. G. Green, *AC electrokinetics: colloids and particles*, Research Studies Press Ltd., Baldock, Hertfordshire, England, 2003.
- [72] C. Rosales and K. M. Lim, Numerical comparison between Maxwell stress method and equivalent multipole approach for calculation of the dielectrophoretic force in single-cell traps, *Electrophoresis* **26**, 2057–2965 (2005).
- [73] S. J. Tans, A. R. M. Verschueren, and C. Dekker, Room-temperature transistor based on a single carbon nanotube, *Nature* **393**, 49–52 (1998).
- [74] A. Javey, J. Guo, Q. Wang, M. Lundstrom, and H. Dai, Ballistic carbon nanotube field-effect transistors, *Nature* **424**, 654–657 (2003).

- [75] P. L. McEuen, M. S. Fuhrer, and H. Park, Single-walled carbon nanotube electronics, *IEEE Transactions on nanotechnology* **1**, 78–85 (2002).
- [76] F. Vermolen, Introduction into Finite Elements, <http://ta.twi.tudelft.nl/users/vermolen/wi3098.pdf>, 2005.
- [77] E. Süli, Finite element methods for partial differential equations, <http://web.comlab.ox.ac.uk/oucl/work/andre.suli/fem.ps>, 2007.
- [78] <http://www.pdesolutions.com>.
- [79] S. K. Doss, R. J. Gelinas, R. G. Nelson, and J. P. Ziagos, Adaptive forward-inverse modeling of reservoir fluids away from wellbores, Report UCRL-ID-126377, Lawrence Livermore National Laboratory, February 1999.
- [80] A. Castellanos, A. Ramos, A. González, N. G. Green, and H. Morgan, Electrohydrodynamics and dielectrophoresis in microsystems: Scaling laws, *Journal of Physics D: Applied Physics* **36**, 2584–2597 (2003).
- [81] L. D. Landau and E. M. Lifshitz, *Electrodynamics of Continuous Media*, Pergamon, Oxford, 1960.
- [82] J. R. Macdonald, Note on the parameterization of the constant-phase admittance element, *Solid State Ionics* **13**, 147–149 (1984).
- [83] K. Biswas, S. Sen, and P. K. Dutta, Realization of a constant phase element and its performance study in a differentiator circuit, *IEEE Transactions on Circuits and Systems II: Express Briefs* **53**, 802–806 (2006).
- [84] S. Blatt, F. Hennrich, H. v. Löhneysen, M. M. Kappes, and R. Krupke, Influence of structural and dielectric anisotropy on the dielectrophoresis of single-walled carbon nanotubes, *Nano Letters* **7**, 1960–1966 (2007).
- [85] M. F. Islam, D. E. Milkie, C. L. Kane, A. G. Yodh, and J. M. Kikkawa, Direct measurement of the polarized optical absorption cross section of single-walled carbon nanotubes, *Physical Review Letters* **93**, 037404 (2004).
- [86] P. G. de Gennes and J. Prost, *The physics of liquid crystals*, Clarendon Press, Oxford, 1974.
- [87] P. M. Chaikin and T. C. Lubensky, *Principles of condensed matter physics*, Cambridge University Press, Cambridge, UK, 1995.
- [88] H. H. Gommans, J. W. Alldredge, H. Tashiro, J. Park, J. Magnuson, and A. G. Rinzler, Fibers of aligned single-walled carbon nanotubes: Polarized Raman spectroscopy, *Journal of Applied Physics* **88**, 2509–2514 (2000).

- [89] H. Morgan and N. G. Green, Dielectrophoretic manipulation of rod-shaped viral particles, *Journal of Electrostatics* **42**, 279–293 (1997).
- [90] M. P. Hughes, Dielectrophoretic behavior of latex nanospheres: Low-frequency dispersion, *Journal of Colloid and Interface Science* **250**, 291–294 (2002).
- [91] C. W. Marquardt, S. Blatt, F. Henrich, H. v. Löhneysen, and R. Krupke, Probing dielectrophoretic force fields with metallic carbon nanotubes, *Applied Physics Letters* **89**, 183117 (2006).
- [92] N. G. Green, A. Ramos, and H. Morgan, Numerical solution of the dielectrophoretic and travelling wave forces for interdigitated electrode arrays using the finite element method, *Journal of Electrostatics* **56**, 235–254 (2002).
- [93] Y. Xue and M. A. Ratner, Electron transport in semiconducting carbon nanotubes with hetero-metallic contacts, *Nanotechnology* **16**, 5–9 (2005).
- [94] M. P. Anantram, S. Datta, and Y. Xue, Coupling of carbon nanotubes to metallic contacts, *Physical Review B* **61**, 14219–14224 (2000).
- [95] J. H. Walther, T. Werder, R. L. Jaffe, and P. Koumoutsakos, Hydrodynamic properties of carbon nanotubes, *Physical Review E* **69**, 062201 (2004).
- [96] H. Qian, T. Gokus, N. Anderson, L. Novotny, A. J. Meixner, and A. Hartschuh, Near-field imaging and spectroscopy of electronic states in single-walled carbon nanotubes, *physica status solidi (b)* **243**, 3146–3150 (2006).
- [97] L. C. Venema, J. W. Janssen, M. R. Buitelaar, J. W. G. Wildöer, S. G. Lemay, L. P. Kouwenhoven, and C. Dekker, Spatially resolved scanning tunneling spectroscopy on single-walled carbon nanotubes, *Physical Review B* **62**, 5238–5244 (2000).
- [98] H. Jiang, A. G. Nasibulin, D. P. Brown, and E. I. Kauppinen, Unambiguous atomic structural determination of single-walled carbon nanotubes by electron diffraction, *Carbon* **45**, 662–667 (2007).
- [99] A. Vijayaraghavan, S. Blatt, S. Dehm, and R. Krupke, Imaging electronic structure of carbon nanotubes by voltage-contrast scanning electron microscopy, submitted.
- [100] H. Seiler, Secondary electron emission in the scanning electron microscope, *Journal of Applied Physics* **54**, R1–R18 (1983).
- [101] O. C. Wells, *Scanning electron microscopy*, McGraw-Hill, New York, 1974.

- [102] M. Buzzo, M. Ciappa, J. Millan, P. Godignon, and W. Fichtner, Two-dimensional dopant imaging of silicon carbide devices by secondary electron potential contrast, *Microelectronic Engineering* **84**, 413–418 (2007).
- [103] A. Konrad and M. Graovac, The Finite Element modeling of conductors and floating potentials, *IEEE Transactions on Magnetics* **32**, 4329–4331 (1996).
- [104] D. L. John, L. C. Castro, J. Clifford, and D. L. Pulfrey, Electrostatics of coaxial Schottky-barrier nanotube field-effect transistors, *IEEE Transactions on Nanotechnology* **2**, 175–180 (2003).
- [105] M. S. Brown, J. W. Shan, C. Lin, and F. M. Zimmermann, Electrical polarizability of carbon nanotubes in liquid suspension, *Applied Physics Letters* **90**, 203108 (2007).
- [106] M. L. Chabinyk, D. T. Chiu, J. C. McDonald, A. D. Stroock, J. F. Christian, A. M. Karger, and G. M. Whitesides, An integrated fluorescence detection system in poly(dimethylsiloxane) for microfluidic applications, *Analytical Chemistry* **73**, 4491–4498 (2001).
- [107] M. S. Strano, C. B. Huffman, V. C. Moore, M. J. O’Connell, E. H. Haroz, J. Hubbard, M. Miller, K. Rialon, C. Kittrell, S. Ramesh, R. H. Hauge, and R. E. Smalley, Reversible, band-gap-selective protonation of single-walled carbon nanotubes in solution, *Journal of Physical Chemistry B* **107**, 6979–6985 (2003).
- [108] A. Nish, J.-Y. Hwang, J. Doig, and R. J. Nicholas, Highly selective dispersion of single-walled carbon nanotubes using aromatic polymers, *Nature Nanotechnology* **2**, 640–646 (2007).
- [109] S. Lebedkin, F. Hennrich, O. Kiowski, and M. M. Kappes, Photophysics of carbon nanotubes in organic polymer-toluene dispersions: Emission and excitation satellites and relaxation pathways, *Physical Review B* **77**, 165429 (2008).
- [110] H. Morgan, A. G. Izquierdo, D. Bakewell, N. G. Green, and A. Ramos, The dielectrophoretic and travelling wave forces generated by interdigitated electrode arrays: analytical solution using Fourier series, *Journal of Physics D: Applied Physics* **34**, 1553–1561 (2001).
- [111] C.-F. Chou, J. O. Tegenfeldt, O. Bakajin, S. S. Chan, E. C. Cox, N. Darnton, T. Duke, and R. H. Austin, Electrodeless dielectrophoresis of single- and double-stranded DNA, *Biophysical Journal* **83**, 2170–2179 (2002).
- [112] C.-F. Chou and F. Zenhausern, Electrodeless dielectrophoresis for micro total analysis systems, *IEEE Engineering in Medicine and Biology Magazine* **79**, 677–732 (2003).

- [113] Zeta-Meter Inc., Zeta Potential: A complete course in 5 minutes, <http://www.zeta-meter.com/5min.pdf>.
- [114] A. V. Delgado, F. González-Caballero, R. J. Hunter, L. K. Koopal, and J. Lyklema, Measurement and interpretation of electrokinetic phenomena, *Pure and Applied Chemistry* **77**, 1753–1805 (2005).
- [115] <http://www.pieper-filter.de/>.
- [116] <http://www.htw-germany.com/>.
- [117] R. R. Henriquez, T. Ito, L. Sun, and R. M. Crooks, The resurgence of Coulter counting for analyzing nanoscale objects, *The Analyst* **129**, 478–482 (2004).
- [118] A. J. Storm, C. Storm, J. Chen, H. Zandbergen, J.-F. Joanny, and C. Dekker, Fast DNA translocation through a solid-state nanopore, *Nano Letters* **5**, 1193–1197 (2005).
- [119] S. P. Han and S.-M. Yang, Orientation distribution and electrophoretic motions of rod-like particles in a capillary, *Journal of Colloid and Interface Science* **177**, 132–142 (1996).
- [120] Danmarks Tekniske Universitet, Department of Micro- and Nanotechnology, <http://www2.mic.dtu.dk/research/MIFTS/research/EKpumps.htm>.
- [121] J. F. Miller, K. Schätzel, and B. Vincent, The determination of very small electrophoretic mobilities in polar and nonpolar colloidal dispersions using Phase Analysis Light Scattering, *Journal of Colloid and Interface Science* **143**, 532–554 (1991).
- [122] S. K. Hait, P. R. Majhi, R. Blume, and S. P. Moulik, A critical assessment of micellization of sodium dodecyl benzene sulfonate (SDBS) and its interaction with poly(vinyl pyrrolidone) and hydrophobically modified polymers, JR400 and LM 200, *Journal of Physical Chemistry B* **107**, 3650–3658 (2003).
- [123] <http://www.sigmaaldrich.com/>.

# List of publications

Parts of this thesis have been previously published or were presented as conference contributions in poster sessions. In particular the work described in Sections 4.1 and 4.2 have been published in the Articles # 3 and 4, while Article # 5 contains the results of Chapter 3 and Section 4.3. Part of the work described in Section 4.4 has been submitted for publication in Article # 6.

## Articles:

1. S. Blatt, *Konstruktion und Inbetriebnahme eines Feldkäfigs für eine TPC*, Diplomarbeit, Fakultät für Mathematik, Informatik und Physik der RWTH Aachen, 2004.
2. S. Blatt, M. Giffels, G. Kaussen, M. Killenberg, S Lotze, J. Mnich, A. Münich, S. Roth, F. Sefkow, M. Tonutti, A. Vogel, M. Weber, and P. Wiennemann, Charge transfer of GEM structures in high magnetic fields, *Nuclear Physics B-Proceedings Supplements* **150**, 155-158 (2006).
3. C. W. Marquardt, S. Blatt, F. Hennrich, H. v. Löhneysen, and R. Krupke, Probing dielectrophoretic force fields with metallic carbon nanotubes, *Applied Physics Letters* **89**, 183117 (2006).
4. A. Vijayaraghavan, S. Blatt, D. Weissenberger, M. Oron-Carl, F. Hennrich, D. Gerthsen, H. Hahn, and R. Krupke, Ultra-large-scale directed assembly of single-walled carbon nanotube devices, *Nano Letters* **7**, 1556-1560 (2007).
5. S. Blatt, F. Hennrich, H. v. Löhneysen, M. M. Kappes, and R. Krupke, Influence of structural and dielectric anisotropy on the dielectrophoresis of single-walled carbon nanotubes, *Nano Letters* **7**, 1960-1966 (2007).
6. A. Vijayaraghavan, S. Blatt, S. Dehm and R. Krupke, Imaging electronic structure of carbon nanotubes by voltage-contrast scanning electron microscopy, submitted.
7. C. W. Marquardt, S. Dehm, A. Vijayaraghavan, S. Blatt, F. Hennrich, and R. Krupke, Reversible local metal-insulator transitions in metallic single-walled carbon nanotubes, *Nano Letters* (2008), in press.

**Conference contributions:**

- S. Blatt, F. Hennrich, H. v. Löhneysen, and R. Krupke, Thin films of metallic carbon nanotubes and their optical spectra, DPG Spring Meeting of the Division Condensed Matter, Dresden, March 2006.
- S. Blatt, C. W. Marquardt, F. Hennrich, H. v. Löhneysen, and R. Krupke, Probing dielectrophoretic force fields with metallic carbon nanotubes, International Winterschool on Electronic Properties of Novel Materials (IWEPNM), Kirchberg, Austria, March 2007.
- S. Blatt, C. W. Marquardt, A. Vijayaraghavan, F. Hennrich, and R. Krupke, Different orientation of metallic and semiconducting carbon nanotubes in thin films, International Winterschool on Electronic Properties of Novel Materials (IWEPNM), Kirchberg, Austria, March 2007.
- S. Blatt, C. W. Marquardt, I. Klugius, A. Vijayaraghavan, F. Hennrich, and R. Krupke, Upscaling dielectrophoretic nanotube separation and probing dielectrophoretic force fields, MRS Spring Meeting, San Francisco, USA, April 2007.
- S. Blatt, F. Hennrich, H. v. Löhneysen, M. M. Kappes, A. Vijayaraghavan, and R. Krupke, Influence of structural and dielectric anisotropy on the dielectrophoresis of single-walled carbon nanotubes, 8th International Conference on the Science and Application of Nanotubes (NT07), Ouro Preto, Brazil, June 2007.
- A. Vijayaraghavan, S. Blatt, D. Weissenberger, M. Oron-Carl, F. Hennrich, D. Gerthsen, H. Hahn, and R. Krupke, Ultra-large scale directed assembly of single-walled carbon nanotube devices, International Winterschool on Electronic Properties of Novel Materials (IWEPNM), Kirchberg, Austria, March 2007; MRS Spring Meeting, San Francisco, USA, April 2007; Web-seminar der Intel Corporation, 24.Mai 2007; 8th International Conference on the Science and Application of Nanotubes (NT07), Ouro Preto, Brazil, June 2007.
- S. Blatt, A. Vijayaraghavan and R. Krupke, Electrostatic modeling of carbon nanotubes in asymmetric electric fields, International Winterschool on Electronic Properties of Novel Materials (IWEPNM), Kirchberg, Austria, March 2008.
- A. Vijayaraghavan, S. Blatt and R. Krupke, Visualizing electronic structure of carbon nanotubes by voltage contrast scanning electron microscopy, International Winterschool on Electronic Properties of Novel Materials (IWEPNM), Kirchberg, Austria, March 2008.